Università degli Studi di Napoli Federico II

Dottorato di Ricerca in Fisica Fondamentale ed Applicata
XVIII ciclo

Elvira Rossi

Study of the angular resolution of the ARGO-YBJ experiment: The shadow of the Moon

Il Coordinatore:
Prof. Arturo Tagliacozzo

Novembre 2005

Contents

Contents i

Introduction 1

1 Introduction to $\gamma-$ray Astronomy 5
- 1.1 Brief history . . . 7
- 1.2 Observation Summary . . . 11
- 1.3 Detection techniques . . . 15
  - 1.3.1 Satellites . . . 16
  - 1.3.2 Ground-based detection. . . . 16
  - 1.3.3 General characteristics of ground-based detectors. . . . 18
  - 1.3.4 Atmospheric Cherenkov Telescopes . . . 21
  - 1.3.5 Extensive Air Shower Arrays . . . 23
- 1.4 New generation EAS arrays . . . 23
- 1.5 Moon shadow concept . . . 26
  - 1.5.1 Earth magnetic-field and calculations of the deflection 28

2 The ARGO-YBJ experiment 31
- 2.1 The ARGO-YBJ experiment . . . 32
- 2.2 RPC performance . . . 37
- 2.3 Trigger logic . . . 37
- 2.4 Observational Techniques . . . 41
- 2.5 Analog read-out . . . 42

3 Study of the angular resolution of the ARGO-YBJ detector 45
- 3.1 Reconstruction procedure of the shower direction . . . 46
- 3.2 The effect of a lead sheet on improving the angular resolution 51
- 3.3 Identification of showers with core outside the array . . . 54
- 3.4 The expected angular resolution of ARGO-YBJ . . . 56
- 3.5 The angular resolution of the ARGO-42 carpet . . . 57
  - 3.5.1 Analysis with the zenith angle distribution . . . 62
- 3.6 Conclusions . . . 64

4 The shadow of the Moon **65**
4.1 Moon-shadow simulation 65
4.1.1 An estimation of the expected "signal" 65
4.1.2 Angular resolution estimation 67
4.1.3 Cosmic ray tracking 68
4.1.4 Understanding the "source" 70
4.2 Signal analysis: method and procedure 73
4.2.1 Background determination 74
4.3 Data analysis 74
4.3.1 Smoothed map 75
4.4 Sun shadow 88
4.5 Conclusions 88

Conclusions **91**

Bibliography **93**

Aknowledgments **97**

Introduction

Ever since cosmic rays were discovered at the turn of XXI century the quest for their origin was on. Soon after the discovery it was realized that cosmic rays are of extra-solar origin. Being charged particles, cosmic rays are scattered and isotropised by the galactic magnetic field and hence lose their original directions. If a neutral radiation like photons (gamma rays) is associated with the presence of energetic particles in a source, they travel in straight lines and their sources can be identified.

Schklovsky [1] pointed out in the early 50's that the high degree of optical polarization from the Crab Nebula could be accounted for by synchrotron process requiring the presence of very high energy electrons ($> 10^{12}$ eV) gyrating round the magnetic fields ($\sim 10^{-4}$ gauss) in the filaments of the nebula.

In 1960 Cocconi [2] suggested that since electrons of such high energy cannot arise from nuclear decay processes, a mechanism of acceleration of particles to high energies must be operative in the Nebula. If such a mechanism was indeed present, there was no reason why protons could not be accelerated to high energies too. Such protons in their nuclear collisions with the filamentary matter could produce charged and neutral pions. Decay of such high energy neutral pions results in the production of high energy (hundreds of GeV) gamma rays.

Thus the detection of high energy gamma rays leads to discovery of cosmic ray sources.

The success of gamma-ray astronomy, in particular the recent exciting discoveries of many new galactic and extragalactic TeV γ-ray emitters by the ground-based Cherenkov arrays, elevated the status of the field from an "astronomy with several sources" to the level of truly observational discipline [3].

It is clear that TeV sources are a powerful tool for exploring the relativistic universe. Despite the rich catalog of sources there is still not unambiguous evidence for the source of the hadronic cosmic radiation; it is possible to explain all the observed TeV gamma rays as coming from electron progenitors. Hence despite the dramatic advances that the new catalogs of TeV sources represent, the origin of the cosmic radiation remains a mystery.

Since the primary cosmic ray spectrum extend up to 10^{20} eV there is a

clear evidence the cosmic hadronic accelerators are at work somewhere in the Universe. Only the observation of high energy gamma-ray (or neutrinos) emission can finally identify the cosmic ray sources.

The main characteristic of the TeV discovered sources are that they are inherently multiwavelength with an high degree of variability. As a consequence, the continuously monitoring of the sources at any wavelength is required to investigate the physical processes at work in the celestial objects.

To perform an "all sky" monitoring looking at transient events, it's indispensable the use of a $\gamma-$ray detector with high sensitivity at TeV energies and with a wide field of view and high duty cycle.

Only an unconventional full-coverage air shower array located at very high altitude may cope with these requirements. The ARGO-YBJ (Astroparticle Radiation with Ground-based Observatory at YangBaJing) experiment is a full-coverage air shower detector devoted to the study of cosmic rays, mainly γ radiation with an energy threshold of a few hundreds GeV.

Since December 2004 to July 2005 the ARGO-42 detector, a carpet of about 1900 m^2 of RPCs (42 Clusters, $\sim 47 \times 41$ m^2, corresponding to about 1/3 of the whole central detector) has been put in stable data taking, yet without any converter sheet. The analysis carried out in this thesis concerns the data recorded in this period. Presently (Nov. 2005) 102 clusters of the central detector carpet have been installed and 74 of them are in data taking for debugging.

In a search for cosmic point sources with ground based experiments the main problem is the background due to charged cosmic rays. To observe point sources, neutral particles emitted from them must be detected above the nearly isotropic background of cosmic rays.

A point source is inferred from an excess of showers arriving from a particular direction of the celestial sphere. Because of the finite instrument resolution, showers from a point source appear to arrive from a finite region of the sky and are therefore accompanied by a background of nearly isotropic cosmic rays. An accurate determination of both signal and background from a particular direction therefore requires a good understanding of the angular resolution (measurement of the arrival direction) of the detector.

As first suggested by Clark in 1957 [4], the cosmic ray anti-source of the Moon or Sun may be treated as a fiducial object. Since the Moon and Sun each have an angular radius of approximately 0.26°, they must cast a shadow in the high-energy cosmic ray flux (this is the so-called *"shadow of the Moon"*). The shadowing of cosmic rays from the direction of the Moon or Sun is therefore useful in measuring the angular resolution of an array directly, without the need to invoke MonteCarlo simulations. Observing the expected depth of shadowing also verifies the array pointing accuracy and stability.

In principle, the size of the deficit gives us information about the angular resolution while the position of the dip provides information about the

pointing error.

This thesis is devoted to the study of the angular resolution of the ARGO-YBJ detector both with MonteCarlo simulations and data analysis. For the first time a systematical analysis of the ARGO-YBJ data has been carried out and is presented.

The work of thesis is organized as follow:

- The Chapter 1 is dedicated to a brief introduction to $\gamma-$Astronomy. The status of the observations is summarized with a comparison of between the main experimental techniques. Finally the concept of the shadow of the Moon is presented.

- In Chapter 2 the ARGO-YBJ experiment and its detector are described. The scientific motivations of the project will be pointed out.

- In Chapter 3, the procedure to reconstruct the primary direction of showers sampled both by the full ARGO-YBJ carpet and the smaller detector ARGO-42 is investigated. A comparison between MonteCarlo simulations and data collected by ARGO-42 is presented.

- In Chapter 4 the analysis of the shadow of the Moon observed with ARGO-42 is presented. MonteCarlo simulations and data are compared.

Chapter 1

Introduction to $\gamma-$ray Astronomy

Understanding cosmic ray origin and transport through the interstellar medium is a fundamental problem which has a major impact on models of the structure and nature of the universe. During the last years $\gamma-$ray Astronomy and ν-Astronomy have emerged as powerful tools to study cosmic ray features. In fact these neutral particles are not deviated by galactic or extragalactic magnetic fields so their directions bring the information of the production sites. Thus the search for γ or ν is primarily addressed to the search of cosmic ray sources and to the investigation of the phenomena in the acceleration sites. Due to the extremely small cross sections for weak interactions ($\lambda \sim \frac{10^{12}}{E}\ g/cm^2$), neutrinos are able to leave compact sources, providing the observer with information from inside or the surroundings of supernovae, active galaxies or other cosmic systems. The challenge is to find neutrino induced muons among those produced by the primary cosmic rays in the atmosphere. Nevertheless the search of high energy neutrinos point sources in the northern hemisphere using the data collected by AMANDA[5] from 2000 to 2005 reveals no statistically significant excess.

Even if the horizon of a high energy photon is not extended, due to $\gamma-\gamma$ interaction, as the neutrino one (see Fig. 1.1), TeV $\gamma-$rays from many sources have been definitively observed providing evidence of the existence of energetic accelerating mechanism.

The detection of high energy $\gamma-$rays is the final step to use the whole electromagnetic spectrum for investigating the most energetic processes and phenomena in the Universe. Photons come from a variety of astronomical sources which accelerate charged cosmic rays (SuperNovae (SN), neutron stars, quasars, Active Galactic Nuclei (AGN)). Therefore the detection of very high-energy (VHE) and ultrahigh-energy (UHE) $\gamma-$ray signals from celestial point sources give us a clue for understanding the acceleration of particles to ultrahigh-energies.

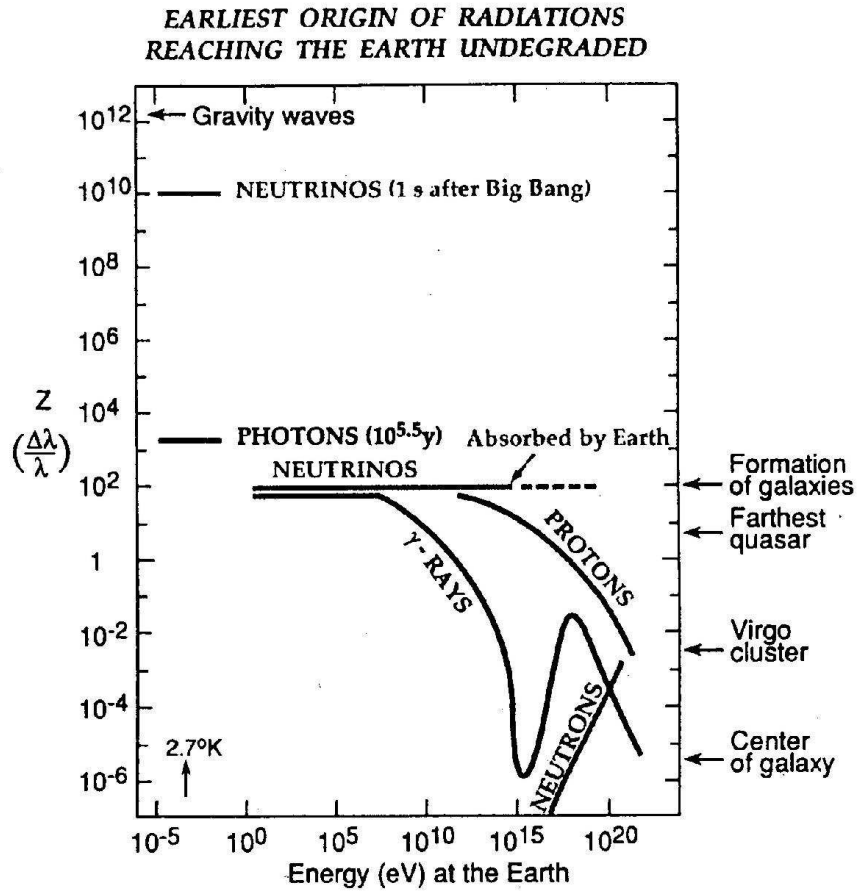

Figure 1.1: *The horizon measured in red-shift as a function of the energy on Earth of different kinds of cosmic radiations.*

So a first motivation for high energy γ−ray astronomy is the study of the phenomenology of these sources. Since non-thermal spectra are a common feature of the observed γ sources, detection of TeV sources can provide constraints on the models of acceleration and radiation processes at extreme conditions. The discovery of new types of sources is an intriguing perspective.

γ−ray astronomy could also give new hints to cosmology (through the measurement of the infrared background or studying primordial black holes) and particle physics beyond the Standard Model (evidence of supersymmetric particles).

These grounds led to a large diffusion of the γ−ray astronomy in the last decades. The number of present and planned experiments demonstrates the continuous growing interest of the scientific community in this field.

Satellite and Cerenkov detectors revealed a lot of $\gamma-$ray sources. However, to perform an "all sky" monitoring looking at transient events, it's indispensable the use of a $\gamma-$ray detector with high sensitivity at TeV energies and with a wide field of view (FOV) and high duty cycle. A high altitude full-coverage detector, like ARGO-YBJ, may cope with these requirements.

The ARGO-YBJ detector [6], a full coverage array operating in Tibet at 4300 $ma.s.l$, has an energy threshold of about 300 GeV, $FOV \sim 2\ sr$ and a duty cycle limited only by the operation efficiency.

Since the sensitivity (S) of ground based detectors depends on the angular resolution (σ_θ), $S \propto \frac{1}{\sigma_\theta}$, it's crucial to optimize σ_θ and to determine the pointing systematic effects. These studies can be carried out analyzing the shadowing of cosmic rays from the direction of the Moon. This method turns out to be extremely powerful to assess the detector performance. As a consequence, in the last years the Moon shadow observation at high energy ($> 50\ TeV$) has been a useful tool to have a direct measurement of the angular resolution and to study the systematic errors in pointing a source. The shadowing of cosmic rays by the Moon could also be used to measure the antiproton-proton ratio at TeV energies [7, 8, 9].

This chapter provides a short introduction to $\gamma-$ray astronomy. The status of the observations will be reviewed and the characteristics of the experimental techniques briefly discussed. In the last section the concept of the Moon shadow analysis will be presented.

1.1 Brief history

At the beginning of the XVII century Galileo Galilei first used a telescope to observe the sky in a narrow spectrum of visible frequencies. Some centuries later, in the 1931-32, Jansky discovered radio cosmic emission. That was the beginning of the astronomy extended over all the electromagnetic spectrum.

In the summer of 1962, an X-ray detector on the Aerobee rocket was flown. The goal of this flight was originally to detect X-ray fluorescence of the Moon due to the Sun's wind. It failed to detect such emission, however, the detector serendipitously discovered extra solar X-rays from a source named Scorpius X-1 (the first X-ray source seen in the constellation Scorpio). In addition, it detected a diffuse X-ray background (some of this has been resolved into sources and the rest is believed to be from unresolved active galaxies).

In the 1961 the satellite Explorer XI first revealed $\gamma-$rays but the first meaningful results were obtained in the 1972-73 when the satellite SAS-2 took data for 7 months collecting about 8000 photons in the energy range $30\ MeV \div 5\ GeV$. In the period between the 1975 and the 1982 the satellite COS-B identified 25 galactic sources of photons at GeV energies.

In the late $60s$ Cocconi suggested the idea of exploring the TeV energy

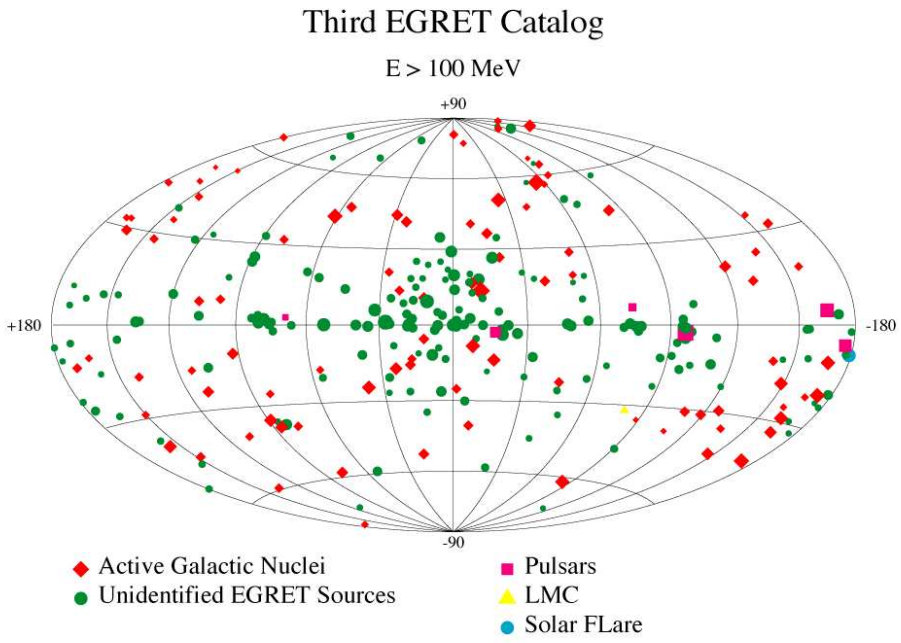

Figure 1.2: *Catalogue in galactic coordinates of the $\gamma-$ray point sources detected by EGRET above* 100 MeV *[10].*

range using ground based detectors to observe $\gamma-$induced air showers.

Indirect measurements at VHE and UHE were made from the 70s by means of Cerenkov telescopes. In the 1972, the Cerenkov telescope of the Crimean Astrophysical Observatory first revealed an excess of showers at TeV energies coming from the direction of the binary source Cygnus X-3. That signed the beginning of the VHE $\gamma-$ray astronomy.

In the early 80s the detection of UHE photons ($\sim 10^{15}\ eV$) from Cygnus X-3 has been claimed by Kiel and Haverah Park air shower arrays. However, a lot of dedicated ground based experiments (EAS-TOP, HEGRA, CASA-MIA) didn't detect any signal, and they provided only upper limits at a level of 1/100 of the previous detections. That seemed to mark the end of the high energy $\gamma-$ray astronomy.

The Compton Gamma Ray Observatory (CGRO) marked a turning point for $\gamma-$ray astronomy. The CGRO, launched into orbit in 1991, thanks to the detector EGRET detected 271 sources with $\gamma-$rays at energies between 100 MeV and 10 GeV. Fig. 1.2 shows a galactic map of the $\gamma-$ray point sources detected by EGRET as published in their third catalogue [10] based on $\sim$ 4 years of observation (April 1991 - October 1995).

The identified sources consist of 8 pulsars, 1 solar flare, 66 high-confidence

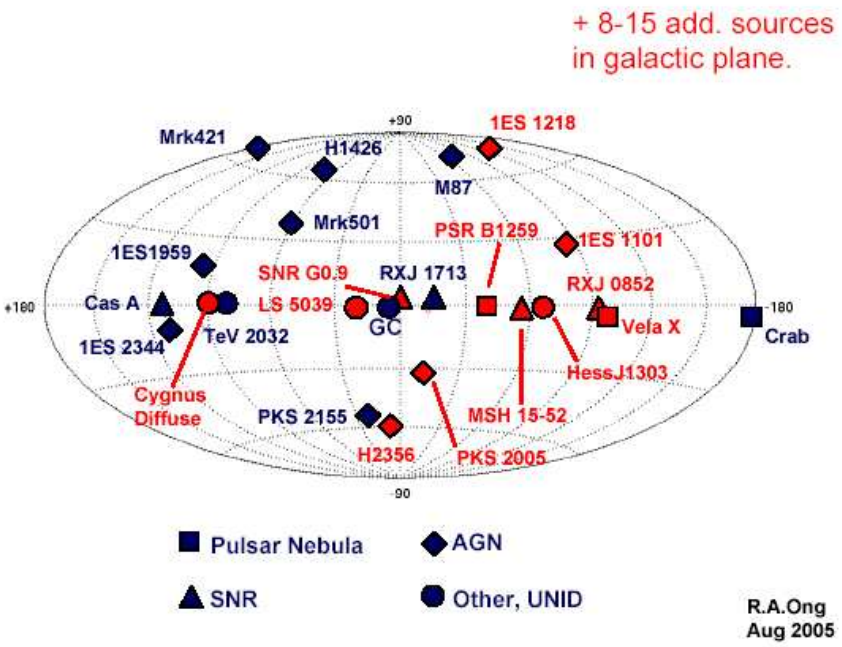

Figure 1.3: *Map of the VHE sky in the 2005 [11].*

blazars identifications, 27 possible blazars, 1 radio galaxy (Cen A) and the Large Magellanic Cloud (LMC). The remaining 170 sources, mostly located along the galactic plane, are not yet identified with known objects, since they have no observed counterparts at other wavelengths.

At the end of 80s a new generation of Cerenkov telescopes enabled to establish that the Crab Nebula is a stationary and continuous source of photons with an energy from 0.5 TeV to 10 TeV. Indeed in 1989 the Cerenkov telescope WHIPPLE observed an excess of photons with energies $\geq$ 500 GeV coming from the direction of the Crab Nebula. After WHIPPLE, others Cerenkov telescope confirmed the stationary flux from the Crab, which is now considered the "standard candle" for the northern hemisphere detectors. Observation of the Crab are used to demonstrate the perfect running of an experiment and to refine the data analysis methods. The Crab photon flux is considered a unit of measurement to evaluate the sensitivity of the apparatus. In the Fig. 1.4 is shown the Crab flux recently measured by the HEGRA experiment. The energy spectrum extends up to 80 TeV.

In 1999, the experiment Tibet As-γ provided the first observation of TeV photons with an air shower arrays.

In section 1.2 is reported the present status of the observations as summarized at the recent ICRC 2005 conference. Despite the large number of sources detected by EGRET, up to now 42 sources have been observed

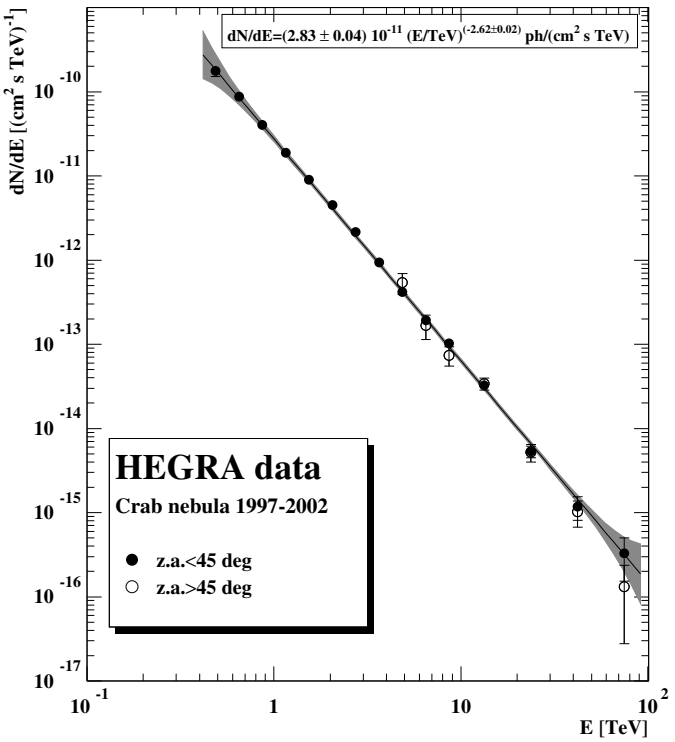

Figure 1.4: *Differential spectrum of the Crab Nebula as measured by the HEGRA system of imaging air Cerenkov telescopes [12].*

in the VHE range at energies above 200 GeV. Their locations in galactic coordinates are shown in Fig. 1.3.

Presently, there are 6 kind of experiments operating or under construction:

- Cerenkov telescope with one big mirror (MAGIC).
- Arrays of Cerenkov telescopes (H.E.S.S, VERITAS).
- Solar towers (STACEE, CELESTE, GRAAL, Solar Two Observatory).
- High density EAS arrays (Tibet As$-\gamma$).
- Full coverage EAS array (ARGO-YBJ, MILAGRO).

They will allow to extend the explored energy range ($E_{min} \sim 50\ GeV$ and $E_{max} \sim 50\ TeV$) with a sensitivity down to 10^{-2} Crab units (see section 1.3).

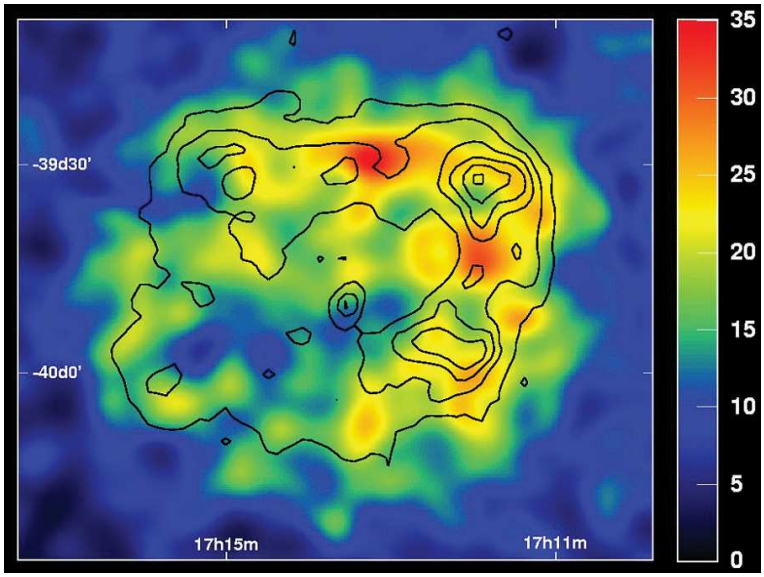

Figure 1.5: *The first astronomical image in VHE gamma rays - supernova remnant RXJ1713.7-3946. The remnant is about twice the diameter of the Moon. Superimposed for comparison are the contours of the X-ray emission observed with the ASCA satellite.*

1.2 Observation Summary

VHE gamma-ray astronomy is now a fast moving field and the observational picture is changing quickly as the new generation of telescopes comes on-line.

Since last two years the HESS array of 4 air Cherenkov gamma-ray telescopes deployed under the southern sky of Namibia delivered the highlights in the particle astrophysics corner. HESS provides unprecedented sensitivity to γ-rays above 100 GeV, below 1% of the flux from the Crab Nebula for 25 hours of observation. As a consequence, for the first time an instrument is capable of imaging astronomical sources in TeV gamma rays. Its images of young galactic SuperNova Remnants shows filament structures of high magnetic fields that are capable of accelerating protons to the energies, and with the energy balance, required to explain the galactic cosmic rays. In Fig. 1.5 the first TeV gamma-ray image of a Supernova shell (RXJ1713.7-3946) is shown. Although the smoking gun for cosmic ray acceleration is still missing, the evidence is tantalizingly close.

The HESS observatory has been particularly productive and it is expected that it will shortly be joined by CANGAROO-III, MAGIC and VERITAS.

In Table 1.2.1 the catalog of Galactic VHE sources is reported updated to the ICRC 2005 (August, 2005). The first column gives the catalog name

for the source, the second the conventional source name (where there it is a known object), the third is the source type, where known, the fourth the date of discovery and the group responsible for the discovery.

The Table 1.2.2 shows extra-galactic sources, about all of them are blazars. All of these detections are well-established. Taken together these sources form the basis for a new exploration of relativistic particles in the jets of Active Galactic Nuclei (AGN).

A feature of these new catalogs is that not only they does contain many new sources, but they also contain some significant omissions. Several sources, including TeV 0047-2518 (NGC 253), TeV 0834–4500 (Vela), TeV 1503-4157 (SN1006) and TeV 1710-2229 (PSR 1706-44), have not been verified by the more sensitive observations by HESS. All four sources were reported with good statistical significance by the CANGAROO group. It is apparent that there were unknown systematic errors in the data taking and/or the analyzes were not independently verified within the large CANGAROO collaboration. Since many of these CANGAROO pseudo-sources were reported to have steep spectra, one possible explanation for the data was unevenly matched ON and OFF fields and hence systematic biases in the data sets.

It should be noted that a few of the sources listed in the tables still do not have the statistical significance and independent verification that one would like. These include TeV 0219+4248 (3C66a), TeV 1121-6037 (Centaurus X-3), TeV 2203+4217 (BL Lac) and TeV 2323+5849 (Cassiopeia A).

At TeV energies the Milagro water-Cherenkov detector [24] and the Tibet air-shower array [25] have been used to perform large-scale surveys. While these instruments have the advantage of a very wide field of view ($\sim$ 1 sterad), the sensitivity obtained by these surveys is rather limited, reaching a flux limit comparable to the flux of the Crab Nebula, $\sim 3\times10^{-10}$ cm^{-2} s^{-1}, for E $>$ 200 GeV ($\sim 2 \times 10^{-11}$ cm^{-2} s^{-1} for E $>$ 1 TeV), in one year of observations. Both surveys covered $\sim$ 2 *sterad* of the northern sky and revealed no previously unknown significant $\gamma-$ray sources. However, some evidence for $\gamma-$ray emission was found by the Milagro Collaboration from a region in the Cygnus constellation and another region close to the Crab Nebula [26]. Recently the detection of diffuse emission from the Galactic Plane with Milagro has been reported [27].

The HEGRA instrument was the first array of imaging air Cherenkov telescopes to be used to survey a part of the Galactic Plane [28]. The range of Galactic longitudes (l) $-2^\circ < l < 85^\circ$ was observed; due to the location of HEGRA in the northern hemisphere and the resulting large zenith angles for observations of the centre of the Galactic Plane, the sensitivity was reduced for the central part of the Galaxy and the energy threshold of the observations ranged from 500 GeV to 7 TeV. No sources of VHE $\gamma-$rays were found in this survey, and upper limits between 15% of the Crab flux for Galactic longitudes $l > 30^\circ$ and more than 30% of the Crab flux in the

TeV Catalog Name	Source	Type	First Detection	Ref.
J0535+2200	Crab Nebula	PWN	Whipple(1989)	[13]
J1514-591	MSH15-52	PWN	HESS(2005)	[14]
J1747-281	G0.9+0.1	PWN	HESS(2005)	[15]
J0852-4622	Vela Junior	PWN	HESS(2005)	[16]
J1616-508	PSR1617-5055	PWN	HESS(2005)	[15]
J1825-137	G18.0-0.7	PWN	HESS(2005)	[15]
J1713-381	G 348.7+0.3	SNR	HESS(2005)	[15]
J1713-397	RXJ1713.7-3946	SNR	CANGAROO(1999)	[17]
J2323+5849	Cas A	SNR	HEGRA(1999)	[18]
J1813-178		SNR	HESS, MAGIC(2005)	[19]
J1834-087	G23.3-0.3/W41	SNR	HESS(2005)	[15]
J1640-465	G338.3-0.0	SNR	HESS(2005)	[15]
J1804-216	G8.7-0.1/W30	PWN/SNR	HESS(2005)	[15]
J1837-069	G25.5+0.0	SNR	HESS(2005)	[15]
J1632-478	IGR J16320-4751	XRB	HESS(2005)	[19]
J1634-472	IGR J16358-4726/G337.2+0.1	XRB/SNR	HESS(2005)	[19]
J1121-6037	Cen X-3	Binary	Durham(1998)	[20]
J1302-638	PSR1259-63/SS2883	BP	HESS(2005)	[21]
J1745-290	Gal. Cen.	SNR/BH	HESS(2005)	[**?**]
J1826-148	LS 5039	Microquasar	HESS(2005)	[14]
J2032+4131	CygOB2	OB assoc.	HEGRA(2002)	[22]
J1640-465	G338.-0.0	SNR/UID	HESS(2005)	[15]
J1303-631	Unidentified	UID	HESS(2005)	[23]
J1614-518	Unidentified	UID	HESS(2005)	[15]
J1616-508	Unidentified	UID	HESS(2005)	[15]
J1745-290	3EG J1744-3011	UID	HESS(2005)	[19]
J1708-410	Unidentified	UID	HESS(2005)	[19]
J1702-420	Unidentified	UID	HESS(2005)	[19]
J1745-303	3EG J1744-3011	UID	HESS(2005)	[19]

Table 1.2.1: *VHE Galactic Sources. PWN=Pulsar Wind Nebulae, SNR=SuperNova Remnant, XRB=X-Ray Binary, BP=Binary Pulsar, UID=Unidentified Source.*

Source	Class	Redshift	First Detection	Confirmation
M87	Radio Gal.	0.004	HEGRA(2003)	HESS
Mrk 421	BL Lac(HBL)	0.031	Whipple(1992)	Many
Mrk 501	BL Lac(HBL)	0.034	Whipple(1995)	Many
1ES2344+514	BL Lac(HBL)	0.044	Whipple(1997)	HEGRA
1ES1959+650	BL Lac(HBL)	0.048	Tel. Array(1999)	Many
2203+4217	BL Lac(HBL)	0.069	Crimea(2001)	
1ES2005-489	BL Lac HBL)	0.071	HESS(2005)	
PKS2155-304	BL Lac(HBL)	0.117	Mark VI(1996)	HESS
H1426+428	BL Lac(HBL)	0.129	Whipple(2002)	Many
H2356-309	BL Lac(HBL)	0.165	HESS(2005)	
1ES1218+304	BL Lac(HBL)	0.182	MAGIC(2005)	
1ES1101-232	BL Lac(HBL)	0.186	HESS(2005)	
3C66A	BL Lac(HBL)	0.444	Crimea(1998)	

Table 1.2.2: *TeV AGN Summary.*

inner part of the Milky Way were derived.

A survey of the inner part of the Galactic Plane in very high energy $\gamma-$rays has been performed with the HESS Cherenkov telescope system. The Galactic Plane between $\pm 30^\circ$ in longitude and $\pm 3^\circ$ in latitude relative to the Galactic Centre was observed in 500 pointings for a total of 230 hours, reaching an average flux sensitivity of 2% of the Crab Nebula at energies above 200 GeV. Fourteen previously unknown sources were detected at a significance level greater than 4σ after accounting for all trials involved in the search.

It is clear that TeV sources are ubiquitous and a powerful tool for exploring the relativistic universe. Despite this rich catalog of sources there is still not unambiguous evidence for the source of the hadronic cosmic radiation; it is possible to explain all the observed TeV gamma rays as coming from electron progenitors. Hence despite the dramatic advances that the new catalogs of TeV sources represent, the origin of the cosmic radiation remains a mystery.

A number of new improved experiments are on-going or planned for the next years. Their main goals are:

- to improve the flux sensitivity better than percent of the Crab flux (for the detection of fainter objects)
- to achieve a continuous monitoring of the whole sky ("all sky survey") with improved efficiency for transient emission.
- to bridge the energy range between 20 GeV and 200 GeV that has been only marginally observed.

High Energy (HE)	$30\ MeV \div 100\ GeV$
Very High Energy (VHE)	$100\ GeV \div 30\ TeV$
Ultra High Energy (UHE)	$30\ TeV \div 30\ PeV$
Extremely High Energy (EHE)	$> 30\ PeV$

Table 1.3.3: *Conventional subdivisions of the cosmic ray spectrum [29].*

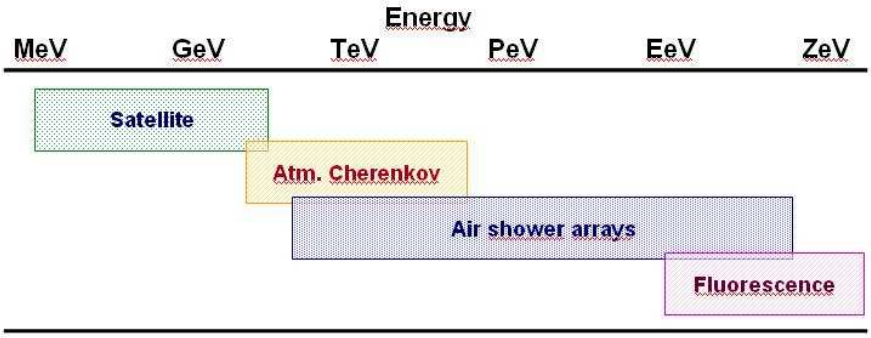

Figure 1.6: *Detection technique used to observe cosmic rays in different energy ranges [30].*

1.3 Detection techniques

The extremely large energy range implies a great variety of generation phenomena and require different detection techniques. For this reason the $\gamma-$spectrum is conventionally divided into subranges approximately corresponding to energy bands over which the different experimental techniques are used (see Table 1.3.3 and Fig. 1.6).

The detection techniques that can be used in HE/VHE $\gamma-$ray astronomy are determined by the properties of the γ radiation and by the background:

1. The Earth's atmosphere is opaque to $\gamma-$rays being about 28 radiation lengths thick at sea level. Therefore, $\gamma-$rays cannot be directly observed by ground-based detectors.

2. The γ-ray flux is very small ($\leq 10^{-3}$ respect to the background of CRs detected in a 1° angle around the direction of the source) and rapidly decreases when energy rises. All the known sources exhibit a typical differential spectrum in the form of a power-law:

$$\frac{dN}{dE} = E^{-\gamma} \tag{1.1}$$

with $\gamma \sim 2-3$. Small detectors over satellite permitted observation of tenths GeV $\gamma-$rays. To reveal the low flux at higher energies is indispensable to build up ground-based detectors where is possible to have big collecting areas. AGILE [31] and GLAST [32] are planned satellite experiments able to reach energies up to 200 GeV.

3. The isotropic CR flux forms a formidable background exceeding by many orders of magnitude even the strongest steady photon flux. It consists largely in protons and heavier nuclei.

Given the limitations imposed by this facts, a terrestrial observer can use different strategies to face the problem of the cosmic rays detection.

1.3.1 Satellites

Making use of detectors flown on satellites is the simplest way to avoid the problem of the atmosphere. Satellite detectors consist mainly of one or more converters layer in which HE photons produce a pair e^+e^-, a tracking detector in which the electron/positron is traced (used to reconstruct the direction of the incident photon with an angular resolution of $\leq 1^\circ$) and a total absorption calorimeter that allows for an energy estimate (resolution $\leq 20\%$). The problem of CR background is solved with a charged particle veto counter that efficiently rejects charged CRs. In the scheme shown in Fig. 1.7 the various elements can be recognized.

The strong limitation for this technique is the point (2): since the size of detectors is constrained by the weight that can be placed on satellites, their collection area is not large. Hence the rapid decreasing of the typical fluxes determines a maximum energy at which the collection area suffices for a statistical significant detection. In the case of EGRET this energy was ~ 10 GeV while the next generation satellite GLAST (shown in Fig. 1.7) should be sensitive up to 200 GeV.

1.3.2 Ground-based detection.

In the VHE range the low fluxes and the spectral slope of the typical sources require the use of very large detectors. Therefore, observations must be done from the Earth's surface. Due to the opacity of the atmosphere to VHE photons, only the secondary effects of the atmospheric absorption can be detected. Until now two experimental approaches have been used to detect γ radiation from the ground:

- Collection of the charged particles of the Extensive Air Showers (EAS) using detectors scattered over wide areas.
  When a photon enters the atmosphere, it interacts with atmospheric nuclei predominantly via pair production. The initial e^+e^- pair produces photons through bremsstrhalung, which in turn convert into

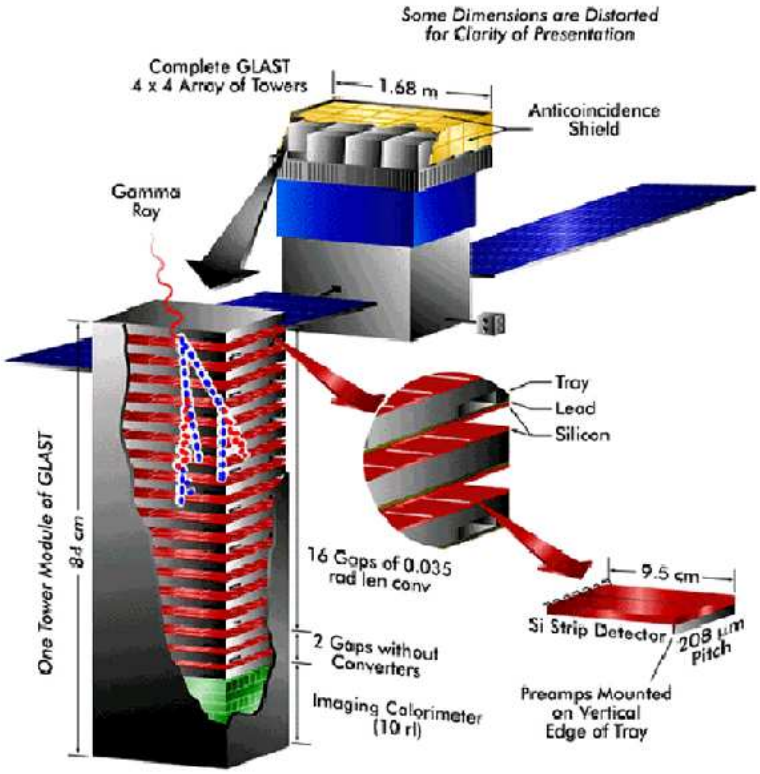

Figure 1.7: *Scheme of the GLAST detector. The silicon strip layers alternated with absorber layers serve as trackers to determine the $\gamma-$ray incident direction, the imaging CsI calorimeter is used to reconstruct the energy. The anti-coincidence shield (in yellow) allows for an efficient rejection of charged cosmic rays.*

more electron-positron pairs and so on. The result is a cascade of particles whose number grows nearly exponentially[1]. The energy of the primary photon is divided among the resulting particles. Therefore, when the mean energy of electrons and positrons goes below the critical energy in air ($\sim 81\ MeV$) ionization losses become predominant and the number of particles gradually decreases. Since the particles in the EAS are relativistic, they retain the original direction of the primary particle to a high degree. The result observed at ground level is a large disk of secondary particles, few meters thick and orthogonal to the direction of the primary photon. The charged CRs also produce EAS is similar to those induced by photons.

- Measurement of the Cherenkov light.

[1] More details on air showers can be found for example in [33].

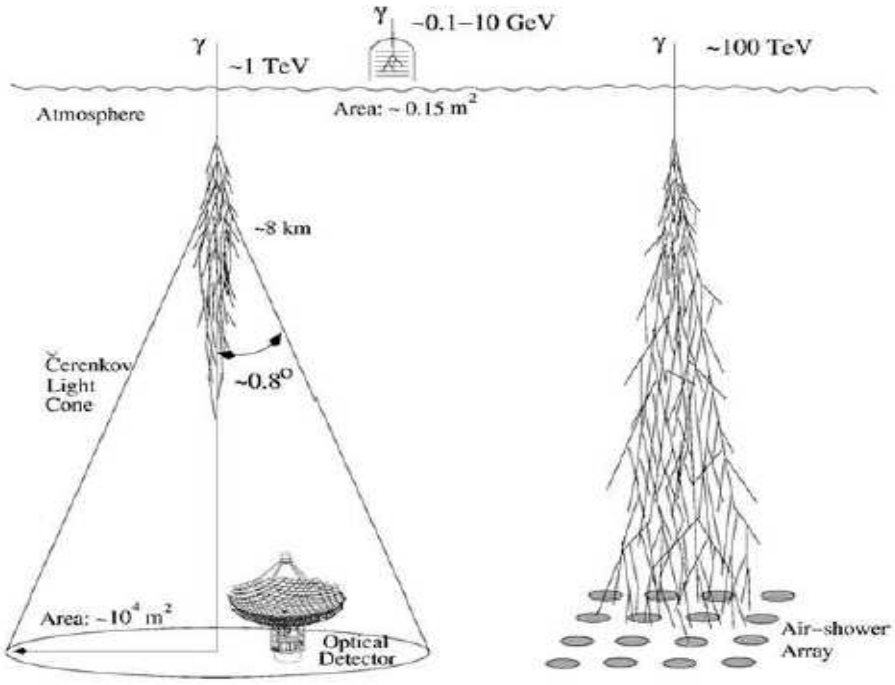

Figure 1.8: *Experimental techniques used for the detection of HE/VHE $\gamma-$rays. The picture (not in scale) gives the values of the effective collection areas, and the typical median energy to which the different kinds of detectors are sensitive.*

Since secondary particles in EAS propagate faster than the local speed of light in air, they emit Cherenkov radiation. Due to the small emission angle ($\sim 0.8^\circ$ at the depth of maximum size, see Fig. 1.8), the result at ground level is a light pool similar in size to the front of the EAS, with a density distribution almost flat out to $\sim 125\ m$ from the shower axis and with a tight time structure (few ns).

To better understand advantages and limits of the two techniques is useful to examine the characteristics of a ground-based detector with particular attention to the parameters that define its sensitivity.

1.3.3 General characteristics of ground-based detectors.

The ground-based detection of VHE photons is indirect: nature, direction and energy of the primary particle have to be inferred from the measurable properties of the secondary particles (in the case of EAS Arrays) or of the Cherenkov flash (for Cherenkov detectors).

The following relevant properties characterize a ground-based detector:

- **threshold energy**: given a minimum number of secondary particles (or Cherenkov photons) required to trigger the detector, the threshold energy is determined by the atmospheric absorption and by the detector layout. This implies that the threshold varies with the zenith angle because of the increasing thickness of atmosphere and that the threshold becomes lower with increasing altitude above sea level.

- **field of view (FOV)**: the FOV is the portion of the overhead sky that can be seen at a time. Therefore, it represents the spatial limit for the continuous monitoring of the sky.

- **duty cycle**: the fraction of time of actual data taking is the temporal limit to the continuous monitoring of the sky.

- **sensitivity to point-like sources**: the time needed to reveal a photon flux Crab-like at a significance level of 5 σ.

The main limitation of the ground-based γ-ray measurements is related to the difficulty into unambiguously identify and reject the charged cosmic ray background. This means that ground-based instruments detect a source as an excess of events from a certain direction over an overwhelming uniform background. For this reason their sensitivities are expressed in units of standard deviations of the CR background:

$$S = \frac{N_\gamma}{\sqrt{bkg}} \tag{1.2}$$

The sensitivity S depends essentially on the angular resolution since, at least for point sources, a better reconstruction of the direction produces a narrower spatial distribution of the signal (see Fig. 1.9) which can be more clearly distinguished over the background. The $\frac{signal}{\sqrt{bkg}}$ ratio can be expressed as a function of the γ and CRs fluxes and of the characteristics of the detector:

$$\frac{signal}{\sqrt{bkg}} = \frac{\Phi_\gamma(> E_{th})}{\sqrt{\Phi_B(> E_{th})}} \cdot \frac{A^\gamma_{eff}(> E_{th})}{\sqrt{A^B_{eff}(> E_{th})}} \cdot \sqrt{\frac{T \cdot f}{\pi}} \cdot \sqrt{(d.c.)} \cdot \frac{\epsilon(\Delta\theta)}{\Delta\theta} \cdot Q_f \tag{1.3}$$

where $\Phi_\gamma(> E_{th})$ and $\Phi_B(> E_{th})$ are the integral fluxes of γ and CRs for energies $> E_{th}$, $A^\gamma_{eff}(> E_{th})$ and $A^B_{eff}(> E_{th})$ are the "effective area" to reveal γ and CR-induced showers, $T \cdot f$ is the fraction of useful time of measurement, $(d.c.)$ is the duty-cycle, $\Delta\theta$ is the opening angle around the source direction and Q_f is the quality factor.

From this expression it is clear that the sensitivity of a detector mainly depends on:

- "Effective area" for $\gamma-$rays: the fact that the atmosphere can be considered a part of the detector itself allows for a further increase of the

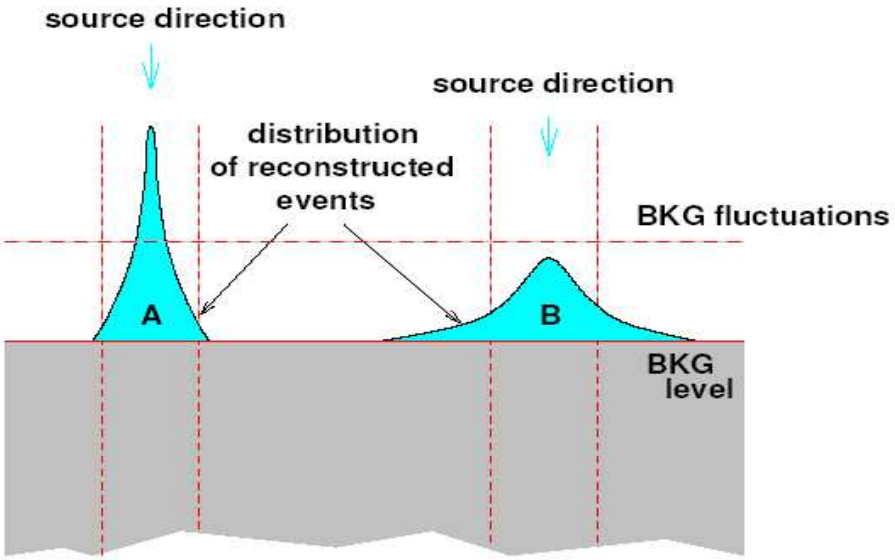

Figure 1.9: *Simplified two dimensional sketch showing that the direction reconstruction results in a distribution of events centered at the true source direction. A good angular resolution produces a narrow distribution (case A) that can be seen as an excess over the background fluctuation while in case B the excess is below the fluctuation level.*

detection area. At high altitude the effective area to reveal $\gamma-$rays $A^{\gamma}_{eff}(> E_{th})$ is higher than the one for cosmic rays.

- The angular resolution σ_θ related to the opening angle $\Delta\Omega$. If the point spread function of the angular resolution is gaussian $\sim e^{-\frac{\theta^2}{2\sigma_\theta^2}}$ the opening angle that maximize the $signal/\sqrt{bkg}$ ratio is given by $\Delta\theta = 1.58\sigma_\theta$ and it tallies with a fraction of $\epsilon = 0.72$ of the events from the direction of the source in the solid angle $\Delta\Omega = 2\pi(cos\Delta\theta)$. And so: $\frac{\epsilon(\Delta\Omega)}{\Delta\Omega} \simeq \frac{0.72}{1.6\sigma_\theta} = \frac{0.45}{\sigma_\theta}$. In the following the opening angle $\Delta\Omega$ which maximize the sensitivity will be called ψ_{70}.
- The energy threshold E_{th}.
- The Duty cycle.
- The "Quality factor" (Q_f): further improvements in the sensitivity level can be achieved by rejecting part of the background on the basis of subtle differences in the cascades initiated by photons and hadrons.

As can be seen from the equation (1.3) the sensitivity is inversely proportional to the angular resolution so it's a crucial parameter: for a given

sensitivity, a gain of a factor X in angular resolution entails a reduction of a factor X^2 in the data taking time.

As will be shown in the next sections, all these characteristics are significantly different in the two cases of atmospheric Cherenkov detectors and EAS arrays.

1.3.4 Atmospheric Cherenkov Telescopes

The most successful instruments in the history of VHE $\gamma-$ray astronomy have been the Imaging Atmospheric Cherenkov Telescopes (IACTs). These detectors typically make use of a parabolic or spherical mirror to focus the Cherenkov photons onto a tightly packed array of photomultiplier tubes (PMTs) placed in the focal plane. Properties of the primary particles can be inferred by the resulting image of the shower (see Fig. 1.10). IACTs are typically sensitive at energies greater than $200 - 300\ GeV$, have excellent angular resolution ($\sim 0.1^\circ - 0.15^\circ$) and moderate energy resolution ($\sim 20 - 40\%$). However their excellent results are actually due to their ability to perform an efficient γ/hadron separation using the shape of the image [34]: $\gamma-$rays give a smooth, elliptical image that points toward the center of the field of view, while CRs images are broader and more irregular[2]. IACTs can reject more than 99% of the background while retaining $\sim 50\%$ of the signal thus increasing sensitivity up to a factor $Q_f = 5$.

The most famous IACT is certainly the Whipple telescope (diameter 10 m), which developed the imaging technique. Other successful IACTs are CAT (Pyrenees, 3 m), CANGAROO (Australia, 3.8 m) and HEGRA that uses 5 mirrors (3 m). The technique is being developed in two different directions: MAGIC will use a single enormous mirror (17 m diameter) to reduce the energy threshold at $20 - 30\ GeV$, while experiments like VERITAS (Arizona, 7×12 m mirrors) and HESS (Namibia, 4×12 m) make use of arrays of traditional reflectors to obtain a stereoscopic view of the shower. Another group of Cherenkov detectors includes the solar towers as CELESTE, STACEE and Solar2. Pre-existing arrays of heliostat mirrors (used in solar power plants) are utilized to focus the Cherenkov light on a secondary mirror which in turn reflects the radiation onto an array of PMTs. The advantage is the very large mirror area that can be instrumented at low cost. This approach allows reaching low threshold energies ($20 - 50\ GeV$). Recently the first ground-based observations of the Crab Nebula in this energy range have been published by STACEE [35] and CELESTE [36]. Both IACTs and solar towers reach a sensitivity of $\sim$ % of Crab units but they have two

[2] Actually the background rejection makes indirectly use of the direction reconstruction: requiring that the axis of the elliptical image intersects the center of the FOV is equivalent to the selection of showers whose direction is parallel to the mirror axis (i.e. primary particles coming from the pointed direction). Indeed the background rejection is not so good in the case of diffuse sources.

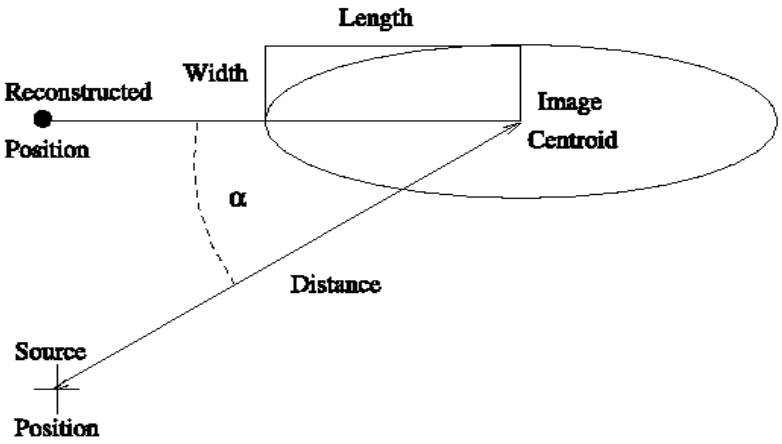

Figure 1.10: *Scheme of the elliptical image produced by an air shower on the pixel camera of a IACT. The point marked as "source position" represents the center of the pixel camera. The Hillas parameters, defined here, are used to perform background rejection.*

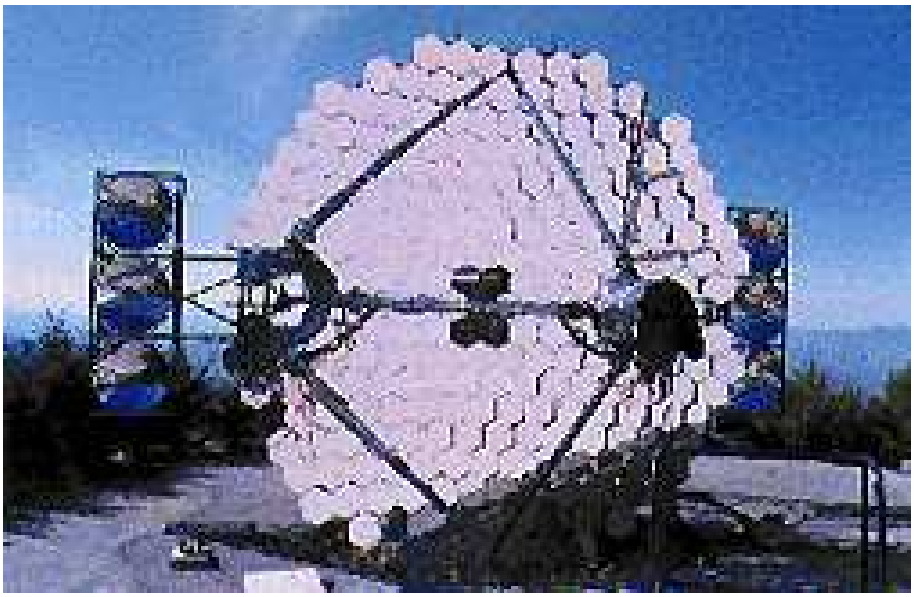

Figure 1.11: *The 10 m diameter Whipple reflector (Mt. Hopkins, US). This detector was the first to successfully experience the imaging technique.*

important limitations. Due to the small FOV ($< 5°$) they must be pointed. Furthermore, they have a low duty cycle ($< 10\%$) since Cherenkov radiation can be detected only during moonless cloudless nights. Given that the flux from TeV sources is generally highly variable, these limitations make the identification of new sources and the observation of flaring states of known sources difficult.

1.3.5 Extensive Air Shower Arrays

Instruments that detect the secondary charged particles reaching the ground level are known as EAS arrays. Typically they consist of a number of charged particle detectors, usually 1 m^2 scintillation counters, spread over an area of $10^4 - 10^5$ m^2 with a spacing of $10 - 20$ m. The total sensitive area is therefore less than 1% of the total enclosed area. The shower is sampled at a single depth (the observational level) and with an additional sampling of the shower front at fixed points. This results in a high degree of uncertainty in the reconstruction due to fluctuations[3].

The sparse sampling sets the energy threshold and determines a poor energy resolution ($\sim 100\%$). The direction of the incoming primary particle is reconstructed with the fast timing method making use of the relative times at which the individual detection units are fired by the shower front. Also the angular resolution is limited by the shower fluctuations ($\sim 1°$). In few arrays the measurement of the muon content may allows for background rejection. However the ability to discriminate γ and hadron induced showers is quite limited.

In addition dependence of threshold and reconstruction capabilities on the zenith angle is higher than for Cherenkov detectors: since the active area is horizontal, its projection onto a plane perpendicular to the shower axis is smaller than the geometrical area[4]. On the other hand, EAS arrays have a large field of view (~ 2 sr) and a 100% duty cycle. These characteristics give them the capability to serve as all-sky monitors.

1.4 New generation EAS arrays

In order to meet the requirements of high duty cycle, large field of view and low energy threshold, new EAS arrays have been constructed in the last decade. Indeed, the need to measure showers induced by cosmic rays

[3]For a comparison, Cherenkov detectors record information related to the whole longitudinal and lateral development of the shower summarized by the elliptical image on the pixel camera.

[4]Cherenkov telescopes point the source therefore their area is always orthogonal to the shower axis. The degradation of the detector performance with zenith is simply due to the increasing thickness of atmosphere.

with energies less than 1 TeV imposes the construction of unconventional air-shower arrays at very high altitude.

Two experiments presently in operation follow, separately, these requirements: the Tibet AS-γ detector is located at very high altitude but is a traditional discrete air shower array; the MILAGRO detector is a full coverage apparatus but is located at modest altitude (2600 m a.s.l.).

The Tibet AS-γ experiment is a hybrid apparatus consisting of emulsion chamber (EC), burst detectors (BD) and an air shower array carried out at Yangbajing (4300 m a.s.l.) [37]. The array is traditional but with a high density distribution of detectors: 221 scintillation counters of 0.5 m^2 each of which are placed on a 7.55 m square grid with an enclosed area of 22050 m^2 (see Fig. 1.12) [38]. Any fourfold coincidence in the detectors is used as the trigger condition for air-shower events. Under this condition the trigger rate is about 200 Hz with a dead time of about 12% for data taking. The energy threshold is estimated to be about 7 TeV for proton-induced showers. The precision of the shower direction determination is about 1°, which has been confirmed by observing the Moon's shadow. The energy resolution is estimated to be 17% at energies around 10^{15} eV. The ECs and the BDs are constructed near the center of the AS, and are used to detect high-energy air shower cores accompanied by air showers induced by primary cosmic rays with energies above $\sim 10^{14}$ eV. The total area of ECs is 80 m^2.

The Milagro Gamma Ray Observatory [39] is a large field-of-view telescope designed to to detect gamma rays near 1 TeV using water Cherenkov techniques to observe air shower particles that survive to the ground level. It is located at a latitude of 36° and an altitude of 2630 m in the Jemez Mountains, New Mexico, USA. A 60 m $\times$ 80 m $\times$ 8 m covered pond, filled with clear water, is instrumented with 723 20-cm photomultipliers (PMT) (see Fig. 1.13). A top layer of 450 PMT's is used to reconstruct the shower direction with a resolution of about 0.75° from the relative PMT timing. A bottom layer of 273 PMT's is used for discrimination between gamma-ray and the dominant hadron-induced air showers. A *Compactness* cut rejects about 90% of the hadronic background and retains about 45% of the gamma-ray signal for typical gamma-ray source spectra [40]. The effective area of Milagro ranges from $\sim$10 m^2 at 100 GeV to $\sim 10^5$ m^2 at 10 TeV. The angular resolution is approximately 0.7 degrees. The energy (E_5) above which 95% of the triggered events from such a spectrum are obtained is approximately 250 GeV, the energy (E_{95}) below which 95% of the triggered events come is 25 TeV, and the median energy is 2.5 TeV.

As discussed in section 1.2 the all-sky surveys performed by these two experiments revealed no previously unknown significant $\gamma-$ray sources (both apparatus detect emission from Crab Nebula and Mrk 421). Indeed, the sensitivity obtained by these surveys is rather limited, reaching a flux limit comparable to $\sim$ 0.5 the flux of the Crab Nebula in about 3 years of data taking. As a consequence, there are no strong unknown point sources of

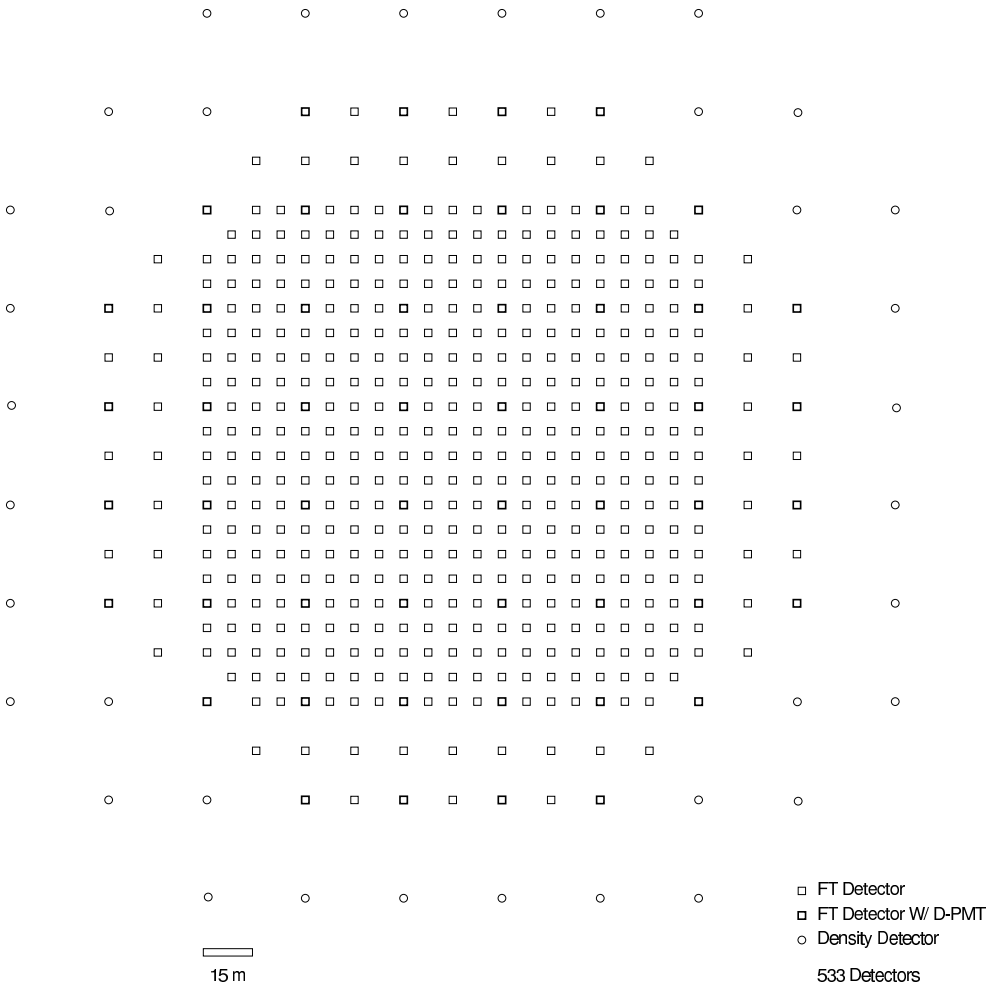

Figure 1.12: *The Tibet AS-γ layout. It is a hybrid apparatus consisting of emulsion chamber (EC), burst detectors (BD) and an air shower array.*

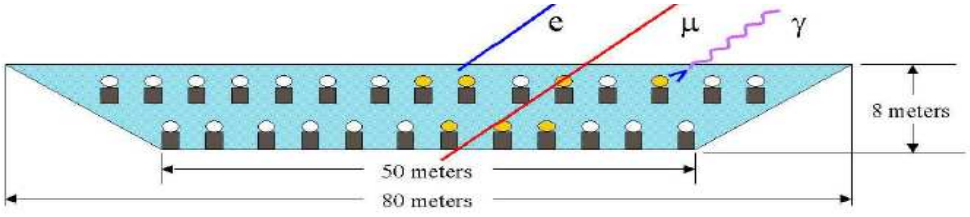

Figure 1.13: *Scheme of the MILAGRO detector cross-section. PMTs are deployed into a man-made pond filled of water.*

VHE gamma rays.

The ARGO-YBJ detector will meet simultaneously the requirements of very high altitude location and full coverage approach. The characteristics of the detector and performance will be discussed in the next chapter. ARGO-YBJ will allow a continuos monitoring of the sky with a sensitivity better than 0.3 Crab units at 1 TeV, without any $\gamma/hadron$ discrimination procedure.

This thesis is based on the study of the angular resolution of the ARGO-YBJ detector. Since December 2004 to July 2005 ARGO-42, a carpet of about 1900 m^2 of RPCs (42 Clusters, $\sim 47 \times 41$ m^2, corresponding to about 1/3 of the whole central detector) has been put in stable data taking. The analysis carried out in this thesis concerns the data recorded in this period.

The angular resolution has been studied in two independent ways:

- comparing the accuracy of the arrival direction reconstruction of the primary particle by MonteCarlo simulations and data collected with ARGO-42 (see chapter 3);
- analyzing the shadowing effect of cosmic ray from the direction of the Moon (see chapter 4).

1.5 Moon shadow concept

A point source is inferred from an excess of showers arriving from a particular direction of the celestial sphere. Owning to the finite instrumental resolution, showers from a point source appear to arrive from a finite region of the sky and are therefore accompanied by a background of nearly isotropic cosmic rays. An accurate determination of both signal and background from a particular direction therefore requires a good understanding of the angular resolution of the detector. Indeed, the better the angular resolution, the smaller the required search region around a putative source, and thus the lower the background. For a point source, the signal/background ratio is in inverse proportion to the square of the angular resolution.

As a consequence it is important to verify that the apparatus is operating with the estimated angular resolution, and that no significant systematic "pointing" errors are present.

As first suggested by Clark in 1957 [4], the cosmic ray anti-source of the Moon or Sun may be treated as a fiducial object. Since the Moon and Sun each have an angular radius of approximately 0.26°, they must cast a shadow in the high-energy cosmic ray flux (this is the so-called *"shadow of the Moon"*, see Fig. 1.14). The shadowing of cosmic rays from the direction of the Moon or Sun is therefore useful in measuring the angular resolution of an array directly, without the need to invoke MonteCarlo simulations. Observing the expected depth of shadowing also verifies the array pointing accuracy and stability.

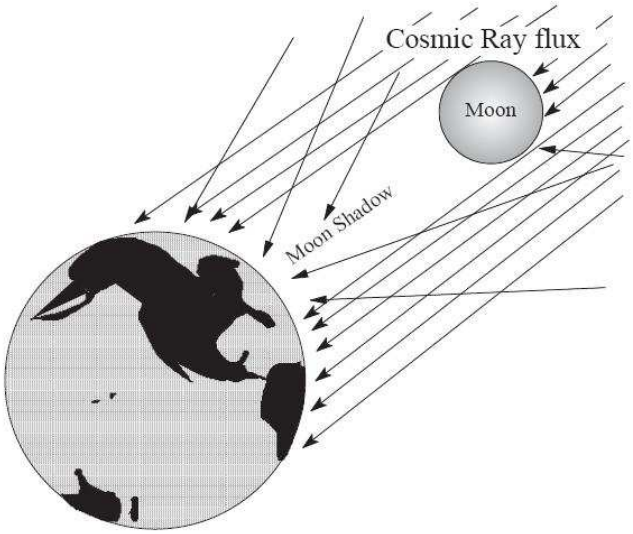

Figure 1.14: *A schematic diagram of how the Moon shadow is created.*

In principle, the size of the deficit gives us information about the angular resolution while the position of the dip provides information about the pointing error.

However, a large sample of events is necessary to obtain a statistically significant result, because the dip in intensity is small. Indeed, the first observation of such a shadowing had to wait for the results of the CYGNUS collaboration in 1991 [8]. They showed a deficit of events 4.9σ below the cosmic ray background.

There are two reasons for this long delay. First, the particles must be insensitive or weakly sensitive to the Earth magnetic field. Obvious candidates are γ-rays or energetic cosmic ray particles. The former are very rare and the observation of the latter above the nearly-isotropic large background of low-energy cosmic rays, was only possible with the advent of EAS arrays able to collect high statistics. Second, a crucial parameter is the angular resolution of the detectors. The signal over background ratio is inversely proportional to the square of this angular resolution and events are spread out from the expected position due to the finite angular resolution. The performance of the detector has to cope with the angular radius of the Moon (or the Sun), each having approximately a 0.26° radius, and only at the begin-

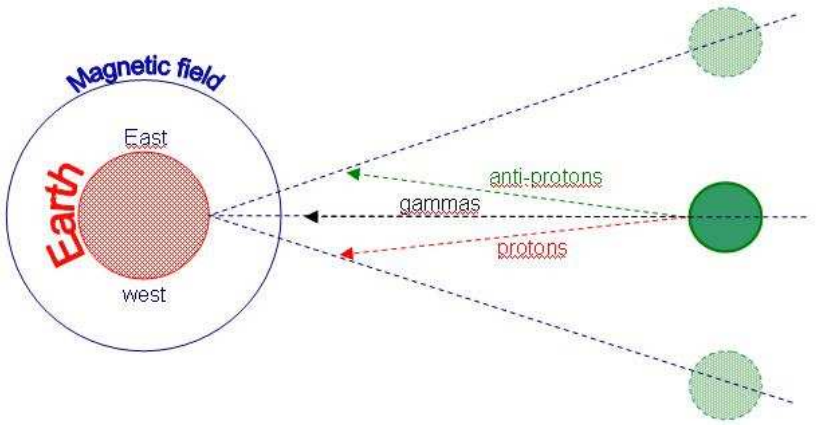

Figure 1.15: *The joint effect of bending and absorption produces a frequency "dip" toward a misplaced Moon [46].*

ning of the 90's, the angular resolutions of cosmic ray detectors reached the one-degree level. Since then, several other experiments, both EAS arrays and large underground detectors have been able to see the Moon-shadow effect [41, 42, 43, 44, 45].

1.5.1 Earth magnetic-field and calculations of the deflection

Almost all the cosmic rays are charged and therefore bend under the influence of solar and terrestrial magnetic fields. Particles with small total energy or large electric charge have low magnetic rigidity and will bend more. During its way from the Moon to the Earth, a particle of charge Z and energy E is subject to the Lorentz force in the field $\vec{B}$ and the deflection $\Delta\theta$ is linked to the particle path l, as:

$$\Delta\theta(mrad) \quad = \quad 0.3 \cdot \frac{Z}{E(TeV)} \cdot \left| \int \vec{B}(Tesla) \times d\vec{l}\,(m) \right| \simeq \frac{1.7^\circ\ Z}{E(TeV)} \quad (1.4)$$

As a consequence, the geomagnetic deflection of cosmic rays can be observed in the shadow of the Moon as a displacement $\Delta\theta$ of the center of the deficit of events relative to the true position of the Moon. Therefore, for different particles the magnetic field produces different displacements. As can be seen in the Fig. 1.15, protons are deflected eastward, so that the "dip" in the occurency frequency of cosmic rays due to the Moon absorption is displaced to the West. The opposite occurs to antiprotons.

Depending on their incident direction at the top of the atmosphere, charged particles traverse different field regions. Thus, for a given particle, the angular deflection is a function of the incident direction, the charge

and the energy of the particle. This can be used to establish a deflection map that gives, for a given energy, the amount of deflection and its direction.

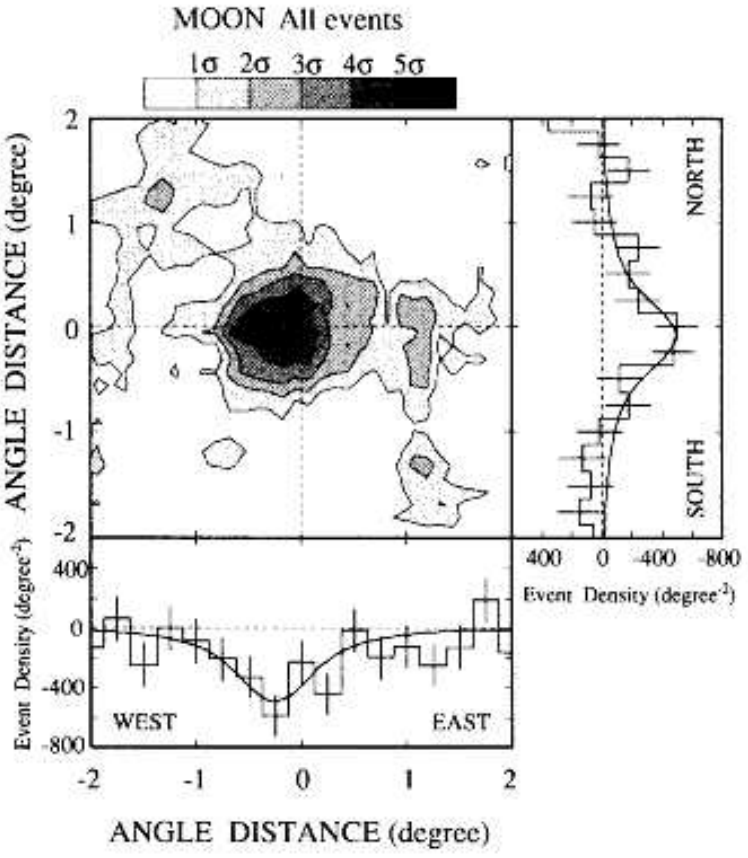

Figure 1.16: *Arrival direction of all events in the area of* $4^\circ \times 4^\circ$ *centered on the Moon (see text).*

As example, a proton with energy 100 TeV will deflect in angle by $\sim \frac{1.7^\circ}{100} = 0.017^\circ$, and an iron nucleus will deflect in angle by $26\times \sim \frac{1.7^\circ}{100} = 0.42^\circ$ along the Moon to Earth trajectory.

The effect of the geomagnetic field in the shadow of cosmic rays by the Moon is shown in Fig.1.16, where the arrival direction of all events in the area of $4^\circ \times 4^\circ$ centered on the Moon is displayed. The map gives the weight of the deficit event density from the background as detected by the Tibet ASγ experiment [47]. The contour lines start from 1σ deficit with a step of 1σ. Shown on the outside of the map are the deficit event densities against the angle distance from the Moon center on the belt of width 1° along the

right ascension (West-East) and the declination (South-North).

A slight deviation of the shadow from the Moon center is seen in this figure. As the profile of the Moon's shadow in the North-South direction is almost free from the effect of the geomagnetic field, the deviation of the highest deficit position from the center of the Moon gives an estimate of the systematic pointing errors of the array.

On the contrary, the profile in the East-West direction is slightly affected by the geomagnetic field when the energies of cosmic rays are not so high (the median energy of these events is about 17 TeV). As seen in Fig.1.16, the profile of the Moon's shadow is broadened in the East-West direction, with a systematic shifted towards the West. Indeed, the geomagnetic field would bend incident positively charged cosmic rays to make their apparent arrival direction shift to the West. The solid curves in the figure show the event density expected from the angular resolution of 0.87°.

Therefore according to the eq. 1.4, high energy cosmic rays are less bent by the geomagnetic field, the Moon shadow is about in the nominal position and its shape is less broadened. The shadow of the Moon for high energy cosmic rays ($E > 10 - 15\ TeV$) is a good tool to measure the angular resolution of an EAS array and to study the systematic pointing errors. Moreover low energy particles ($E \leq 1\ TeV$) are deviated of $\Delta\theta \geq 1.7°$ toward east and anti-particles are deviated of $\Delta\theta \geq 1.7°$ westward. Consequently the shadow of the Moon for low energy cosmic rays permits to estimate the antimatter/matter ratio, and in particular the $\bar{p}/p$ ratio (see [9, 48]).

Chapter 2

The ARGO-YBJ experiment

The ARGO-YBJ (Astroparticle Radiation with Ground-based Observatory at YangBaJing) experiment is a full-coverage air shower detector devoted to the study of cosmic rays, mainly γ radiation, of very low energy, i.e. with an energy threshold of a few hundreds GeV.

The scientific motivation of such an apparatus is to perform a continuous all-sky survey of the Northern hemisphere with a high sensitivity (better than 0.3 in Crab units at 1 TeV) to search cosmic ray sources through the detection of their γ-rays emission.

The need to measure showers induced by cosmic rays with energies less than 1 TeV imposes the construction of an unconventional air-shower array at very high altitude. In fact, at these energies the shower particle content is too small to reconstruct the EAS observable with a typical array made of several detectors spread over a large area sampling only about 1% of the shower size. Only the exploitation of a full coverage approach can provide the required high granularity sampling of particle showers. Such a detector improves the angular resolution and lowers the energy threshold. In addition, a large sensitive area allows, in principle, topological studies of particle density distributions useful to investigate the differences between γ and hadron-induced showers, important for the rejection of the background in γ-ray astronomy.

At high altitude: (1) the shower fluctuations are reduced since the detector approaches the depth of the maximum longitudinal development; (2) the reduced attenuation in the atmospheric overburden allows one to observe EAS primaries with low energy ($\sim$ TeV), thus approaching the direct measurements; (3) the ratio of effective areas for γ and hadron-induced showers $\frac{Aeff^{\gamma}}{Aeff^{h}} \gg 1$ improves the photon detection capability.

In addition: (4) the average shower size in the knee region of the cosmic ray spectrum ($E \simeq 10^{15}\ eV$) is almost the same for both proton and iron primaries, providing a composition independent estimator of the energy; (5) the energy flow in the core region of EAS is less attenuated and easier to

Sampling	Altitude	E_{th}
discrete	2000 m	$\sim$ 50 TeV
discrete	4300 m	$\sim$ 3 TeV
full coverage	2000 m	$\sim$ 3 TeV
full coverage	4300 m	$\sim$ 300 GeV

Table 2.0.1: *Energy thresholds E_{th} for different sampling typology and altitude of the detector.*

observe. As an example, at 4300 m a.s.l. for showers with the knee energies the energy flow of the electromagnetic component within 1 m from the core is 30-40 times higher than that at sea level [49]. These features can be exploited for a measure of the cosmic ray composition in the energy range $10^{14} - 10^{16}$ eV.

Two experiments presently in operation follow, separately, these requirements: the Tibet AS-γ detector is located at very high altitude but is a traditional discrete air shower array; the MILAGRO detector is a full coverage apparatus but is located at modest altitude (2600 m a.s.l.). In Table 2.0.1 the dependence of the energy thresholds of an apparatus on the sampling typology and detector altitude is reported.

The ARGO-YBJ experiment can meet simultaneously these requirements. This experiment will image with high efficiency and sensitivity atmospheric showers initiated by primaries of energies $\geq$ 300 GeV, allowing to bridge the GeV and TeV energy regions and to produce data on a wide range of fundamental issues in cosmic ray physics and γ-ray astronomy.

2.1 The ARGO-YBJ experiment

The ARGO-YBJ experiment is located at the YangBaJing High Altitude Cosmic Ray Laboratory (Tibet, P.R. China, 4300 m a.s.l.). The site location (latitude 30° 06′ 38″ N, longitude 90° 31′ 50″ E) will allow the monitoring of the Northern hemisphere in the declination band $-10° < \delta < 70°$.

The ARGO-YBJ apparatus consists of a full coverage array of dimension $\sim 74 \times 78$ m^2 realized with a single layer of Resistive Plate Counters (RPCs), 280×125 cm^2 each. The area surrounding the central detector core, up to $\sim 100 \times 100$ m^2, is partially ($\sim 50\%$) instrumented with RPCs (see Fig. 2.1). This outer ring improves the apparatus performance, enlarging the fiducial area for the detection of showers with the core outside the full coverage carpet.

A lead converter 0.5 cm thick will cover uniformly the RPCs plane. In this way the number of charged particles is increased by conversion of shower photons, thus lowering the energy threshold and reducing the particle time

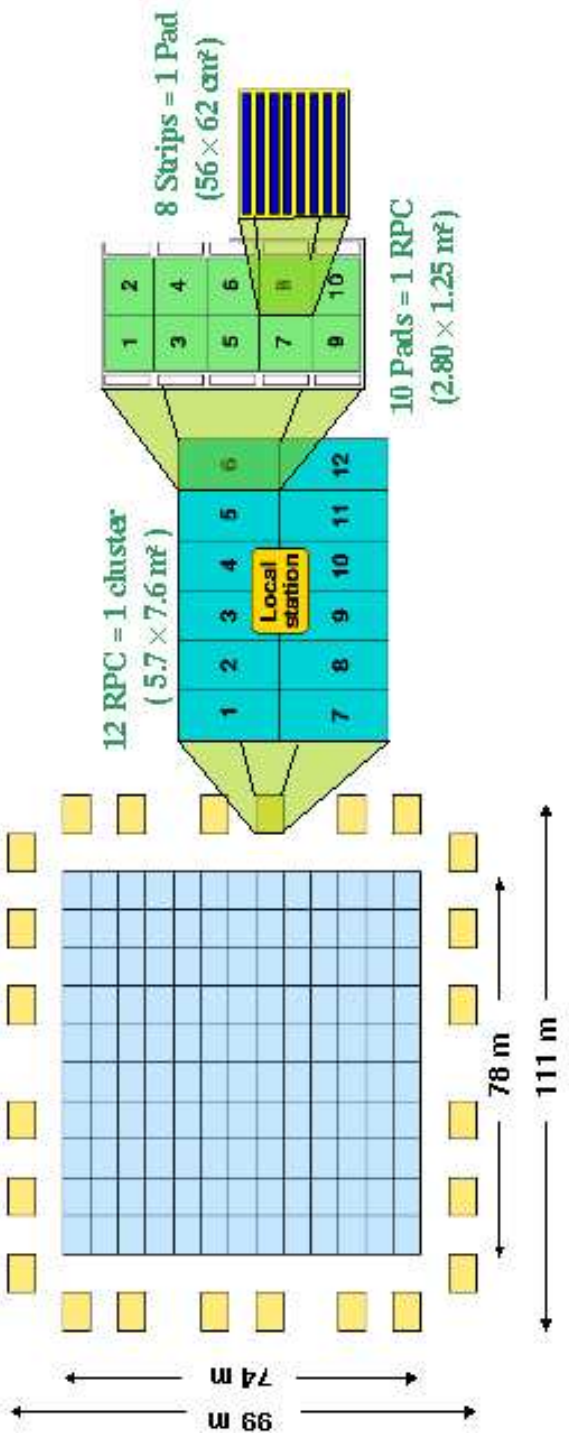

Figure 2.1: *The ARGO-YBJ layout showing the division into physical (RPCs and strips) and logical (pads and Clusters) units.*

fluctuations on the shower front.

The RPC signals are picked up by means of strips 6.7 cm wide and 62 cm long. The strips (124800 in total in the carpet) are the basic element which defines the space pattern of the shower. The fast-OR signals of 8 strips are used for time measurements and trigger purposes. These OR-ed strips define a logic PAD of 56×62 cm^2 (15600 in total in the carpet), which is the basic element (the "pixel") providing the time pattern of the shower. Both environmental and detector parameters, namely atmospheric pressure, external air temperature, high voltage power supply, current drawn by each RPC, gas temperature and humidity, are continuously monitored.

The time resolution (~ 1 ns, see Fig. 2.1) and the small temporal (the pad) and spatial (the strip) pixels, allow to image the shower front with an unprecedented space-time granularity. An example of the high accuracy sampling capability of the ARGO-YBJ carpet is shown in Fig.2.2 and Fig. 2.3 where the pictures of air shower events recorded by the pad system of 42 Clusters are displayed.

This digital response of the detector can be used up to energies of a few hundreds of TeV. In order to extend the dynamic range, a charge read-out has been implemented by means of two large size pads of dimension 140×125 cm^2 each (Big Pad) [50] (see section 2.5).

The RPC consists in two bakelite (phenolic polymers with high resistivity $\rho \geq 5 \times 10^{11} \Omega cm$) electrode plates $2mm$ thick whose area is $125 \times 280 cm^2$. They are separated by a $2mm$ gap filled with gas. The RPCs operate in streamer mode with a gas mixture of Ar (15%), C_4H_{10} (10%) and $C_2H_2F_4$ (75%) specifically studied for the operation at extreme environmental conditions (low atmospheric pressure and low temperature). At the YBJ site, the detection efficiency of charged particles is 95% at an operating voltage of $\sim 7kV$.

In Fig. 2.4 the chamber layout is shown. Each RPC is assembled in a box of $285 \times 122.5 \times 0.47 cm^3$. Two external shaped rigid panel of an Aluminium foil (200 μm thick) foil, glued on a 1.5 cm foam layer, are used as a protection for the gas volume and to fix the chamber elements. According to the figure each chamber consist of:

- rigid panel
- copper foil (17 μm thick) glued on a PET foil (190 μm) used for analog read-out of the total induced charge produced in the gas volume (Big Pad)
- 3 mm thick foam layer glued on PET foil (250 μm)
- gas volume
- strip panel

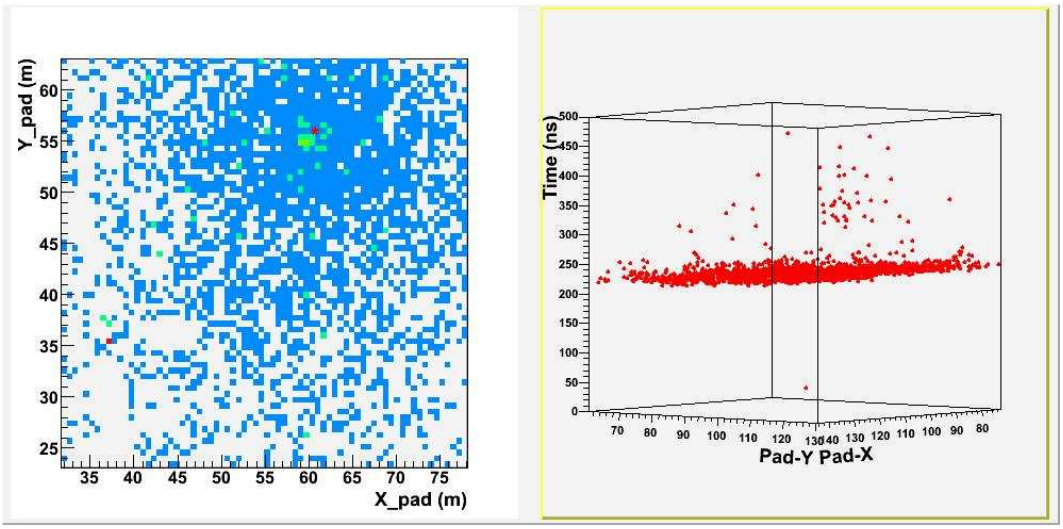

Figure 2.2: *Space (left) and space-time (right) view of a shower.*

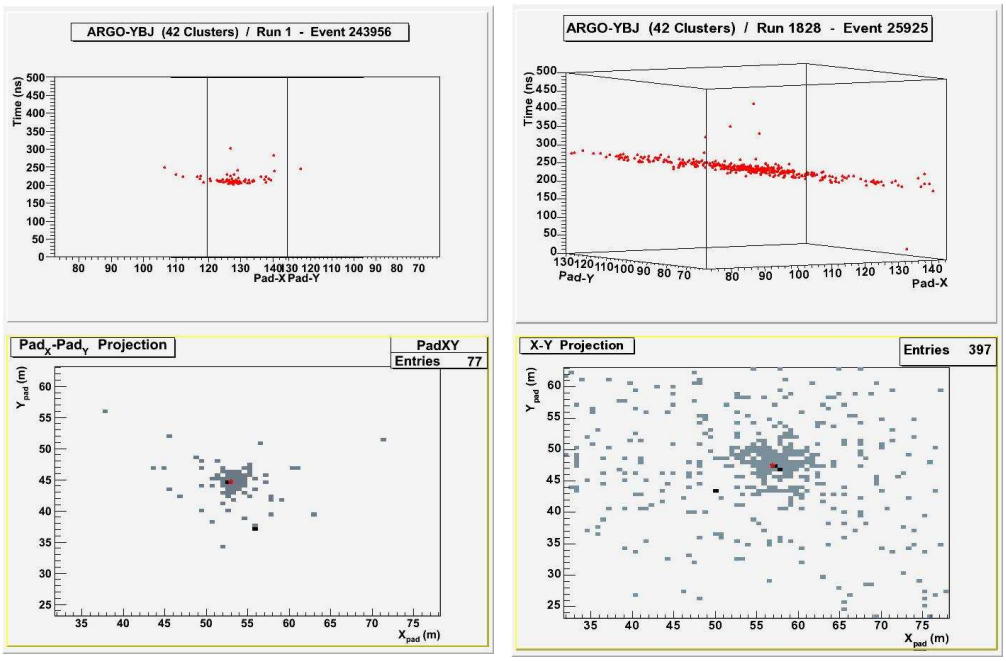

Figure 2.3: *Space (bottom) and space-time (top) view of two showers.*

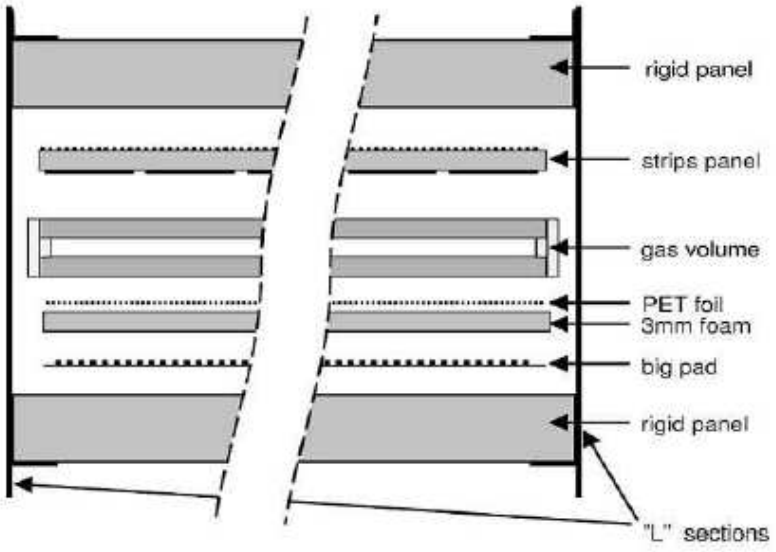

Figure 2.4: *Layout of the RPC used in the ARGO-YBJ.*

- rigid panel

The basic detection unit is the Cluster, a set of 12 contiguous RPCs (the rectangles of Fig.2.1). The signals from each Cluster are organized by a front-end pre-processing electronics ("Local Station", LS) in order to give a continuous counting of the fired pads ("pad multiplicity") in a narrow time window ($\Delta t = 150$ ns). This information is transferred to the "Central Station" for trigger purposes. At any trigger occurrence, the space and time information from each LS is collected and elaborated in the Central Station for event building and storage.

Presently (Nov. 2005) 102 clusters of the central detector carpet have been installed and 74 of them are in data taking for debugging. Since December 2004 to July 2005 ARGO-42, a carpet of about 1900 m^2 of RPCs (42 Clusters, $\sim 47 \times 41$ m^2, corresponding to about 1/3 of the whole central detector) has been put in stable data taking, yet without any converter sheet [51]. The analysis carried out in this thesis concerns the data recorded in this period.

The central carpet will be completed and put into stable data taking early in the summer 2006.

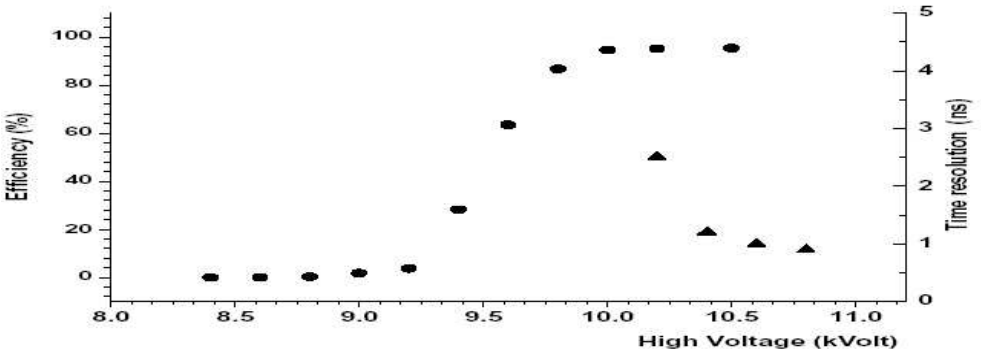

Figure 2.5: *Efficiency and time resolution of the ARGO-YBJ chamber at sea level.*

2.2 RPC performance

The RPC efficiency and time resolution have been measured with a telescope realized by three scintillation counters and two RPCs. The coincidence of the three scintillators define the trigger signal used as a common stop for the TDC board. The efficiency and the time resolution have been measured using the lower RPC in coincidence with this trigger signal. The performance of the upper RPC has been measure as a function of the applied high voltage (HV). The efficiency has been obtained by comparing the upper RPC signal with the signal of the three scintillators in coincidence with the lower RPC. The time resolution has been measured unfolding the time signals of both RPCs. All measurements have been performed operating the RPCs in streamer mode with a standard gas mixture ($Ar/Isobutane/R134A = 10\%/15\%/75\%$).

The results are shown in Fig. 2.5. As expected, the plot shows an efficiency curve with a well defined and wide plateau starting at $\sim 10\ kV$ ("knee"). The efficiency measured in the plateau region is close to geometrical acceptance value, while the time resolution obtained is $\sim 1\ ns$ at a high voltage of $\sim 500\ V$ after the "knee" value [52].

2.3 Trigger logic

Three different trigger subsystems have been implemented: (1) Low Multiplicity Trigger (LMT), (2) Fast Trigger (FT), (3) High Multiplicity Trigger (HMT). All these triggers are based on the fired pads counters generated by the LSs on a given number of Clusters. These counters are two and they are used for trigger purposes with the following scheme: LMT and FT (from ≥ 1 to ≥ 6), HMT (≥ 7, ≥ 16, ≥ 32, ≥ 64). The Fast Trigger, which sums up

the counts of 4 Clusters (a "Supercluster") greater than a selected threshold, is very efficient for low energy events. A detailed description of the trigger and DAQ setup can be found in [53].

All the trigger algorithms validate and select an event on the basis of the time distribution of the fired pads and their multiplicity on the carpet. The performance of the trigger has been tested to select low energy showers in the range of a few hundreds GeV which are expected to fire less than 100 pads on the entire carpet. Beside this low multiplicity channel there are others triggers to select showers which have a much higher particle density [54].

A simple yet powerful algorithm to select shower events is achieved just adding the multiplicities of all Clusters corresponding to the same shower across the entire carpet in $\sim$ 400 ns. The spurious signals of the detector ($\sim$400 Hz/pad) represent the noise for the shower events. To keep them as low as possible, a four-level coincidence scheme has been implemented in order to correlate only pad signals of adjacent areas [54].

This logic produces an output when the total number of hits exceeds the programmed threshold (N_{trg}). This inclusive trigger $N_{trg} = 60$ has been used to collect data with ARGO-42.

The triggering efficiency as a function of the shower energy is shown in Fig. 2.6 for different trigger conditions. For $N_{trg} = 10$ we observe a "tail" due to a spurious contribution from the pad noise. Accordingly, a "noiseless" trigger is obtained by setting $N_{trg} = 20$. The curves of the Fig. 2.6 have been folded to the Crab-spectrum [55] to get the effective energy spectrum sampled by different trigger conditions. The result is shown in Fig. 2.7. A median energy of about 500 GeV is achieved by using the most inclusive triggers ($N_{trg} = 30$). Similar calculations have been carried out to evaluate the maximum trigger rate of the DAQ system. The present estimate takes into account only proton and helium induced showers. The proton and helium fluxes are from [56]. After integration on energy up to 100 TeV and over the solid angle up to $\theta_{max} = 50^{\circ}$ we obtain the trigger rate shown in Fig. 2.8 as a function of the inclusive threshold N_{trg}. In this figure the proton and helium contributions from "internal" and "external" events (cores inside and outside the carpet) are singled out. Taking into account the contribution of heavier nuclei, we can state that the trigger rate with the most inclusive thresholds should not exceed 10 kHz.

A check of these calculations has been performed by simulating the expected trigger rate for the 42 clusters in data taking from December 2004 to July 2005. The measured trigger rate is compared in Fig. 2.9 to the calculated values. The agreement is remarkable, the slight difference at high trigger thresholds likely being due to the contribution of the cosmic ray heavy components.

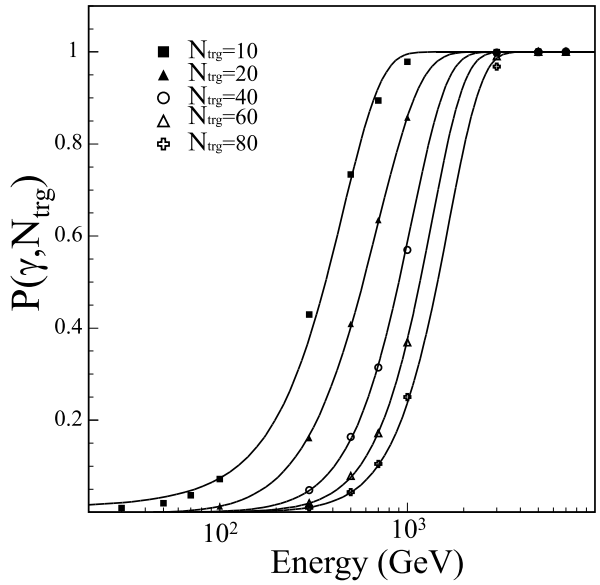

Figure 2.6: *Trigger efficiency $P(\gamma, N_{trg})$ vs. energy for γ-induced showers at zenith angle=20° ("internal events").*

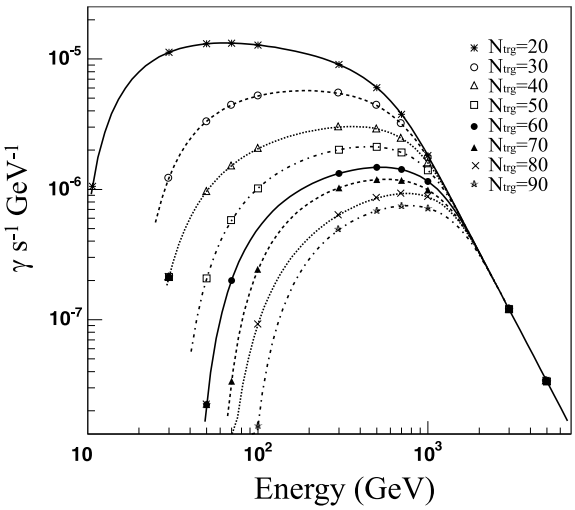

Figure 2.7: *The energy spectrum sampled at different trigger thresholds. The median energies range from 490 GeV for $N_{trg} = 20$ to 1650 GeV for $N_{trg} =$* 90.

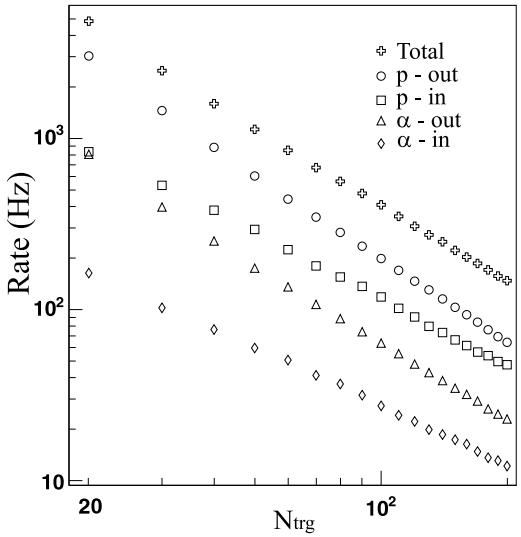

Figure 2.8: *Trigger rate (full ARGO carpet) induced by protons (p) and Helium nuclei (α): in=internal events and out=external events.*

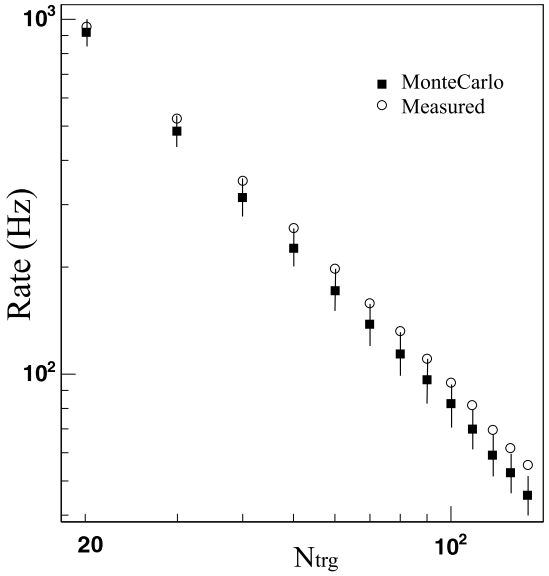

Figure 2.9: *Trigger rate vs. trigger threshold for the ARGO-42. The measured rate is compared to the one expected according to MonteCarlo simulations.*

2.4 Observational Techniques

The full coverage approach and the high altitude location allow the study of many physics items in the field of low energy cosmic rays. As a consequence, two main operation modes have been designed for the ARGO-YBJ detector:

- **Shower mode**: Based on the requirement that a minimum number of pads (N_{pad}) must be fired in the central carpet with the proper space-time pattern. For these events the position and time of any fired pad will be recorded to reconstruct the shower parameters (core position, arrival direction and shower size). The shower data will be used in γ-ray astronomy and in cosmic ray studies. The expected trigger rate is $\sim 10^3$ *events* s^{-1}, for $N_{trg} = 60$. From Monte Carlo simulations we infer that the trigger condition $N_{trg} = 60$ corresponds to explore a Crab-like γ-ray source spectrum with energy threshold $\sim$ 200 GeV and median energy $\sim$ 500 GeV, by selecting internal events. With such a multiplicity threshold ARGO-YBJ can achieve a pointing accuracy better than 1°, and a sensitivity to such a point source of at least 10 σ in 1 year of data taking (without considering any quality factor coming from γ/hadron primary discrimination).

- **Scaler mode**: The counting rate of the single particles, 2-particles, 3-particles and 4-particles on each cluster in 150 *ns* coincidence time, hitting the detector is recorded at fixed time intervals (0.5 *s*). An excess is registered if the counting rate is significantly higher than the background. This simple technique allows the detection of secondary particles from very low energy showers (E > 10 GeV) that reach the ground in a number insufficient to trigger the detector operating in shower mode. The arrival direction is not measured. The single rate measurement will be used to search for low energy transient phenomena such as GRBs or Solar Ground Level Enhancements, and to study cosmic ray modulations due to solar activity. Moreover, the same data can be used to check the detector stability. The expected rate is $5 \cdot 10^6$ events s^{-1}.

  With this simple technique, a good sensitivity at low energies can be achieved; MonteCarlo calculations show that even considering a low multiplicity for the shower mode trigger ($\geq$ 6), the scaler mode is more sensitive for energies ranging below 100 *GeV* [57, 58]. Since the counting rates for different multiplicities correspond to different mean energies of incoming primaries, if a positive detection is obtained it is possible to give an indication of the signal energy spectrum. As an example, a rough measurement of the mean primary energy can be done comparing the ratio ≥ 2 to ≥ 1 counting rates with MC predictions. Since this ratio depends on the primary energy, even if slightly, increasing for protons from 5.8% at 10 GeV to 6.8% at 100 GeV and

12.9% at 1 TeV, the measured ratio of 5.4% is consistent with the quoted 10 GeV mean energy of primary particles. Conversely, since the arrival direction of the incoming signal can not be determined, an independent confirmation by a directional detector is required even if a big excess is detected.

The validity of this approach is confirmed by a variation of the signal counting rate correlate with a forbush decrease observed by ARGO-42 [59].

2.5 Analog read-out

A brief description of the analog read-out of the RPCs is presented. The energy spectrum of cosmic rays is well described by a power law over several decades of energy, before and after the knee region, $10^{15}-10^{16}$ eV, where the slope changes. The origin of this steepening, observed indirectly in the EAS data, is still obscure, and it has been the subject of many speculations on the production, acceleration, propagation and composition of cosmic rays. On the experimental side, a comparison between the existing data makes evident that there is a substantial disagreement between the models for the primary cosmic ray composition provided by different experiments. The ARGO-YBJ experiment permits to investigate a large energy range from a few TeV up to the knee region by exploiting both the digital and the analog read out of the RPCs.

In Fig.2.10 we show the average strip and pad sizes (N_s and N_{pad}) as a function of the primary energy for proton-induced showers. For comparison, the total shower size N_{ch} and the so-called "truncated size" N_{ch}^{tr}, i.e., the size sampled by the full ARGO-YBJ carpet, are also plotted. In the calculations only quasi-vertical ($\theta < 15°$) showers with reconstructed core inside a small fiducial area (260 m^2 around the center of the carpet) have been used. As can be seen from the figure, $log(N_s)$ is a linear function of $log(E)$ up to about 100 TeV and "saturates" above 1000 TeV. Accordingly, the digital response of the detector can be used to study the primary spectrum up to energies of a few hundreds TeV. In order to extend the dynamic range, a charge read-out has been implemented by instrumenting each RPC also with two large size pads of dimension 140×125 m^2 each [50].

The results of the calculations for the smaller ARGO-42 carpet are shown in Fig.2.11. In this case the saturation of digital response starts below 100 TeV.

The analog read-out system has been put in operation on 4 Clusters ($\sim$ 180 m^2 of the detector) in Nov. 2004, allowing a cross-check of digital and analog information. The threshold of the analog read-out is > 32 particles on at least one Cluster. Fig. 2.12 shows different typologies of events that have been recorded. In the upper left plot there is an event with a maximum

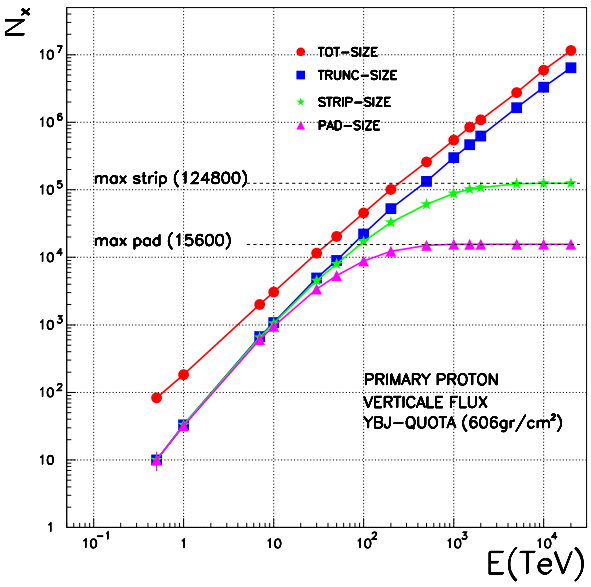

Figure 2.10: *Average strip size and pad size compared to the total size and truncated size for the full ARGO-YBJ carpet.*

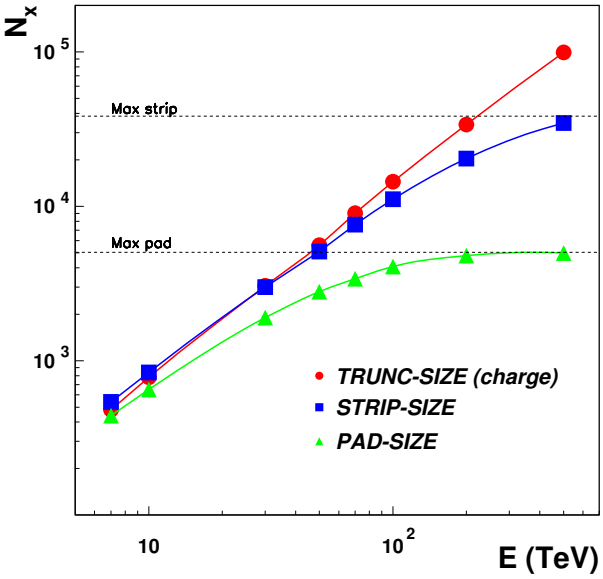

Figure 2.11: *Average strip and pad sizes compared to the total and truncated size for proton-induced air showers for ARGO-42.*

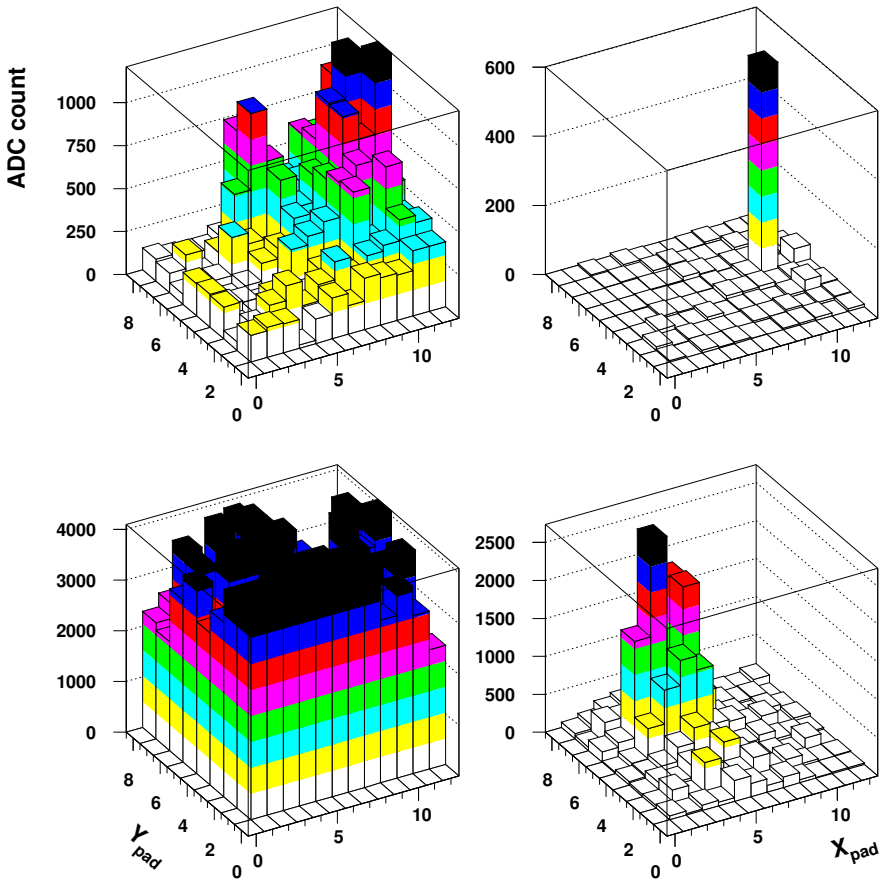

Figure 2.12: *Events on 4 Clusters at YBJ, as seen by the analog read-out system: upper left) contained event; upper right) "single pad event"; lower left) saturation event; lower right) "spot event" (See text for details).*

signal of about 50 particles/Big Pad while, in the lower left plot, a saturation event is shown where almost all 4 Clusters have Big Pads with a saturated signal corresponding to 166 particles/pad. The other two events shown refer to very localized releases of energy, in particular the one in the lower right plot involves about 15 Big Pads (about 25 m^2) with high particle density. The upper right event is very peculiar, since it has only 1 Big Pad with signal corresponding to 25 particles.

Studies are in progress to evaluate the performance of the analog read-out in the analysis of EAS hadronic cores.

Chapter 3

Study of the angular resolution of the ARGO-YBJ detector

In a search for cosmic point sources with ground-based detector the main problem is the background due to charged cosmic rays. A good angular resolution (measurement of the arrival direction) is therefore of great importance. In order to determine the primary direction the shower front has to be reconstructed from the time measurement and the position of the pads in the carpet.

This calculation is usually performed for internal events (i.e. events with the core inside the detector) only. In fact, the direction of showers with the core outside the detector is in general badly reconstructed due to the cone-like shape of the shower front and the unknown core position.

In the Fig. 3.1 is shown an exaggerated shower with two scenarios: case A where the shower core strikes at the center of the ARGO-YBJ detector, and case B where the core hits outside of the carpet. To be able to trigger the array with the same detector response (number of fired pads), the primary energy in case B is larger than that in case A. In case A, the direction obtained from the plane fitting is close to the real shower direction. However, in case B, the carpet sees a tilted portion of the same air shower, and in turn the fitted direction acquires a pointing error and deviates from the true shower direction.

If we can somehow locate the shower core position, the distance from each hit to the shower core can thus be determined. In turn, a curvature correction can be made to each pad's time to level off the tilt before the normal shower fit. In this way, the pointing error mentioned can be minimized.

The expected performance of the primary direction reconstruction procedure of the showers sampled both by the full ARGO-YBJ carpet and the smaller detector ARGO-42 is investigated in this chapter. A comparison

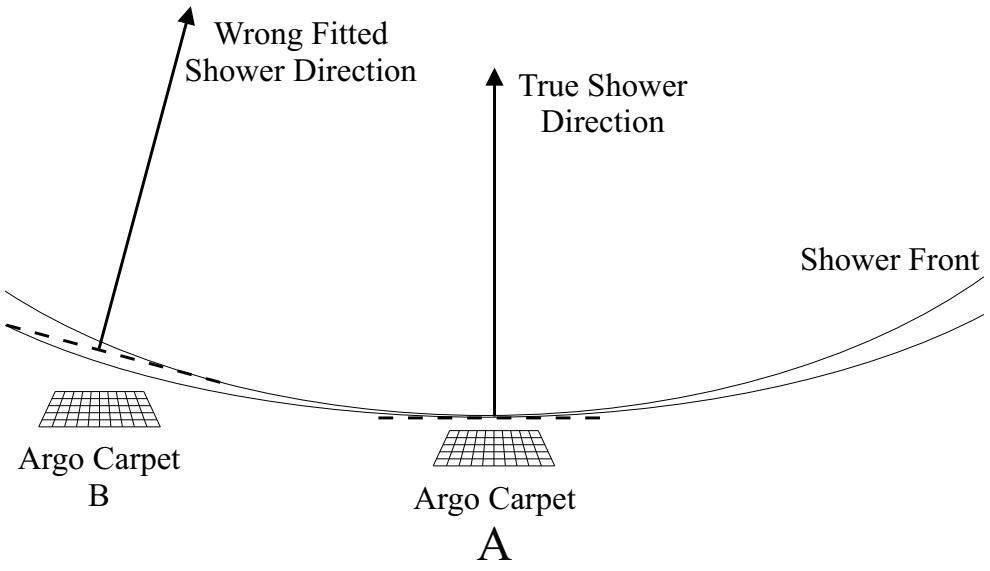

Figure 3.1: *Core inside the carpet or core outside can make a difference. The true shower core hits under the middle arrow.*

between data collected with ARGO-42 and MonteCarlo simulation is presented.

We have simulated proton and $\gamma-$induced showers via the Corsika/QGSJet v. 6.018 code [60]. The detector response has been simulated via a GEANT3-based code. The calculations has been performed for different primary energies and fiducial areas. The effect of a lead converter sheet on the full ARGO-YBJ carpet detector is also investigated. The performance of a conical correction to the shower front with a suitable fixed cone slope is discussed.

3.1 Reconstruction procedure of the shower direction

The measurements of time delays of charged particles makes it possible to estimate the direction of air showers. The arrival time of the earliest particle provides the information concerning the time profile of the shower front. From MC simulations (see ref [61], Fig. 15) it appears that the shower front assumes a parabolic shape more pronounced for the electron component than for the photon component. Near the core charged particles form, as a first approximation, a plane disk.

The thickness of an EAS is defined by the distribution of arrival times of the shower particles which are delayed relative to the prompt particles which

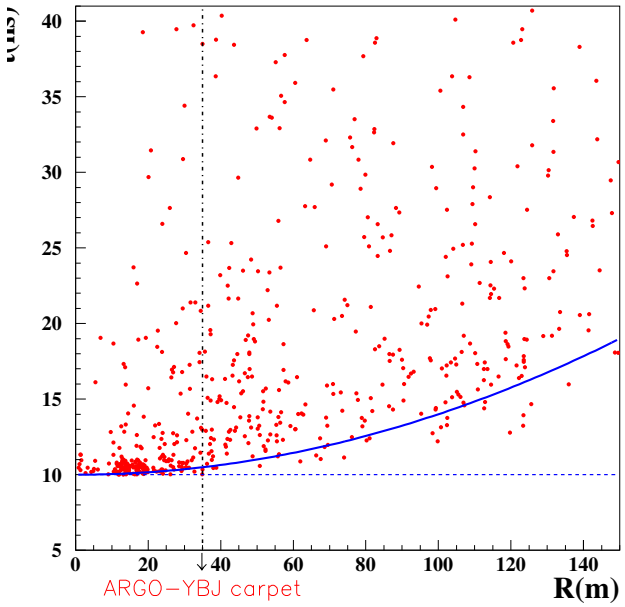

Figure 3.2: *The delay time vs the distance of the fired pads respect to the core of a typical $\gamma-$induced shower.*

make up the shower front. The shower thickness is, therefore, due to the lower-energy particles in a shower. This means that the shower thickness is smallest near the core and increases with increasing distance from the shower axis position [61]. Hence, even in the case of vertical incidence the particles arrivals are not simultaneous.

As an illustration, in Fig. 3.2 is shown the delay time versus the distance between the fired pads and the core of a typical shower. They refer to gamma-induced vertical showers with energy of 3 TeV.

In addition to the curvature, the combined effect of the finite size of the detector and of its time resolution makes the shower appear non-planar.

The usual method for reconstructing the shower direction is performing a χ^2 fit to the recorded arrival times t_i by minimization of

$$\chi^2 = \sum_i w(f - t_i)^2$$

where the sum includes all pads with a time signal. Usually the function f describes a plane, a cone with a fixed cone slope or a plane with curvature corrections as a function of r and N. Fitted are a time offset and the two direction cosines. The weights w are generally chosen to be an empirical function of the number N of particles registered in a counter, a function of r

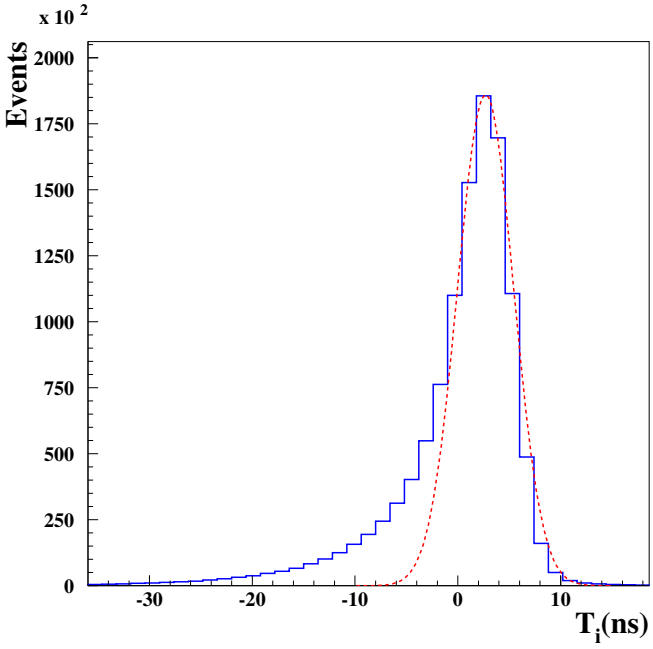

Figure 3.3: *The arrival time distribution.*

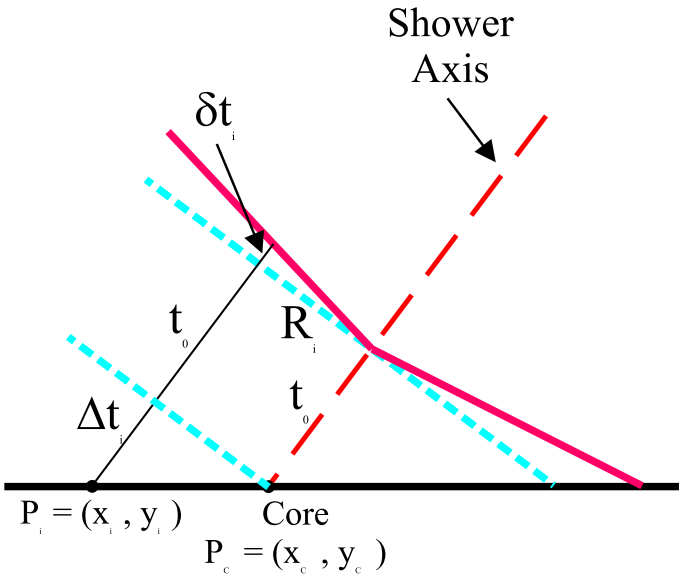

Figure 3.4: *Shower front geometry. The dashed lines are plane fit approximations to the conical time profile.*

or a function of r and N. This represents in general terms the usual fitting procedure.

Improvement to this scheme can be achieved by excluding from the analysis the time values belonging to the non-gaussian tails of the arrival time distribution (see Fig. 3.3) by performing some successive χ^2 minimizations for each shower [62].

In Fig. 3.4 is shown the shower front geometry. The dashed lines are plane fit approximations to the conical time profile. With reference to this figure we can define

- **Plane fit**

  $$T_i = [t_0+\Delta t_i]-(t_i)_{exp} = \begin{cases} 0 & \text{if the particle is on the shower plane} \\ \neq 0 & \text{due to the fluctuations} \rightarrow \text{'shower thickness'} \end{cases}$$

  Minimizing ΣT_i^2 with respect to $\{l, m, t_0\}$ correspond to impose that experimental hits are on the shower plane.

- **Conical fit**
  Conical approximation implies the additional term $\delta t_i(l, m)$

  $$\Delta t_i \rightarrow \Delta t_i + \delta t_i(l, m) \tag{3.1}$$

  where

  $$\delta t_i = \alpha \cdot R_i \tag{3.2}$$

  $$R_i = \sqrt{(\Delta x_i^2 + \Delta y_i^2) - (\Delta x_i l + \Delta y_i m)^2} \tag{3.3}$$

  and $\Delta x_i = x_i - x_c$, $\Delta y_i = y_i - y_c$, and α is the slope parameter.

  While Δt_i is a linear function of direction cosines, the conical correction δt_i is not a linear function of $\{l, m\}$. Then for the following:

  $$\chi^2 = \Sigma_i w_i (t_0 + \frac{\Delta x_i}{c} l + \frac{\Delta x_i}{c} m + \alpha R_i - t_i)^2 \tag{3.4}$$

  therefore an algebric minimization is not possible.

Usually the R_i expression is approximated to $R_i = \sqrt{(\Delta x_i^2 + \Delta y_i^2)}$, i.e. the radial distance is computed on the detector plane, not on the shower plane.

As a consequence, the conical fit can be performed using an iterative procedure

a) Plane fit
In the first step we recover the shower direction cosines $\{l_p, m_p\}$ by means of a planar fit performed minimizing the function $\chi^2(ns^2) = \frac{1}{c^2}\sum_i w\{lx_i + my_i + nz_i + c(t_0 - t_i)\}^2$. The sum includes all the fired pads and c is the velocity of light, t_i is the arrival time, $(x_i, y_i, z_i \equiv 0)$ are the coordinates of the center of the i-th pad, and the weights w_i are the number of fired strips inside the $i-th$ pad. The parameters of the fit are the time offset t_0 and the direction cosines l, m. After each minimization the time signals which deviate more than $K \cdot \sigma$ from the fitting function are excluded from further analysis and the fit is iterated until all times do not verify this condition or the reconstructed angle difference between consecutive fits is less than 0.1°. If the remaining hits number is ≤ 5 the event is discarded. Here σ_{sd} is the standard deviation of the time distribution around the fitted plane (i.e. $\sigma = \sqrt{\frac{\chi^2}{N-3}}$).

b) Conical correction
From this first determination of the arrival direction $\{l_p, m_p\}$ we calculate the conical correction $\delta t_i(l_p, m_p) = \alpha \cdot R_i$, where:

$$R_i = \sqrt{(\Delta x_i^2 + \Delta y_i^2) - (\Delta x_i l_p + \Delta y_i m_p)^2} \tag{3.5}$$

and $\Delta x_i = (x_i - x_c)$, $\Delta y_i = (y_i - y_c)$ are the pad distances from the shower core position $\{x_c, y_c\}$. Then we correct the experimental time values $t_i \rightarrow t_i' = t_i - \delta t_i(l_p, m_p)$. In this approach the slope parameter α is not a fit parameter but is fixed to a value that maximizes the angular resolution [63].

c) New plane fit
With the time values t_i' we reconstruct a new shower direction by means of a further planar fit.

A systematic study via MC simulations led us to the following best tuning of the reconstruction procedure for γ and proton-induced showers:

- **full ARGO-YBJ carpet**
  $K = 1.5 - 2$ with the maximum number of iterations in the range 5 - 6 (see ref. [64, 65]).

- **ARGO-42**
  $K = 1.5 - 2$ with the maximum number of iterations in the range 8 - 12 (see ref. [66]). In Fig. 3.5 is shown the angular resolution (see section 1.3.3) as a function of the number of iteration for several cuts for proton-induced showers. A proton spectrum with an index of -2.7 has been simulated with the CORSIKA/QGSjet code in the energy range $400\ GeV \div 1\ PeV$.

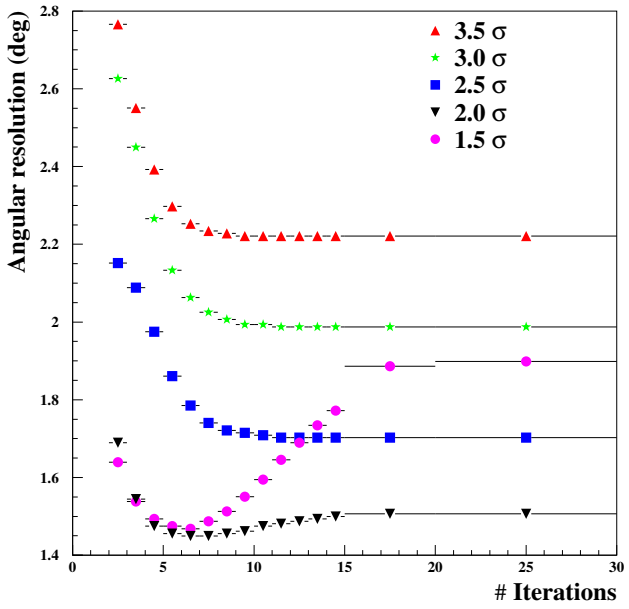

Figure 3.5: *Angular resolution as a function of the number of iteration for several cuts for proton-induced showers.*

In both case a further improvement of the angular resolution is obtained by fixing the slope of the successive conical correction to the value $\alpha = 0.03$ ns/m. The shower core position is reconstructed by means of the Maximum Likelihood Method applied on the RPCs (the so-called 'LLF2 method' of ref. [68]). The Fig. 3.6 shows the comparison between the angular resolution calculated via plane (squares) and conical (triangles) fit as a function of the pad multiplicity (N_{pad}) for photon-induced showers. Photons has been simulated with a Crab-like energy spectrum from 100 GeV to 100 TeV. The left plot refers to the full ARGO-YBJ and the right plot to the ARGO-42 carpet. No selection on the events has been performed.

3.2 The effect of a lead sheet on improving the angular resolution

The consequences of placing a thin sheet of converter above the detector are, qualitatively: (1) absorbtion of low energy electrons (and photons) which no longer contribute to the time signal; (2) multiplication process of high-energy electrons (and photons) which produce an enhancement of the signal. The enhanced signal reduces the timing fluctuations: the contributions gained

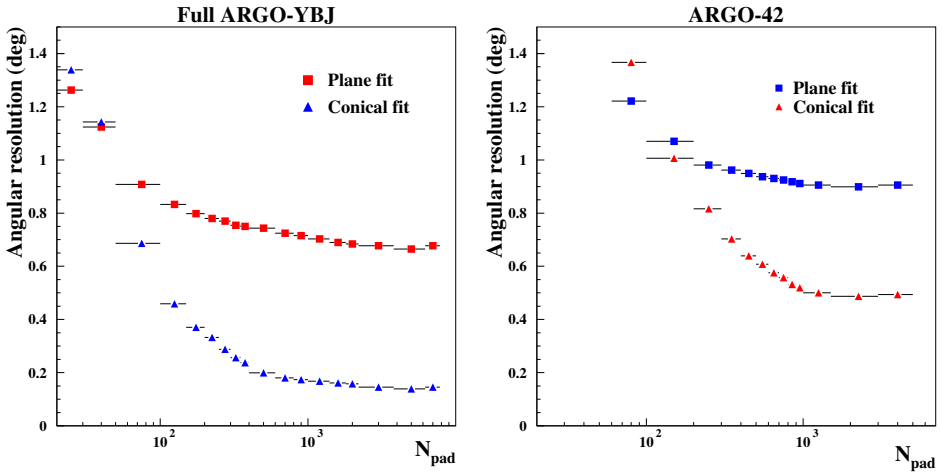

Figure 3.6: *The angular resolution is calculated via plane (squares) and conical (triangles) fit as a function of the pad multiplicity (N_{pad}) for photon-induced showers with a Crab-like energy spectrum. The left plot refers to the full ARGO-YBJ and the right plot to the ARGO-42 carpet. No selection on the events has been performed.*

are concentrated near the ideal time profile because the high energy particles travel near the front of the shower while those lost tend to lag far behind.

To study the effect of the converter on the angular resolution we have simulated the full ARGO-YBJ carpet with 0.5 *cm* lead sheet at 5 *cm* above the RPCs. The conclusions discussed in the previous section are qualitatively analogous, adding a lead converter sheet, for what concerns the dependence of the angular resolution on the number of iterations of the plane fit.

As expected, the improvement of the temporal profile of the showers implies a fewer number of iterations in the iterative procedure: the best tuning of the plane fit is achieved after only 3 iterations, with K = 1.5.

The parameter ψ_{70} is defined as the value of the angle which contains the 71.5 % of the events in the distribution of the angular difference between the reconstructed and the simulated primary shower directions (see section 1.3.3). In Fig. 3.7 we show the effect of a 0.5 cm lead sheet on the angular resolution by comparing the ψ_{70} parameter as a function of the fired pads with and without the lead. The calculations refer to 1 TeV γ-induced showers with a fixed zenithal angle $\theta = 20^\circ$ and with the core sampled on a 50 $\times$ 50 m^2 area. In the upper plot we show the values calculated after the best tuned iterative plane fit: 6 iterations without the lead and 3 iterations with the converter. In the lower part of the figure the angular resolution calculated after the conical correction is shown with and without the lead. The improvement is clearly evident.

In Fig. 3.8 the dependence of the angular resolution on the distance of

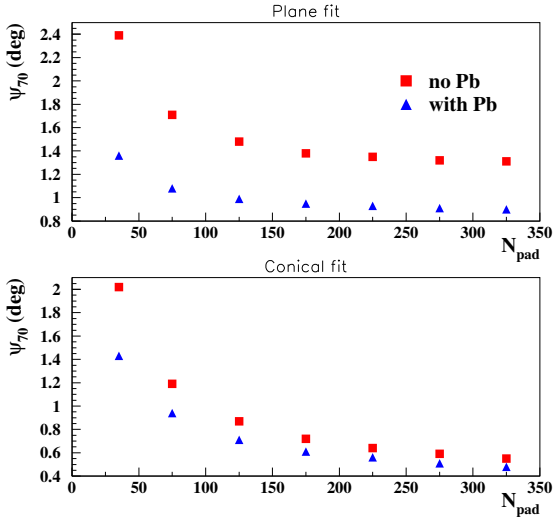

Figure 3.7: *The parameter ψ_{70} as a function of pad multiplicity after the plane fit (upper plot) and after the conical correction (lower plot) for* 1 *TeV γ-induced showers ($\theta = 20°$).*

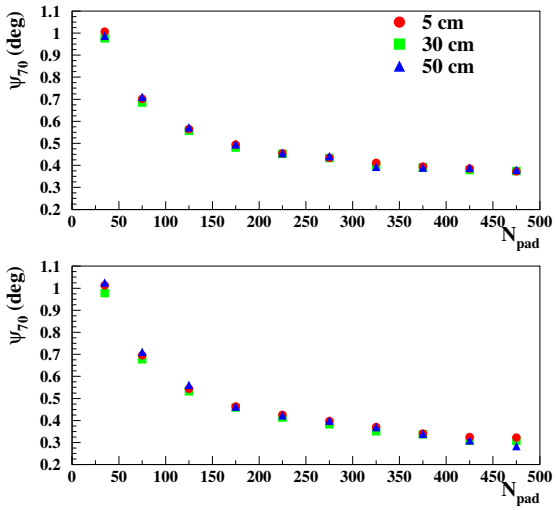

Figure 3.8: *The parameter ψ_{70} as a function of pad multiplicity after 3 plane fit (upper plot) and after the conical correction (lower plot). The data refer to 1 TeV vertical γ-induced showers sampled by a detector with* 0.5 *cm of Pb at 3 different distances from the RPCs.*

the lead sheet from the RPCs is studied. We simulated a 0.5 cm Pb sheet at three different distances from the carpet: 5, 30, 50 cm. As can be seen from the figure, the angular resolution does not dependent on the distance of the converter from the chamber plane.

3.3 Identification of showers with core outside the array

In order to obtain a good angular resolution it is crucial to select internal showers since, as already stated, the direction of the showers with core outside the detector in general is badly reconstructed due to the conical shape of the shower front and to the unknown core position. In principle all the algorithms typically reconstruct external events inside or near the detector boundaries. Therefore it's not correct reject the external events by means only of the core reconstructed position.

To find the optimal selection method we have to rely on MC calculations, thus we have simulated, via the Corsika/QGSJet code, proton-induced showers with energy spectrum $\sim E^{-2.75}$ ranging from 400 GeV to 1 PeV. The core positions have been randomly sampled in an energy-dependent area large up to 800 $\times$ 800 m^2, centered on the detector.

In a previous work [63] various parameters based on the particles density or time information has been investigated to identify showers with core position outside the ARGO-YBJ detector. The rejection of external events with the smaller ARGO-42 carpet has been exploited by studying the performance of the following quantities:

- particle fired pads density of the inner 20 clusters compared with the one of the outer ring;
- position of the cluster with the highest particle density;
- pad multiplicity of the 6 central clusters.

The selection by means of the first point permits to reject the 45% of the external events, considering as internal the events with a particle density of the inner 20 clusters greater than the particle density of the outer ring.

To locate the positions of the ARGO-42 clusters, they have been numbered from 1 to 7 on the X axis and from 1 to 6 on the Y axis, as can be seen from Fig. 3.9 where the ARGO-42 carpet is shown.

In Fig. 3.10 the distribution of the positions of the cluster with the highest particle density for proton-induced showers is shown. The events with core truly outside ARGO-42 (solid histograms) and the truly internal ones (dashed histograms) are plotted. The events selected have a pad multiplicity > 60. The clear different behaviors of IN and OUT showers suggest to tag as

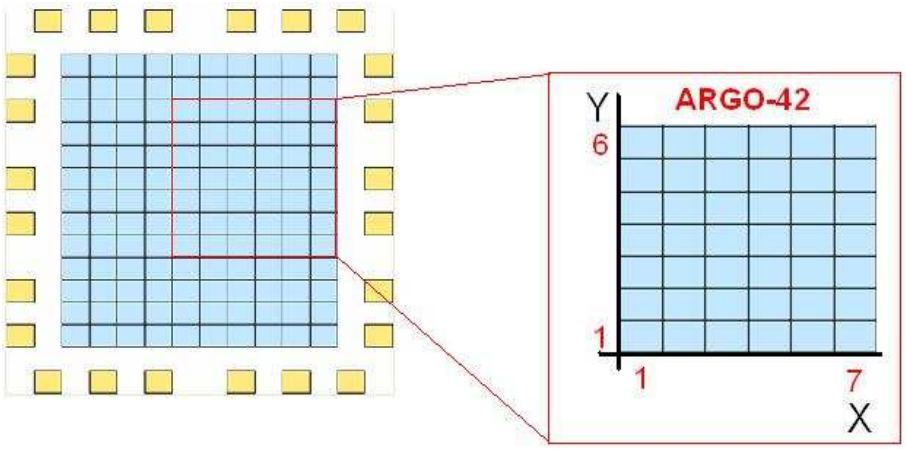

Figure 3.9: *The ARGO-42 carpet. To locate the positions of the clusters, they have been numbered from 1 to 7 on the X axis and from 1 to 6 on the Y axis.*

external the events with the highest particle density in the 2 outer clusters rows and columns.

Studying the number of fired pads on each cluster, the events with almost 16 fired pads in the 6 central clusters are a good compromise between selecting internal events and having a low energy threshold.

In conclusion in order to select a sample of events with a small contamination from external showers we define an EAS as internal if it satisfy the following selection criteria:

- the particle density of the inner 20 clusters is higher than that of the outer ring;
- the most fired cluster is one of the 6 central clusters;
- at least one of the 6 central clusters has a pad multiplicity > 16.

In Table 3.3.1 the residual fraction of external events (contamination c) and the fraction of internal showers surviving (efficiency ϵ) after the selection cuts are reported for four pad multiplicity values. The median energy (E_{50}) of the selected events is also reported. We find that for a multiplicity threshold of 60 the resulting contamination by external events is $\sim 7\%$. The median energy of such events is ≈ 4 TeV.

The shower core position $\{x_c, y_c\}$ of the selected events is hence reconstructed by means of the Maximum Likelihood Method [67]. The analysis which follows refers to showers selected as internal with the above procedure and with a zenith angle $\theta < 40°$.

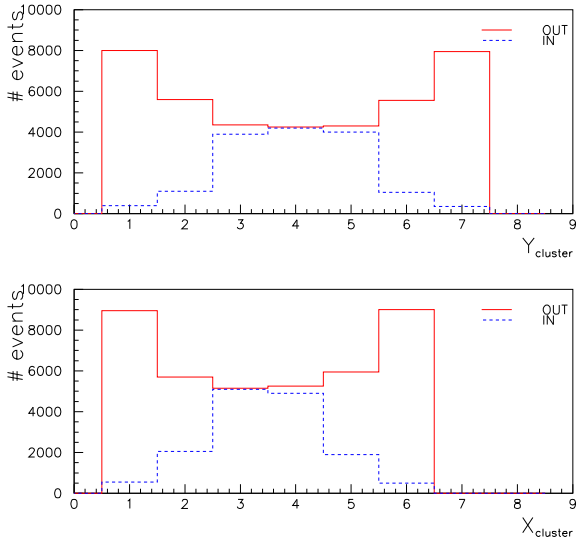

Figure 3.10: *Coordinate distributions of the cluster with the highest particle density for proton-induced showers. The plots show the X and Y view (bottom and top plots respectively). The solid histograms are for truly external events, the dashed ones are for truly internal ones. The events selected have a pad multiplicity* > 60.

3.4 The expected angular resolution of ARGO-YBJ

In this section the angular resolution has been studied via MC simulation both for the full ARGO-YBJ carpet (130 clusters) taking into account the

N_{pad}	ϵ	c	E_{50} before cuts (TeV)	E_{50} after cuts (TeV)
> 60	21%	7%	7.8	3.8
> 200	47%	6%	18.0	6.1
> 500	56%	4%	33.3	13.0
> 1000	65%	3%	50.8	24.14

Table 3.3.1: *The percentage of truly internal showers surviving (efficiency* ϵ*), the residual fraction of external events (contamination c) after the selection cuts are reported for four pad multiplicity values.* E_{med} *is the median energy before and after the selection.*

presence of 0.5 cm lead sheet on the RPCs.

In the left plot of Fig. 3.6 the angular resolution of the full ARGO-YBJ carpet is shown. As can be seen for very low multiplicity events the plane fit is better: this fact depends on the bad shower core position reconstruction. Indeed, when the procedure discussed in ref. [68] is applied and a high fraction of external showers is rejected, the conical correction improves on the plane fit. Fig. 3.11 and 3.12 show the dependence of the angular resolution on the pad multiplicity for all the events (circles) and for the internal reconstructed ones (triangles). The figures refer to proton-induced showers with an energy spectrum with a spectral index of -2.75 and photon-induced showers with a Crab-like spectrum respectively. As can be seen, for low multiplicities ($N_{pad} < 100$), the rejection of external events is crucial to improve the angular resolution.

As expected, due to the larger lateral spread of particles in proton-induced showers, the angular resolution for protons is worse than for photons.

For $N_{pad} > 100$ the angular resolution of the ARGO-YBJ experiment can be described by the equation $\sigma(^\circ) = 0.0011^\circ + \frac{4.8187^\circ}{\sqrt{N_{pad}}}$, for γ induced events with a Crab-like energy spectra. We would like to point out that one would not conclude from the above $1/\sqrt{N_{pad}}$ behavior that one can improve the angular resolution by adding more pads in the detector. A larger number of fired pads in Fig. 3.13 reflects simply the fact that one observes a larger shower which covers a larger area and has a better defined shower front with less time spread.

The resulting angular resolution is better than 0.2° for events which fire more than 600 pads on the full ARGO-YBJ carpet.

Viceversa, the angular resolution for proton-induced showers can be described by the equation $\sigma(^\circ) = 0.07^\circ + \frac{5.69^\circ}{\sqrt{N_{pad}}}$, in the same multiplicity range ($100 < N_{pad} < 1400$).

3.5 The angular resolution of the ARGO-42 carpet

In this section the angular resolution of the smaller detector ARGO-42 with only 42 clusters has been studied both via MC simulation and data.

The experimental data recorded with ARGO-42 from Dec. 2004 to Jul. 2005 has been used to investigate directly the angular accuracy of the shower reconstruction via the so-called *"chess-board method"* [69]. In Fig. 3.14 and 3.15 the angular resolution as a function of the pad multiplicity for all the events (circles) and for the internal reconstructed ones (triangles) is shown for proton and photon-induced showers respectively. Photons with a Crab-like energy spectrum and a proton spectrum with an index of -2.7 has been simulated. As can be seen, the rejection of external events is crucial to improve the angular resolution of the detector. As an example, for a pad

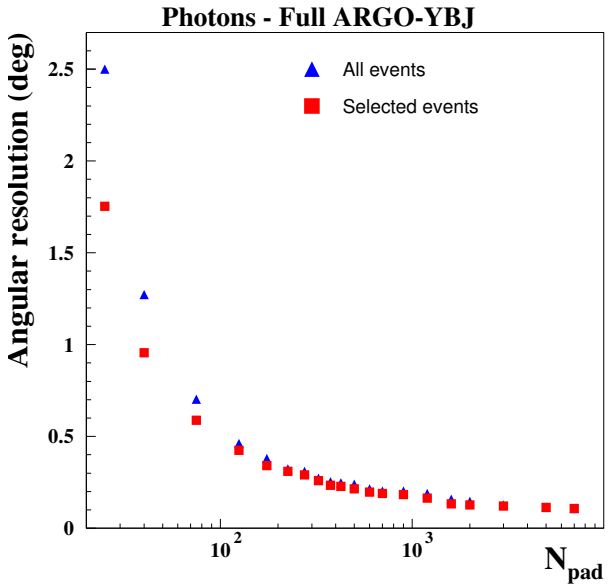

Figure 3.11: *The angular resolution as a function of pad multiplicity for γ-induced showers with a Crab-like spectrum before and after the selection of internal events.*

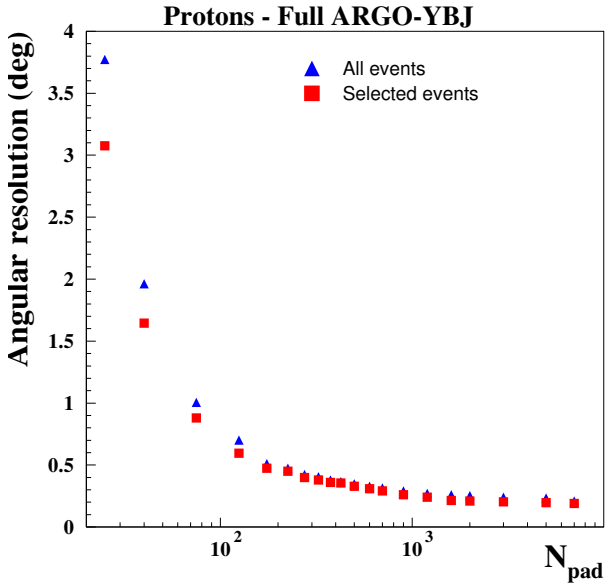

Figure 3.12: *The angular resolution as a function of pad multiplicity for proton-induced showers before and after the selection of internal events.*

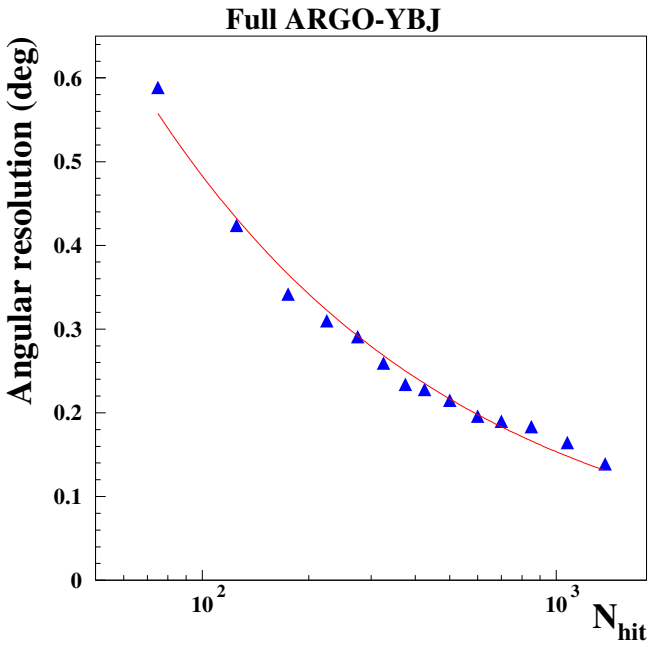

Figure 3.13: *Parametrization of the angular resolution as a function of pad multiplicity for γ-induced showers for the full ARGO-YBJ.*

multiplicity of $\sim$ 300 the angular resolution improves from 0.7° to 0.5° for both photons and protons induced showers.

The angular resolution of the ARGO-42 detector calculated by MC simulations can be described by the equations:

- **Proton-induced showers**

$$\sigma(^\circ) = 0.23^\circ + \frac{21.87^\circ}{(N_{pad})^{0.73}} \tag{3.6}$$

- **Photon-induced showers**

$$\sigma(^\circ) = 0.23^\circ + \frac{16.76^\circ}{(N_{pad})^{0.70}} \tag{3.7}$$

It is possible to use the experimental data directly to study the angular accuracy of the shower reconstruction. For this purpose the detector can be divided into two interspersed sub-arrays resembling a chess-board. The two sub-arrays, which we call the white and black array (or even-numbered and odd-numbered arrays), are handled as independent ones which view the same shower. Since they totally overlap spatially the two sub-arrays each are affected similarly by the EAS curvature. The directions are reconstructed

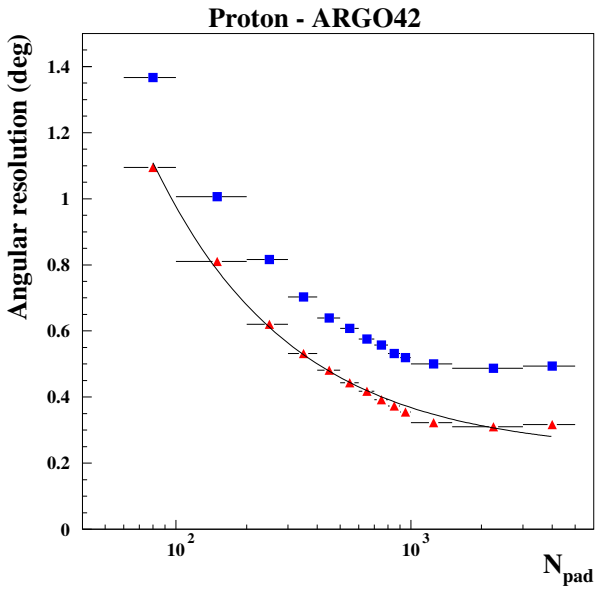

Figure 3.14: *The angular resolution before (squares) and after the selection (triangles) as a function of pad multiplicity for proton-induced showers.*

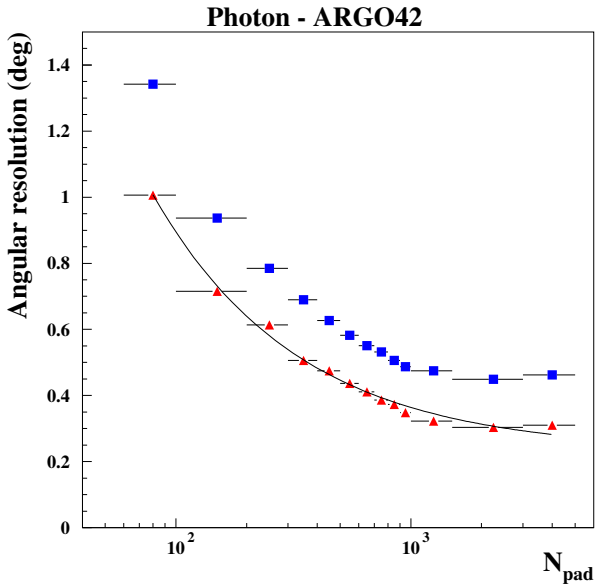

Figure 3.15: *The angular resolution before (squares) and after the selection (triangles) as a function of pad multiplicity for $\gamma-$induced showers.*

independently in both arrays and the resulting angles are compared (this is the so-called *"chess-board method"*). This method obviously works only if in each of the sub-arrays enough counters are hit by shower particles in order to allow us to perform the fit (we ask for a minimum of 5 pads as the fit has 3 degrees of freedom). Further we require that the difference in the number of counters hit in both sub-arrays is less than 4. This guarantees that both reconstructions have a similar systematical and statistical errors. In the following analysis we used the shower core parameters deduced from information from the full ARGO-42 carpet instead of using two separately fitted cores, one from each sub-array. Thus the assumption of two totally independent measurements is not completely correct.

The median of the distribution of the difference of the space angles determined from two sub-arrays, M_Δ, is a measure of the angular resolution. Assuming that the angular resolution function for the entire array is a Gaussian, its standard deviation σ is given by

$$\sigma = \frac{M_\Delta}{1.177 \times 2}. \tag{3.8}$$

The factor 2 in the above formula is the product of two separate factors of $\sqrt{2}$. One factor of $\sqrt{2}$ is due to the fact that the full array has twice as many counters as each sub-array and the angular resolution decreases as the inverse of the square root of the number of struck detectors. The other factor of $\sqrt{2}$ is present because M_Δ involves the subtraction of two independent reconstructed angles.

We evaluated the expected angular resolution of the ARGO-42 carpet applying the "chess-board method" ("even/odd method") to the simulated events reconstructed as internal with the procedure described in section 3.3.

Data recorded with the ARGO-42 carpet since Dec. 2004 to Jul. 2005 by means of an inclusive trigger ($N_{trg} = 60$, see section 2.3) have been analyzed with the same procedure used for MC simulations described in the previous sections. The relative time offset (due to differences in cable length etc.) among different pads has been estimated with the method described in [70].

In Fig. 3.16 the angular resolution obtained via the even-odd method with data from 42 Clusters (squares) is compared, as a function of pad multiplicity N_{pad} (i.e., the sum of even and odd pads), to the MC results (triangles). The upper scale shows the estimated median energy of triggered events for the different multiplicity bins. As can be seen, there is a fine agreement of the simulated result with the experimental one.

The data can be described by the following expression:

$$\sigma = 0.27 + \frac{20.06}{N_{pad}^{0.67}} \tag{3.9}$$

However, a small angle between even and odd directions does not necessarily guarantee a good angular resolution. The equations 3.9 and 3.6

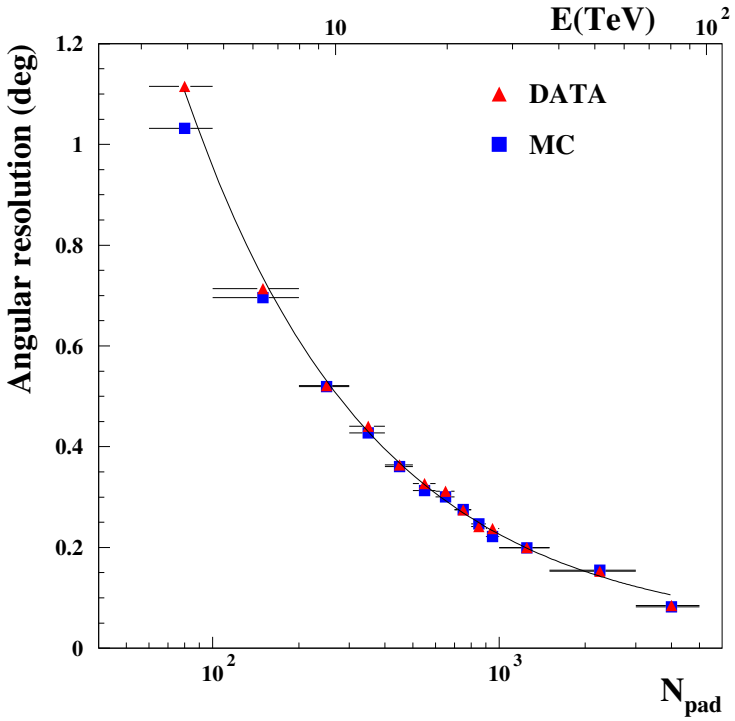

Figure 3.16: *Comparison between the angular resolution for MC simulation and ARGO-42 data as a function of the pad multiplicity. The upper scale shows the estimated median energy of triggered events for the different multiplicity bins.*

don't give the same results because the even and odd reconstruction are not indipendent.Therefore angular resolution studies with sub-arrays only give information on statistical errors.

Systematic pointing errors cannot be estimated with this approach. Both aspect, absolute pointing and angular resolution, can be studied analyzing the shadow of the Moon (see chapter 4).

3.5.1 Analysis with the zenith angle distribution

In general, most of the showers should come from the zenith and this fact can be used to check if the estimated arrival direction has any systematic error, although we cannot state anything about the magnitude of the angular resolution. In Fig.3.17 the measured zenith angle distribution of internal events is shown. The best fit is provided by an exp(-n/cosθ) law, with $n = \gamma\ x_0/\lambda = 5.426 \pm 0.008$, where γ is the index of the primary energy spectrum and x_0 the observation depth. The resulting absorption mean free

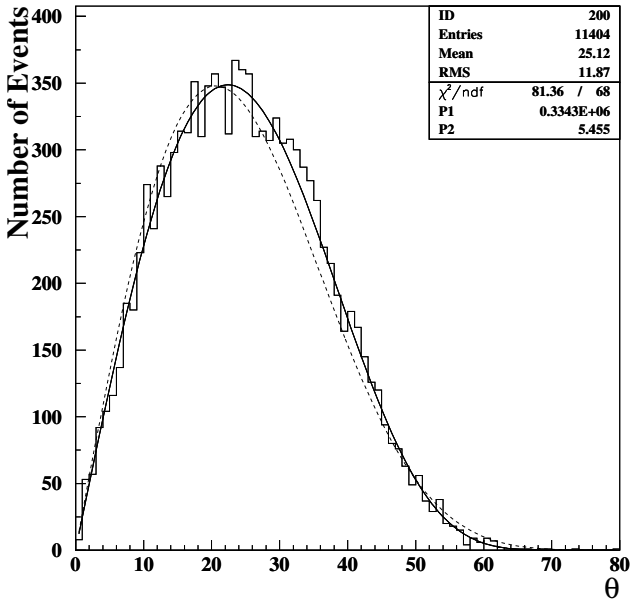

Figure 3.17: *Measured zenith angle distribution for internal events. The "exponential" (solid line) and "cos$^n\theta$" (dashed line) best fits are also shown.*

path of showers is $\lambda \approx 195$ g/cm^2, consistent with the EAS measurements [71], and the barometric effect $\beta = \gamma/\lambda = -(\Delta n/\Delta x)/n \approx 0.9\%$ mbar^{-1}. The difference in fitting the angular distribution with an exponential (solid line of Fig.3.17) or with a $\cos^n\theta$, $n = 7.05 \pm 0.02$ (dashed line) function shows that the shape is dominated by the physical effect of atmospheric absorption. Distributions dominated by instrumental effects are better fitted with $\cos^n\theta$ behaviors [72]. The fitted curve reaches the maximum at zenith angle $\theta \approx 22°$, while the average value is $< \theta >= 25.19°$. Only about 5 % of the showers have zenith angles larger than 45°. The direction distribution of recorded showers is centered around the zenith, and does not display features indicative of inaccurate timing.

The distributions of the direction cosines l and m both exhibit a Gaussian shape around the zenith suggesting that residual systematic timing shifts are negligible. Their peak positions, obtained by fitting a Gaussian curve around the zenith, are -0.002 $\pm$ 0.003 and 0.005 $\pm$ 0.003, respectively.

In addition, assuming that the distribution of the shower axis projected zenith angles follows a $\cos^n\theta$ function, it is possible to calculate the value of n which would give the observed dispersion of the projected zenith angle. It can be shown that $D(\sin\theta_\perp) = 1/(n+2)$, where $D(\sin\theta_\perp)$ is the dispersion of the sine of the projected zenith angles [73]. From the measured dispersion

($D(\sin\theta_\perp) = 0.10$) we obtain $n \sim 7.8$, in good agreement with the results of the fitting of the differential zenith angle distribution.

3.6 Conclusions

The study of the angular resolution of the ARGO-YBJ detector carried out with MC simulations and ARGO-42 data analysis leads us to the following conclusions:

- The angular resolution of the full ARGO-YBJ carpet can be described, for $N_{pad} > 100$, by the equation $\sigma(^\circ) = 0.0011^\circ + 4.8187^\circ/\sqrt{N_{pad}}$, for γ-induced events with a Crab-like energy spectra. The angular resolution for proton-induced showers can be described by the equation $0.07^\circ + \frac{5.69^\circ}{\sqrt{N_{pad}}}$, in the same multiplicity range ($100 < N_{pad} < 1400$).

- The angular resolution of the smaller ARGO-42 detector can be described by the relation $\sigma(^\circ) = 0.23^\circ + \frac{21.87^\circ}{(N_{pad})^{0.73}}$ for proton-induced showers and $\sigma(^\circ) = 0.23^\circ + \frac{16.76^\circ}{(N_{pad})^{0.70}}$ for photon-induced showers, without any lead sheet.

- The angular resolution of the ARGO-42 carpet without any lead sheet obtained with data recorded from Dec. 2004 to July 2005 by means of the "chess-board method", can be described by the formula $\sigma(^\circ) = 0.27^\circ + \frac{20.06^\circ}{(N_{pad})^{0.67}}$ for cosmic ray events. The equations 3.9 and 3.6 don't give the same results because the reconstruction coming from the two sub-arrays are not independent.

- We found a fine agreement between data collected with ARGO-42 and MC calculations, as well as a good consistency of all the investigated parameters with results of other EAS experiments.

We may conclude that the detector is working according to the expected performance and our reconstruction procedure are correct.

In the next chapter a study of the angular resolution looking at the shadow of the Moon is presented.

Chapter 4

The shadow of the Moon

This chapter is devoted to the study of the angular resolution of the ARGO-42 detector by means of the analysis of the shadow of the Moon. ARGO-42, about one third of the final active area ($\sim$ 1800 m^2), was in data taking from December 2004 to July 2005. It has stably operated for debugging and calibration. The data collected were a useful tools to check the detector performance and the reconstruction algorithms. Despite the small detection area and the short duration of the data taking a first analysis of the Moon shadow has been performed.

4.1 Moon-shadow simulation

A proton spectrum with an index of -2.7 has been simulated with the CORSIKA/QGSjet code in the energy range 400 $GeV \div 1$ PeV. The primary direction is reconstructed with the procedure described in the previous chapter. A fake Moon shadow is generated by throwing events from the Moon's direction and then subtracting them from a simulated background. The effect of geomagnetic field is simulated as described in the section 4.1.3 as a function of the rigidity of the particle.

It should also be mentioned that the Moon is not a source at all, but a "sink". Unlike all other analysis which look for excesses of events above the background of cosmic rays, the shadow study looks for a deficit of events below the background.

4.1.1 An estimation of the expected "signal"

The number of background events in a circular bin of 1° of radius is:

$$N_{bkg}(1^\circ) = \Phi_p(> E) \cdot A_{fid} \cdot T_M \cdot (d.c.) \cdot \Delta\Omega(1^\circ) \qquad (4.1)$$

where:

Expected Moon observation time	hours ($\theta < 50°$)
Dec 04	156
Jan 05	149
Feb 05	130
Mar 05	122
Apr 05	127
May 05	135
Jun 05	144
Jul 05	153
Tot.	1116

Table 4.1.1: *Moon observation time with a zenith angle* $\theta < 50°$.

- $\Phi_p(> E)$ is the proton flux with energy $> E$

$$\Phi_p(> E) = 5.16 \cdot 10^{-2} (\frac{E}{TeV})^{-1.74} \; protons/m^2 \cdot s \cdot sr \qquad (4.2)$$

- A_{fid} is the fiducial area
- T_M is the Moon observation time
- $(d.c.)$ is the duty cycle
- $\Delta\Omega(1°)$ is the area of the angular bin

$$\Delta\Omega(1°) = \pi(\frac{1\pi}{180})^2 = 9.57 \cdot 10^{-4} \; sr \qquad (4.3)$$

In our case we can consider as the fiducial area the dimension of ARGO-42 ($A_{fid} = 2000 \; m^2$) and a value of the duty cycle $\sim 50\%$, reasonable for an apparatus like ARGO-42 in the debugging phase.

The expected Moon observation time with a zenith angle $\theta < 50°$ at YBJ from Dec. 2004 to Jul. 2005 has been calculated (see Table 4.1.1). As the detector cannot be triggered above a certain zenith angle value, the Moon is only available for certain periods of time. For these analysis the maximum zenith angle considered is 50°. Since the period of ARGO-42 data tacking goes from 24-12-04 to 23-03-05 and from 19-05-05 to 17-07-05, then the estimated observation time is $\sim 830 \; h = 2988 \; 10^3 \; s$.

The inclusive trigger used for the ARGO-42 data permits to select showers with a median energy of about 4 TeV.

Therefore, taking into account the proton flux above 4 TeV, from the 4.2.1 it results:

$$N_{bkg}(1°) = 4.625 \; 10^{-3} \cdot 2000 \cdot 2988 \; 10^3 \cdot 0.5 \cdot 9.57 \; 10^{-4} = 13224 \; protons \qquad (4.4)$$

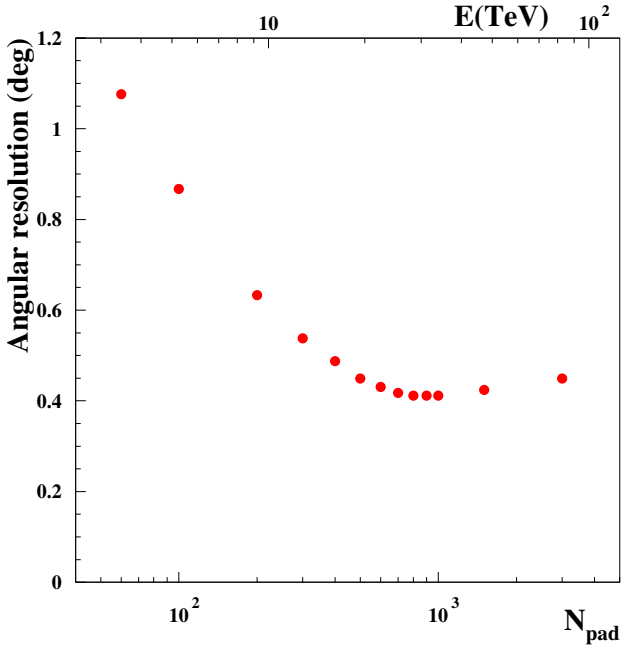

Figure 4.1: *Angular resolution for events with a pad multiplicity* $> N_{pad}$. *No selection on external events has been applied. The upper scale shows the estimated median energy of triggered events for the different multiplicity bins.*

Indeed in a circular bin of 1° of radius we estimate a background signal $N_{bkg} = 13224$ protons.

In the same way we can calculate the number of protons in a circular bin of 0.26° of radius equal to the Moon dimension. Then the number of protons absorbed by the Moon is about 894. This corresponds to a 7.8 σ effect.

Therefore the expected signal from the Moon direction is 12330 protons. At an energy threshold of 20 TeV the expected signal is 750 protons.

4.1.2 Angular resolution estimation

Since the number of collected events is too small, we have calculated the expected angular resolution for this sample of data without applying any selection to reject external events. Fig. 4.1 shows the angular resolution for events with a pad multiplicity $> N_{pad}$. It results that for events detected with an inclusive trigger $N_{pad} > 60$ the angular resolution is about 1.1°. Increasing the threshold the angular resolution improves. For $N_{pad} > 500$ the angular resolution is 0.4°.

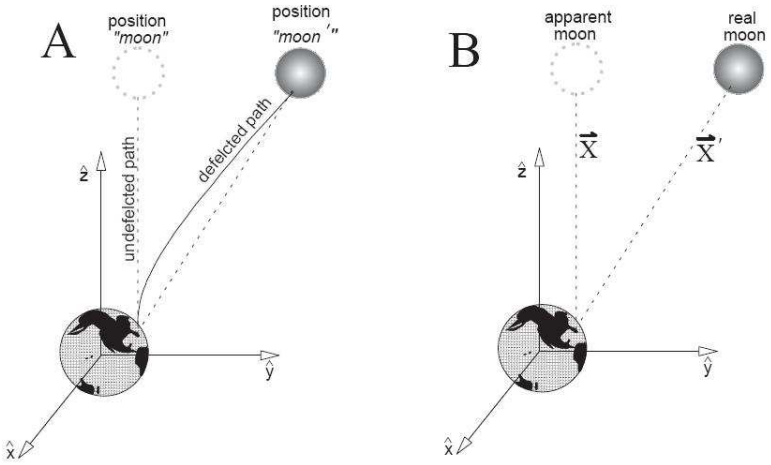

Figure 4.2: *Diagram illustrating the cosmic ray tracking method. Cosmic rays are projected from the top of the atmosphere above ARGO-YBJ toward the position "Moon", and traced as they are deflected by geomagnetic field. The deflected path leads to the position "Moon′", which is the true position of the Moon.*

4.1.3 Cosmic ray tracking

The cosmic ray tracking method is illustrated in Fig. 4.2. The geomagnetic deflection of cosmic rays is simulated by starting with a cosmic ray of known charge Ze and mass m located at the ARGO-YBJ position and projecting that cosmic ray towards the position of the Moon, designed as "Moon" in Fig. 4.2. This is the direction opposite to the direction actually traversed by real cosmic rays coming from the Moon to the Earth. The geomagnetic field bends the path of the particle, so that it does not finish its motion at the position "Moon", but rather at some new position, "*Moon′*". The path traced by the cosmic ray in this way is the same it would trace starting at "*Moon′*" and moving toward the Earth rather then away from it.

Two vectors can now be defined: one, $\vec{X}$, from the detector to the position "Moon", and a second, $\vec{X}'$, from the detector to the position "*Moon′*". The interpretation of these vectors in the context of the Moon shadow simulation is tricky, but crucial. The vector $\vec{X}'$ is the line of sight from the detector to the true position of the Moon, and $\vec{X}$ is the line of sight from the detector to the apparent position of the Moon. In other words, $\vec{X}$ desig-

nates the path that photons would travel as they passed from the apparent Moon position to the earth. But since cosmic rays are charged particles moving through a magnetic field, they follow a curved path between the Moon and the earth. The cosmic ray paths are bent by the geomagnetic field, so that the momentum vector of a cosmic ray that travelled from the true Moon position ($\vec{X}'$ in Fig. 4.2) to the earth is aligned with the vector $\vec{X}$ when it arrives at the detector carpet. Thus projecting the direction of the final momentum vector of that cosmic ray back away from the earth makes it appear as if the cosmic ray originated at the position "Moon". A look-up table of detection values was assembled by projecting cosmic rays in the above manner for all positions of the Moon in steps of 1°, and for several values of magnetic rigidity, from 100 GV/c up to 500 GV/c. Above 500 GV/c, the detection of cosmic rays by the geomagnetic field was found to change inversely with the rigidity, so the detection of cosmic rays above this rigidity is found by extrapolating the detection of a 5500 GV/c cosmic ray up to the higher rigidity. The coordinate system used for the simulation is Cartesian, with the origin placed at the center of the earth. The z-axis intersects the geographic north pole, and the x-axis intersects prime meridian at the equator. The center of the earth is chosen as the origin, rather than ARGO-YBJ, because the distance from the Moon to the center of the earth is very nearly constant, while the Moon-ARGO-YBJ distance is not. The geomagnetic field used is a simple dipole field, with the point dipole itself pointed in the direction of the magnetic pole closest to the south geographic pole. The dipole field, $\vec{B}(\vec{x})$, at any point was calculated using a formula from [77]:

$$\vec{B}(\vec{x}) = \frac{3\vec{n}(\vec{n}\cdot\vec{m}) - \vec{m}}{|\vec{x}|^3} \tag{4.5}$$

where $\vec{m}$ is the dipole moment and $\vec{n}$ is a unit vector in the direction of $\vec{x}$.

The bending is done in small steps, over which the magnetic field is assumed to be constant. In traversing a constant magnetic field, a charged particle follows a circular path whose radius, r, is determined by the rigidity, R, of the particle and the strength of the magnetic field, B,

$$r = \frac{R}{0.3B} \tag{4.6}$$

where r is measured in m, B in $Tesla$, and R in GV/c [78]. So, in each step the magnetic field is calculated and the particle, located at $\vec{x}$ with momentum $\vec{p}$, is sent through its circular path. At the end of the step, the new position and momentum, $\vec{x}'$ and $\vec{p}'$, of the particle are calculated and used at the beginning of the next step. The steps are parameterized as a function of time; the new position and momentum of each step are found by calculating the motion of the particle at the old position with the old momentum and for a set period of time, Δt. The step size was determined

by varying Δt for a test particle's trajectory until it was small enough that there was no noticeable change in the outcome by reducing it any further.

4.1.4 Understanding the "source"

Starting with the Moon's position for a given day and time, the geomagnetic deflection is first applied. The resulting deflected direction is taken as the incident direction of the cosmic ray. Then the shower induced by this cosmic ray and the detector response are simulated, and the reconstructed direction (θ, ϕ) obtained.

To define the cosmic ray direction in the sky, both local (θ, ϕ) and equatorial coordinate (α, δ) systems are used (see Fig. 4.3 and 4.4). The Moon position is computed using a program based on the ephemerides of the 1950. The error on the position calculation is estimated to be smaller than 0.01°, much smaller than the angular resolution or the Moon radius. The Moon is the nearest and the only astronomical object for which the position is significantly dependent on the observation location on Earth. This parallax effect is taken into account. It amounts to a few tenths of a degree.

A distant object, such as a star or a galaxy, is always located at the same point in the sky, at least over a time scale of human lifetimes. The Moon oscillates through α and δ with a period of 28 days. In a lunar month its declination change between $\pm 28^\circ$ and at YangBaJing location the Moon follows a trajectory with the culmination zenith angle that changes between 2° and 58°.

Fig. 4.5 shows the simulated angular distribution in a 1° angular bin around the Moon's position. Only those events which would have come from the Moon's position, but are not blocked by its presence are plotted. The peak oh the zenith angle is $\sim 22^\circ$. No events were simulated at $\theta > 50^\circ$, that's why the azimuthal angle ϕ distribution shows an absence of events between $0^\circ \div 140^\circ$.

To simulate the data trigger rate and to take into account the period when the apparatus was off, to each simulated event is associated the time of a real event. The simulated θ and δ versus the time are plotted in Fig. 4.6. The plots contains blank spaces because we have taken into account when the experiment was down.

In conclusion, events in a 1° angular bin around the Moon recorded with ARGO-42 are expected to follow the angular distributions of Fig. 4.5 and 4.6.

Once we have the direction of the cosmic rays, we assemble the events into sky maps centered on the Moon's position in equatorial coordinates. In the next sections the procedure to build up the maps and the method to estimate the background will be described. These has been applied to both MonteCarlo simulation and data.

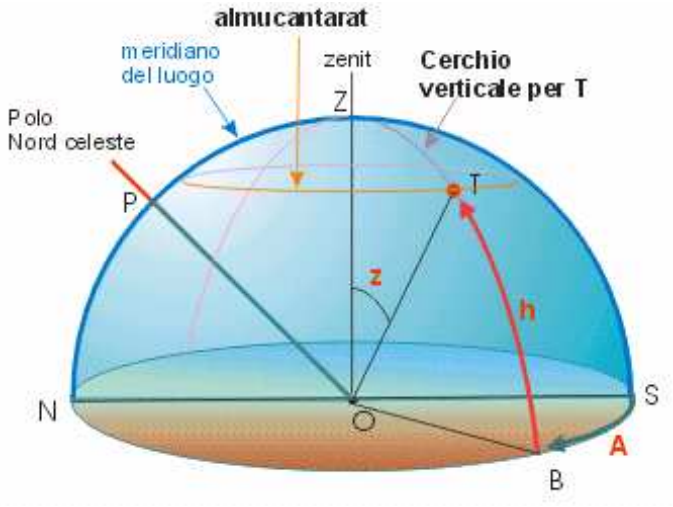

Figure 4.3: *Local coordinate system (θ, ϕ).*

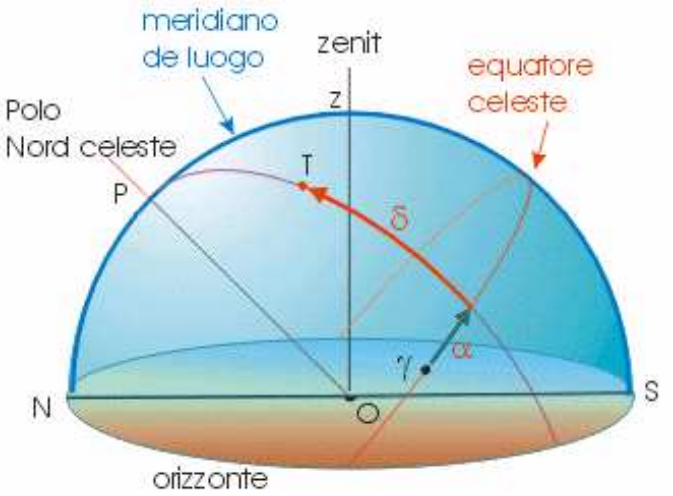

Figure 4.4: *Equatorial coordinate system (α, δ).*

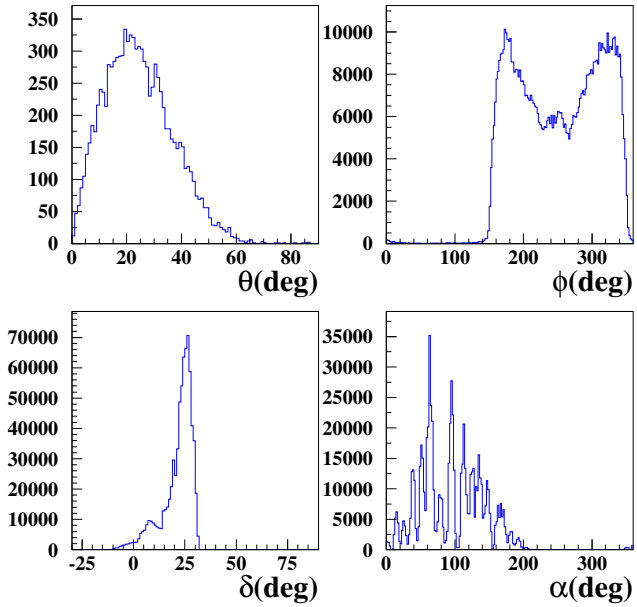

Figure 4.5: *Simulated ARGO-42 angular distribution of events from within* 1° *of the Moon. The top two plots show the events in zenith angle (θ) and azimuthal angle (ϕ) and the bottom plots show declination (δ) and right ascension (α).*

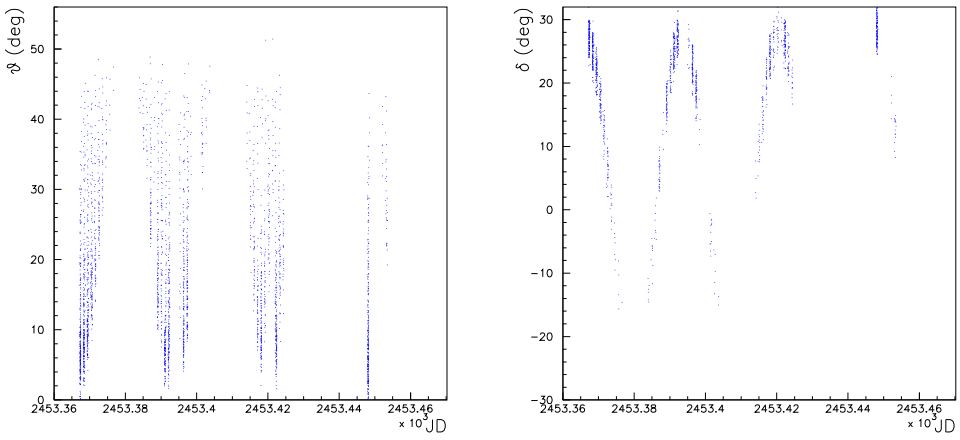

Figure 4.6: *ARGO-42 simulated zenith angle (θ) (left plot) and declination (δ) (right plot) of events from within* 1° *of the Moon as function of Julian date (JD).*

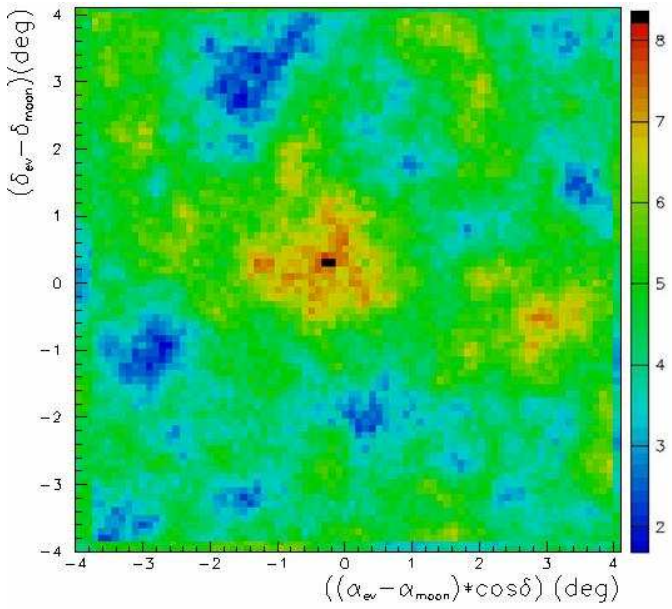

Figure 4.7: *Expected significance of ARGO-42 Moon shadow for showers with* $\theta < 50°$. *The scale given on the right indicates the significance in each* $0.1° \times 0.1°$ *bin.*

Here we report the final simulated map, obtained putting in each bin the statistical significance $\sigma = \frac{N_{ev}-N_{bkg}}{\sqrt{N_{bkg}}}$, it is shown in the Fig. 4.7. As can be seen in about 5 months of data taking the expected sensitivity is about 8.4 σ and the bin with the highest statistical significance is found at 0.2° toward West and at 0.1° toward North. A deviation from the true position is due to the magnetic field that for $N_{pad} > 60$ ($E^{50} = 4\ TeV$) gives a shift ≤ 0.4.

4.2 Signal analysis: method and procedure

In this section we describe the method used to build up the signal and background maps.

Once the arrival direction is reconstructed, the events are assembled into sky maps. The maps are centered on the Moon's position in equatorial coordinates. The map consist of square bins of 0.1° on a side. In order to map equal areas of the sky into bins no matter what the Moon's position was, the coordinates used for the maps are $\Delta\delta = (\delta_{event} - \delta_{Moon})$ on the ordinate and $\Delta\alpha = ((\alpha_{event} - \alpha_{Moon}) \times cos\delta_{event})$ on the abscissa. Once the background estimate is made (see Section 4.2.1), background maps are assembled in exactly the same way as the events maps.

The two maps could then be compared and search techniques applied to

look for a deficit in the data maps compared to the background maps.

4.2.1 Background determination

Searching for a point source (or shadow) entails the counting of the number of events in an angular bin containing the possible signal (signal bin) and comparing it to the number of background events expected in this bin.

The background estimation method used in this analysis depends on the fact that the flux of cosmic rays is isotropic in right ascension. This leads to the assumption that any real detected event in local coordinates could have come at any detected time. All of the events detected in a short time interval (typically 2-3 hours) are used to generate a fake data set as follows. The measured local coordinates (θ, ϕ) of each real event are paired with a time chosen randomly from the time interval. This new (t, θ, ϕ) triplet consists a new, fake, background event. It is as if the fake event came from the same point in the sky as the real event but at a different time. To reduce statistical fluctuations, 10 fake events are generated thus for each real event.

The effect of this method, the so-called "time swapping" method, is to mix up the times of the events in the data sample. It is equivalent of randomly reassigning a new right ascension to each event, but keeping the declination of the event unchanged. This is because the selection of a new time is equivalent to a rotation of the celestial sphere with the respect to the Earth. Transforming the original right ascension through the arc equivalent to the time difference of the two events is the same as selecting a new right ascension for the event.

This methods naturally takes into account any systematic biases in estimating the background, except for the time-dependent biases. Any interruption in the data collection or other event rate variations, are compensed for because the fake data set has the same time distribution as the real one. A weight is given to each fake event depending on the rate of the run. The fake data set also has the same distribution in local coordinates as the real data have.

4.3 Data analysis

Since December 2004 to July 2005 ARGO-42 has been put in stable data taking. In table 4.3.2 the used trigger, the number of detected events and the duty cycle (d.c.) are summarized.

During this about 5 months of data taking the expected observation time estimated for the Moon is about $\sim 830\ h$. The actual observation time has been $\sim 338.3\ h$. Indeed due to the debugging needs the data acquisition has been frequently stopped resulting in a duty cycle of only 53%.

Fig. 4.8 shows the angular distribution in θ, ϕ, δ, α from within 1° of the Moon's position.

Trigger	> 60 fired pad
Number of events	11.710^8
Run time	1909.4 h
Events rate	171 $events/s$
Duty cycle	53%

Table 4.3.2: *ARGO-42 data from 24-12-04 to 23-03-05 and from 19-05-05 to 17-07-05.*

Moon observation time ($\theta < 50°$)
estimated $\sim$ 830 h
measured $\sim$ 338.3 h
Sun observation time ($\theta < 50°$)
measured $\sim$ 304.9 h

Table 4.3.3: *Moon and Sun observation time.*

Fig. 4.9 shows the zenith angle θ and the declination δ of the Moon as a function of time. The oscillation of the Moon's path can be clearly seen. The plots contains blank spaces when the experiment was down. There is a good agreement with the angular distributions obtained with the MonteCarlo simulation (see Fig. 4.5 and Fig. 4.6).

Figures 4.10 and 4.11 show the angular distribution of events both in local coordinates and in equatorial coordinates.

Once the data are reconstructed, they are assembled into sky maps with square bin of 0.1° on a side in equatorial coordinate. These data have been used to estimate the background following the procedures described in section 4.2.1. The Fig. 4.12 shows the signal (top) and background (bottom) maps.

4.3.1 Smoothed map

The 2-dimensional sky maps may be analyzed directly. Smoothing the maps is one way to do this. The ARGO-42 Moon shadow maps have been smoothed using a circular bin of about 1°. This has the effect of drawing out features in the map that occur on scales of 1°, such as the Moon deficit. The value of 1° is a typical choice for this kind of analysis and it's compatible with the angular resolution.

From the square bins of 0.1° map a second map is constructed. A circular window of 1° of radius is made summing the square bins. This window is then moved at a step of 0.1° in both direction $East - West$ and $North - South$. As a result, these circular bins are not independent one from another. The

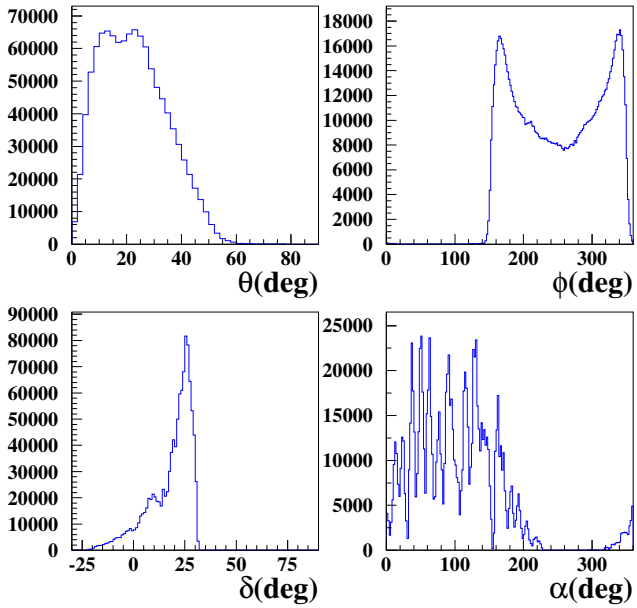

Figure 4.8: *Angular distribution of events from within* 1° *of the Moon. The top two plots show the events in zenith angle (θ) and azimuthal angle (ϕ) and the bottom plots show declination (δ) and right ascension (α).*

event maps and background maps are smoothed in the same way. Starting from these maps a final map is obtained putting in each bin the statistical significance $\sigma = \frac{N_{ev} - N_{bkg}}{\sqrt{N_{bkg}}}$.

The Fig. 4.13 shows the resulting smoothed map of the significance. The coordinates used for the maps are $\Delta\delta = (\delta_{event} - \delta_{Moon})$ on the ordinate and $\Delta\alpha = ((\alpha_{event} - \alpha_{Moon}) \times cos\delta_{event})$ on the abscissa. The scale given on the right indicates the significance in each $0.1° \times 0.1°$ bin.

From the figure it results:

- the statistical significance of the dip due to the shadow of the Moon is $\sim 5.1\sigma$. This value is a bit lower than the one expected according to the simulations. Anyway, it is the first time that the shadow of the Moon is observed with this sensitivity in such a short time;
- the maximum of the significance is located at 0.6° toward West and 0.4° toward South.

The easiest way to look for a deficit is to make projections of the maps. The map projections are shown in Fig. 4.14 and 4.15. The results has been fitted with a gaussian function. The gaussian gives a measure of the

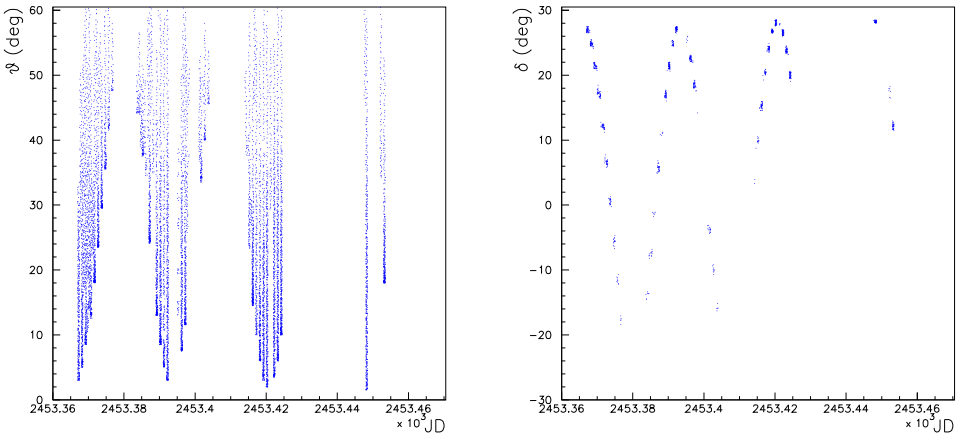

Figure 4.9: *ARGO-42 zenith angle θ (left plot) and declination δ (right plot) of events from within* 1° *of the Moon as a function of the Julian date (JD).*

width of the deficit and the position of the peak. The expected shift due to the deflection of the magnetic field is about $\sim 0.4^\circ$ (see formula 1.4 with $E \sim 4\ TeV$) toward East. From the fit of the East-West projection on the data (Fig. 4.14) the position of the minimum is at $0.77^\circ \pm 0.05$ toward East and the σ of the distribution is $0.9^\circ \pm 0.2^\circ$. From the fit on the North-South projection on the data (Fig. 4.15) the position of the peak is at $0.21^\circ \pm 0.05$ toward South and the σ of the distribution is $1.0^\circ \pm 0.2^\circ$. Therefore the shift is at variance with the expectation.

Combining both the projections the resulting angular resolution is $\sigma_\theta = 1.3 \pm 0.3^\circ$ compatible with the MonteCarlo simulation $\sigma_\theta^{MC} = 1^\circ$ (see section 4.1.1).

The observed deficit has been calculated integrating the two gaussian curves. Integrating between $\pm 1^\circ$ from the mean value the number of events is 12840 compatible with the expected value of 12330 (see section 4.1.1).

A smoothed map window of 1° has been used in this analysis. The Fig. 4.16 shows the significance versus the dimension of the radius of the circle bin used for smoothing the map (OA). As can be seen the maximum of the sigma is reached for a radius of 1°, very close to the angular resolution.

The plot 4.17 shows the distribution of the statistical significance for circular bin of 1°. The deviation from a gaussian distribution identify many dips. The one with the biggest significance (5.1σ) corresponds to the Moon shadow.

Since the deficit is found shifted respect to the nominal position of the Moon the question if it really represents the Moon shadow arises. A confirmation is given by the plots of the Fig. 4.18 where the calculated rate of obscured events and the measured rate of the observed deficit as a function

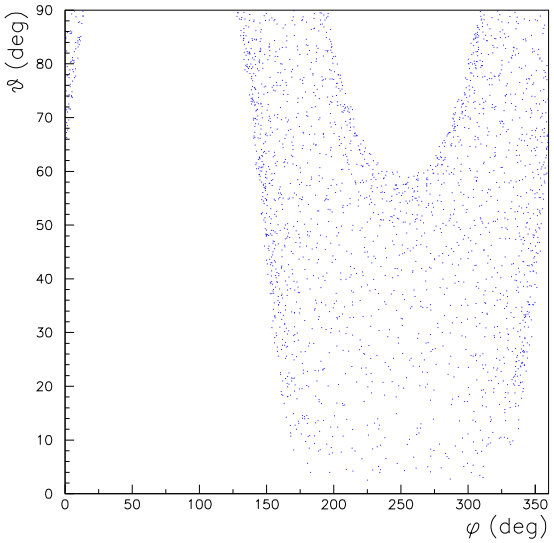

Figure 4.10: *Angular distribution of events from within* 1° *of the Moon, shown in* θ *versus* ϕ *plot.*

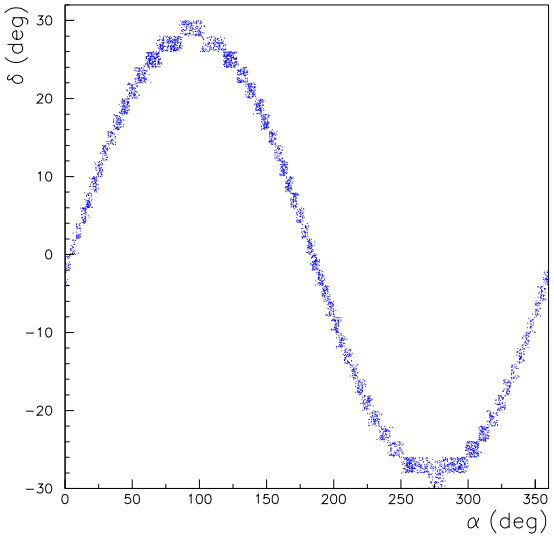

Figure 4.11: *Angular distribution of events from within* 1° *of the Moon, shown in* δ *versus* α *plot.*

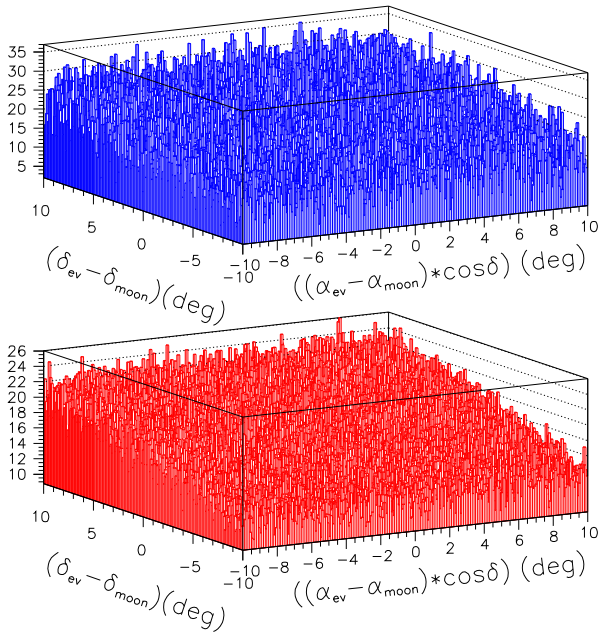

Figure 4.12: *Signal (top) and background (bottom) maps.*

of the time are compared. The agreement is excellent, confirming that the observed deficit is due to the absorption of cosmic rays by the Moon.

To investigate the disagreement between the expected and the observed position of the Moon shadow we have calculated two new maps, one selecting events with zenith angle $\theta < 40°$ and one selecting events of high multiplicity ($N_{pad} > 500$).

In Fig. 4.19 the map with $\theta < 40°$ is shown. Also in this case the map shows a shift toward West so it seems that the disagreement doesn't depend on the bad direction reconstruction due to very tilted showers.

The Fig. 4.20 shows the smoothed map of the significance for showers with $N_{pad} > 500$. In this case the statistical significance is 3.9σ and the shadow moves toward the expected position.

The projections of the map obtained selecting events with $N_{pad} > 500$ are shown in Fig. 4.21 and 4.22. In this case the results of the fit are:

- East-west projection: the position of the minimum is shifted of $0.038° \pm 0.004$ toward East and the σ is $0.6° \pm 0.2°$.

- North-South projection: the position of the minimum is shifted of $0.38° \pm 0.05$ toward South and the σ is $0.6° \pm 0.2°$.

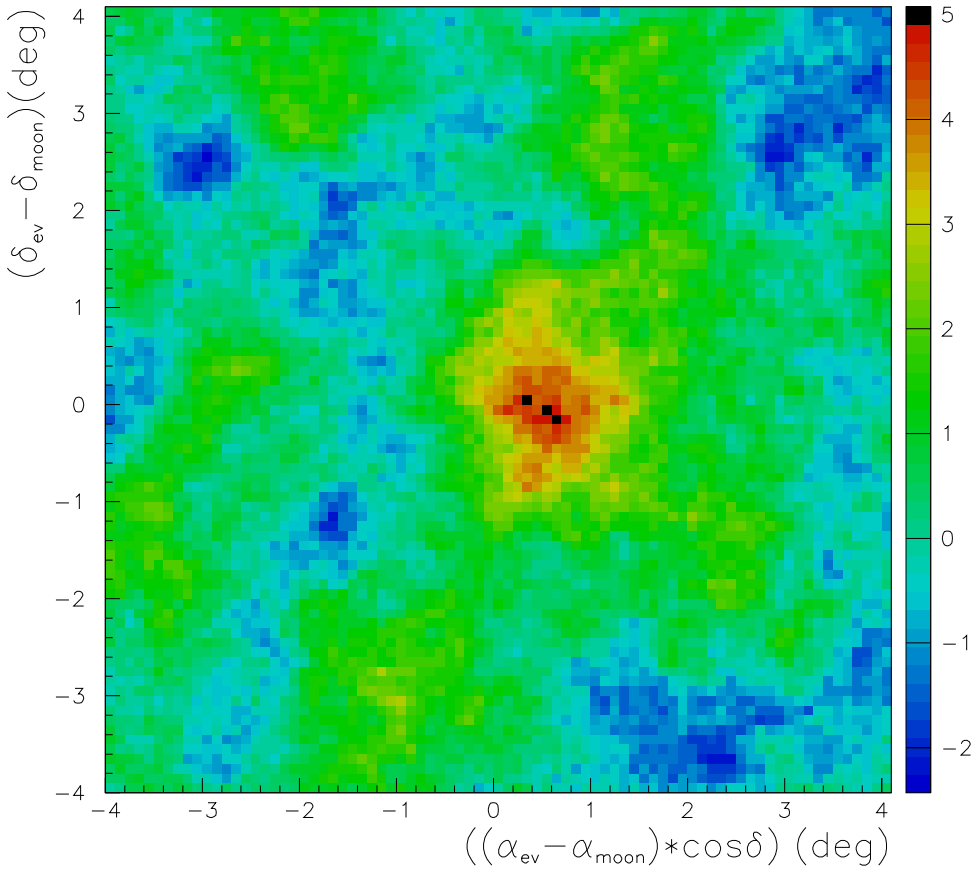

Figure 4.13: *Significance of ARGO-42 Moon shadow for showers with* $\theta < 50°$. *The scale given on the right indicates the significance in each* $0.1° \times 0.1°$ *bin.*

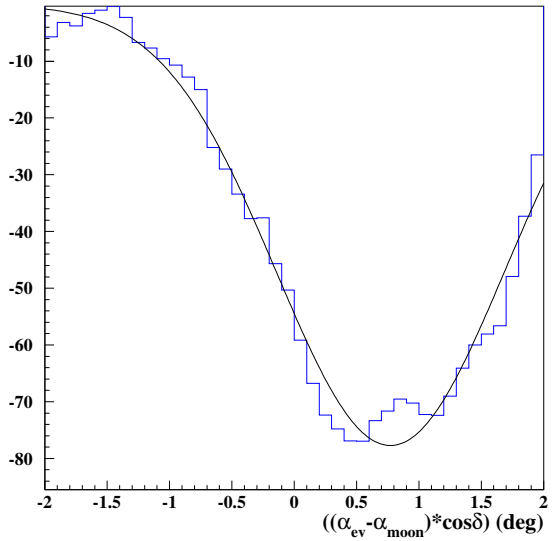

Figure 4.14: *East-West map projection. The continuous line represents the fit with a gaussian function.*

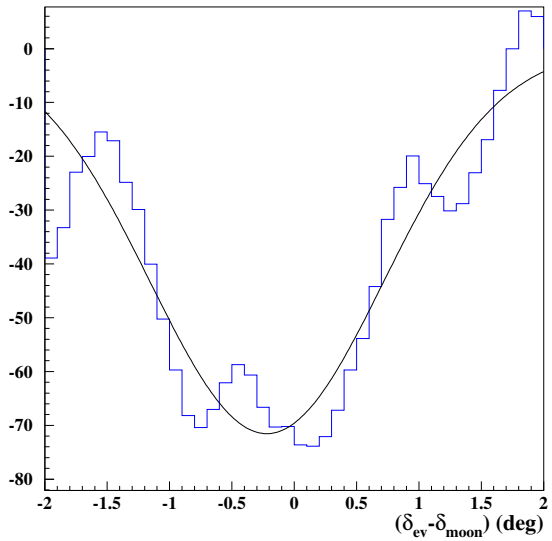

Figure 4.15: *North-South map projection. The continuous line represents the fit with a gaussian function.*

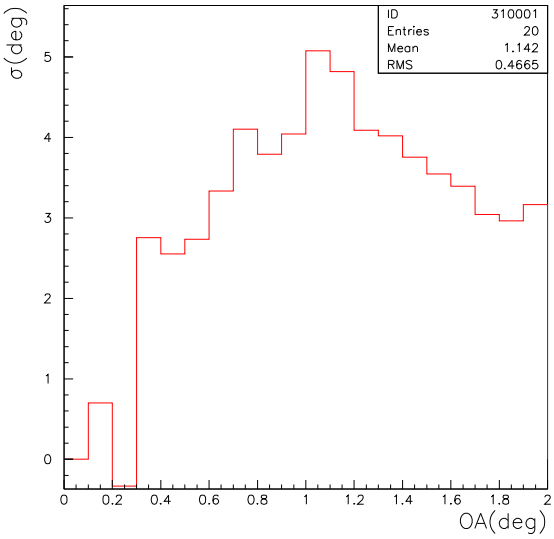

Figure 4.16: *Distribution of the significance (σ) versus the dimension of the radius of the circle bin used for smoothing the map (OA).*

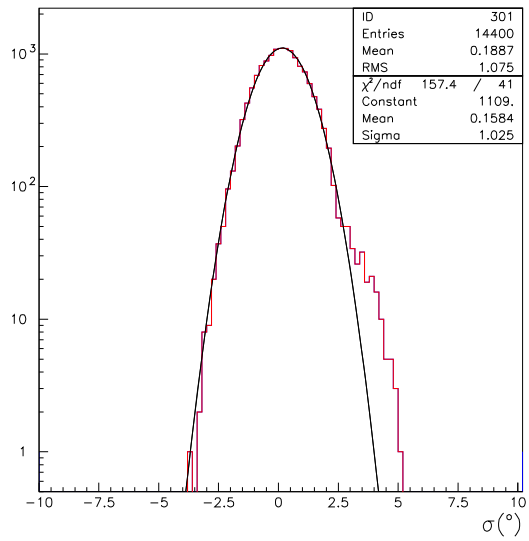

Figure 4.17: *Distribution of the significance (σ) in each* $0.1^\circ \times 0.1^\circ$ *bin.*

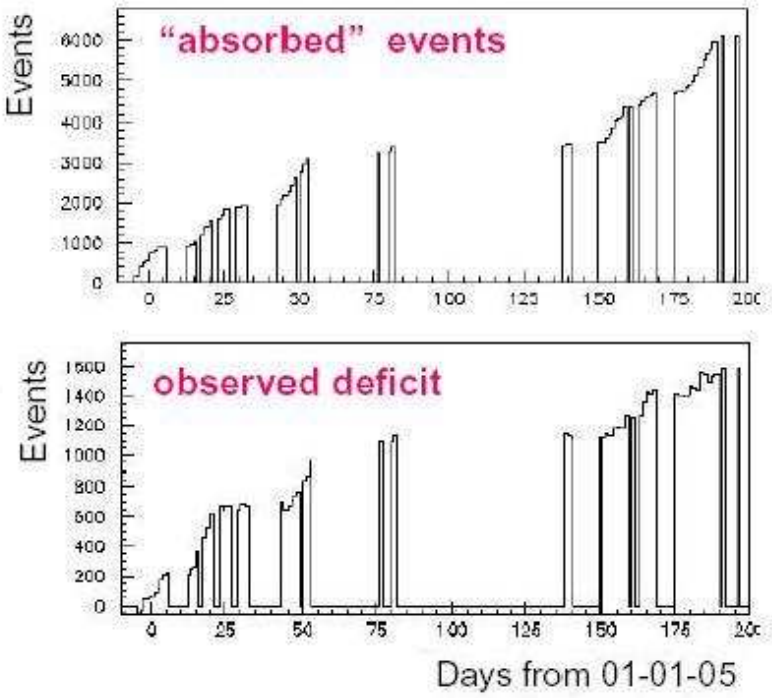

Figure 4.18: *Daily expected "absorbed" events (top plot) and observed deficit(bottom plot). Arbitrary units are used.*

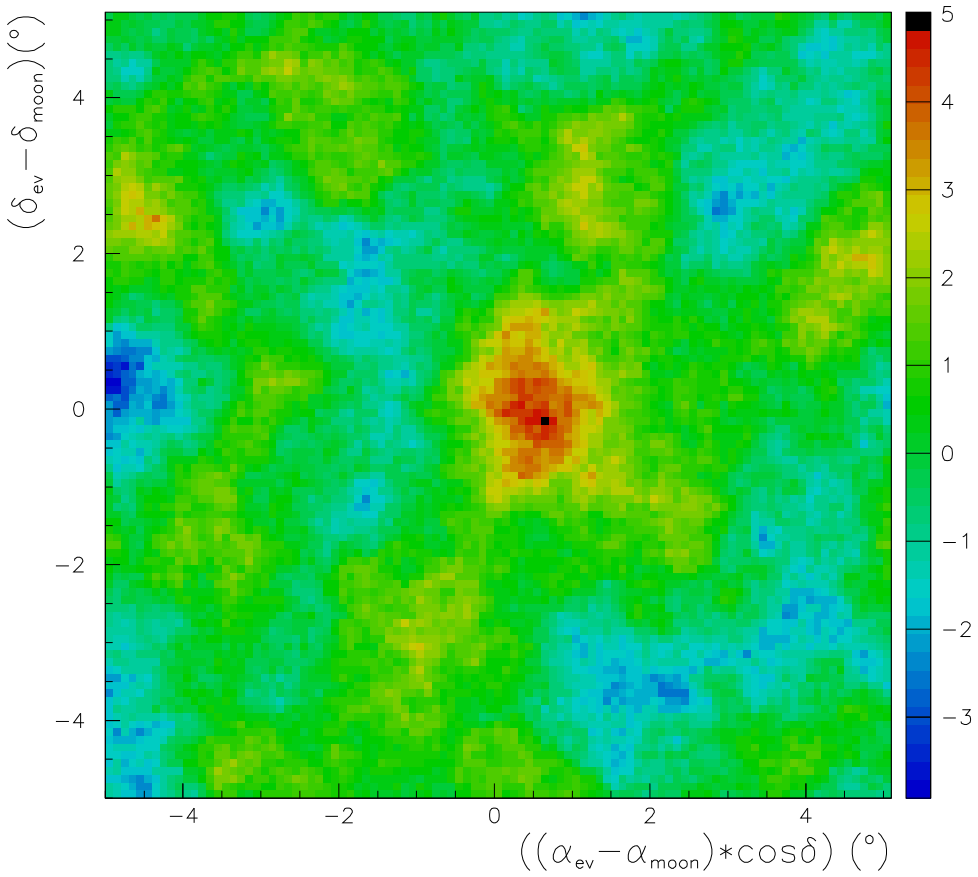

Figure 4.19: *Significance of ARGO-42 Moon shadow for events with* $\theta < 40°$*. The scale given on the right indicates the significance in each* $0.1° \times 0.1°$ *bin.*

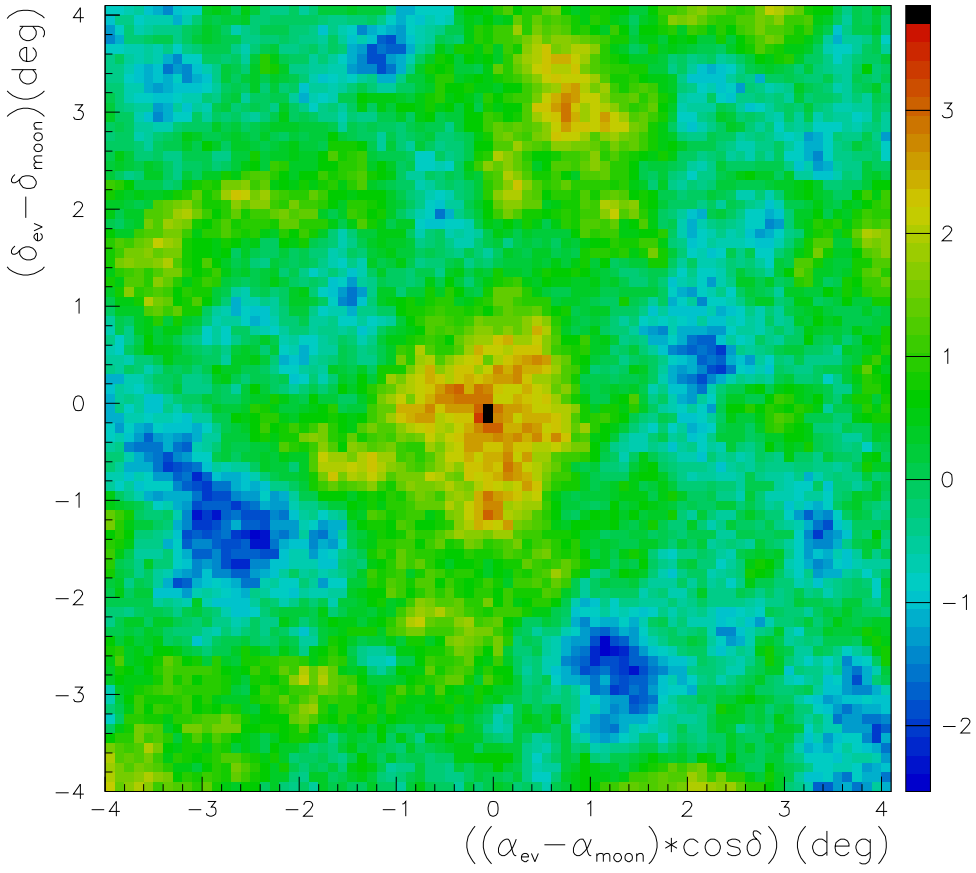

Figure 4.20: *Significance of ARGO-42 Moon shadow for events with* $\theta < 50°$ *and* $N_{pad} > 500$. *The scale given on the right indicates the significance in each* $0.1° \times 0.1°$ *bin.*

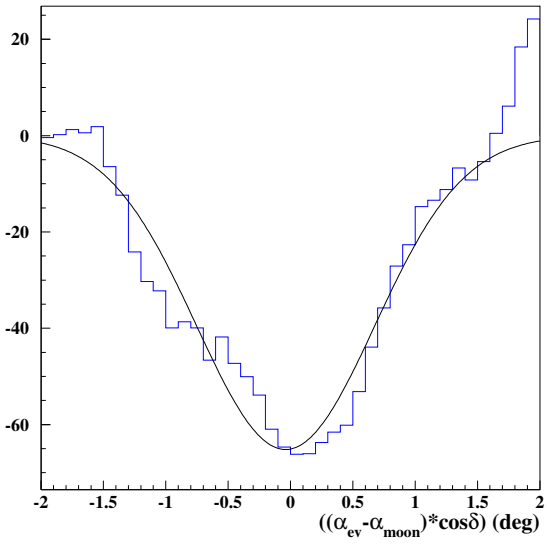

Figure 4.21: *East-west map projection for events with* $N_{pad} > 500$. *The continuous line represents the fit with a gaussian function.*

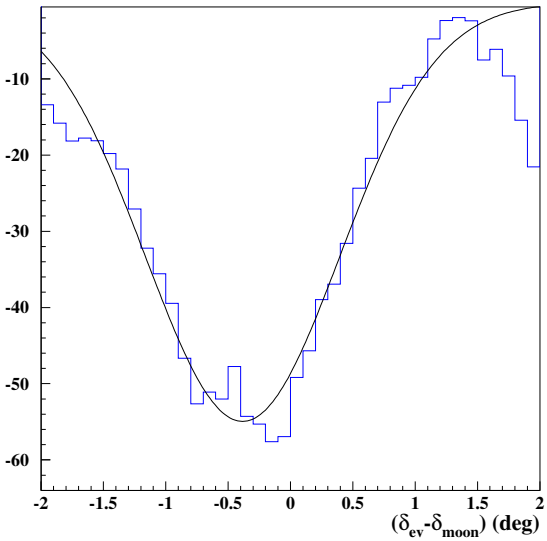

Figure 4.22: *North-south map projection for events with* $N_{pad} > 500$. *The continuous line represents the fit with a gaussian function.*

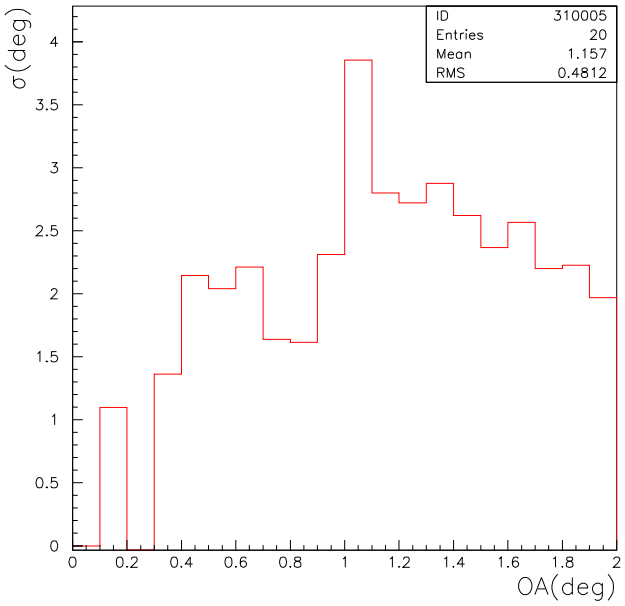

Figure 4.23: *Distribution of the significance (σ) versus the dimension of the radius of the circle bin used for smoothing the map (OA) for showers with* $N_{pad} > 500$.

Combining both the projections the resulting angular resolution is $\sigma_\theta = 0.6 \pm 0.3°$ compatible with the expected one (see Fig. 4.1).

Also in this case the event deficit is comparable with the expected value. The Fig. 4.23 shows the significance versus the dimension of the radius of the circle bin used for smoothing the map (OA) for showers with $N_{pad} > 500$. As can be seen the maximum of the sigma is reached for a radius of 1°.

The results suggest that increasing the number of fired pads not only improves the angular resolution but also reduces the systematic pointing errors. However, a residual effect is observed. The origin of this shift is still not completely clear.

Possible reasons are:

- no correct description of the detector orientation
- no selection of external events
- no accurate reconstruction of the core position due to the small detection area
- insufficient time alignment of the pads.

It is worthwhile to notice that a large detector as Tibet-ASγ operating since a long time measured a residual systematic pointing error of about 0.1°.

4.4 Sun shadow

As a further check of the previous results we have performed a preliminary analysis looking at the Sun shadow.

The Sun has the same shadowing effect on the cosmic ray flux as it passes overhead as the Moon does. Thus the shadow of the Sun can be studied in the same way as the shadow of the Moon. The shadow of the Sun is more complicated, however, because of its complex magnetic field.

The Sun's position oscillates with a period of one year. In a solar year its declination change between $\pm 23.5°$ and at YangBaJing the Sun follows a trajectory with the culmination zenith angle changing between 55.5° (winter) and 6.5° (summer).

Because of the motion of the Sun's position and the location of ARGO-YBJ only few data from the winter period have been used in the shadow analysis.

The Sun shadow has been analyzed in the same manner as the Moon shadow. Fig. 4.24 shows the smoothed significance map of the shadow of the Sun. Also in this case the radius of the window of the smoothed map is 1°.

The significance of the deficit is 4.6σ and the maximum of the significance is found 0.6° toward West and 0.3° toward South.

Also this result confirms the presence of a systematic effect which determines the same shift of the reconstructed deficit for both Moon and Sun.

4.5 Conclusions

In this chapter a first analysis of the angular resolution of the ARGO-YBJ detector by means of the study of the Moon and Sun shadow has been carried out. The data recorded by the ARGO-42 carpet refer to the period Dic. 2005 - Jul. 2005. The results of this work can be summarized as follows:

- the shadow of the Moon has been observed with a statistical significance of 5.1 σ for $N_{pad} > 60$ and of 3.9 σ for $N_{pad} > 500$ in about 338 h of observation time;

- from the analysis of the sky maps it results that the angular resolution of the ARGO-42 detector is $1.3° \pm 0.3°$ for $N_{pad} > 60$ and $0.6° \pm 0.3°$ for $N_{pad} > 500$, consistent with the expectation from MonteCarlo simulations and with the results of the data analysis with "chess-board" method;

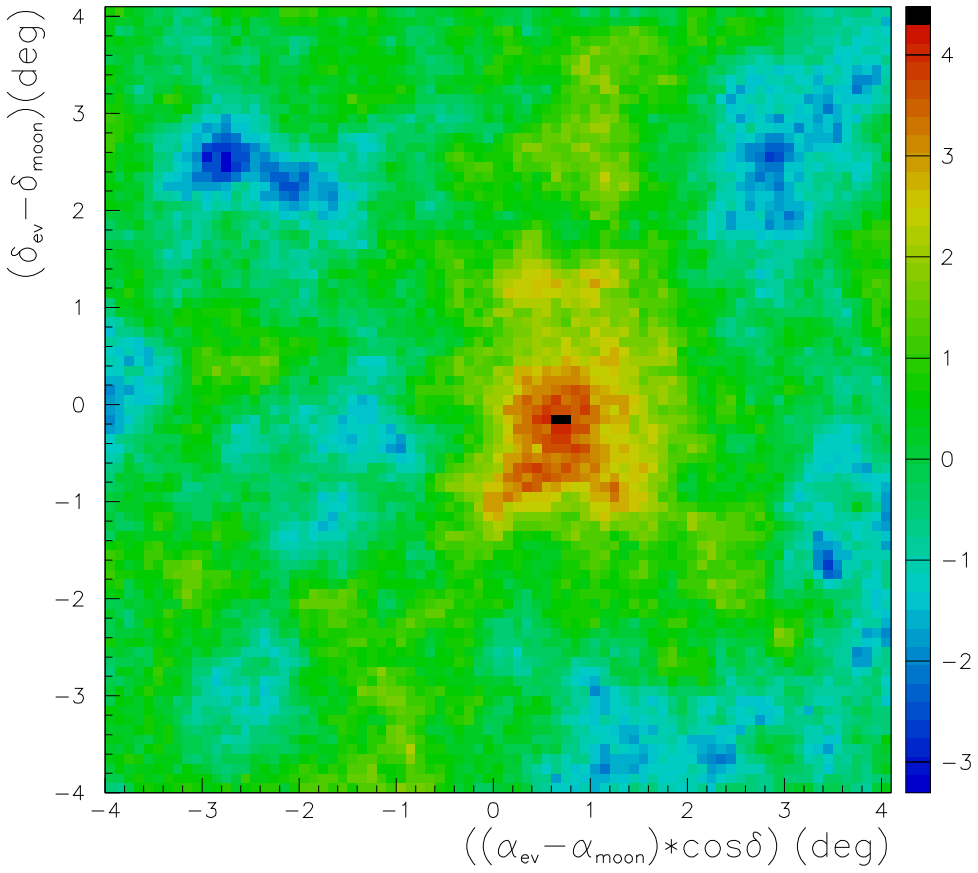

Figure 4.24: *Significance of ARGO-42 Sun shadow for events with* $\theta < 50°$. *The scale given on the right indicates the significance in each* $0.1° \times 0.1°$ *bin.*

- the resulting number of events cast by the Moon is in good agreement with the expectation;
- the position of the Moon is not shifted as expected from the magnetic field effect for $N_{pad} > 60$ ($E^{50} \sim 4\ TeV$). For a higher multiplicity $N_{pad} > 500$ ($E^{50} \sim 20\ TeV$) the shift from the true position is smaller as due to the reduced effect of the magnetic field;
- from the higher energy results we can conclude that a small residual systematic error affects the data;
- studies are in progress to investigate the disagreement in the position of the Moon at low energy. The main factor that can be responsible of the systematic effect in the angular reconstruction is the absence of the internal event selection;
- the shadow of the Sun has also been observed making us confident in our analysis procedures.

Conclusions

In this thesis we have studied the angular resolution of the ARGO-YBJ experiment both by means of MC simulations and analysis of data recorded by the detector ARGO-42 (42 Clusters, $\sim 47 \times 41\ m^2$, corresponding to about 1/3 of the whole central detector) operating and in data taking from December 2004 to July 2005.

The results of this work can be summarized as follows:

- the expected angular resolution σ_θ of the full ARGO-YBJ experiment calculated via MonteCarlo simulations, taking into account a 0.5 cm lead sheet on the RPCs, can be described by the following formula: $\sigma(^\circ) = 0.0011^\circ + 4.8187^\circ/\sqrt{N_{pad}}$, for γ-induced events with a Crab-like energy spectrum. We note that the resolution is 0.6° for $N_{pad} \sim 60$ and improve to 0.2° for $N_{pad} \sim 500$.

- The expected angular resolution for the carpet ARGO-42, without any lead sheet on the RPCs, can be described by the equation $\sigma(^\circ) = 0.27^\circ + \frac{20.06^\circ}{(N_{pad})^{0.67}}$ for photon-induced showers with a Crab-like energy spectrum. The angular resolution results 1.1° for $N_{pad} \sim 60$ ($E^{50} \sim 4\ TeV$) and improves to 0.4° for $N_{pad} \sim 500$ ($E^{50} \sim 20\ TeV$).

- Using tha data collected by the ARGO-42 carpet the angular resolution has been studied with two different techniques, that is by applying the so-called "chess-board" method and by analyzing the shadow in the primary cosmic flux cast by the Moon.

Results from both methods are well consistent with MonteCarlo predictions, suggesting that the simulation of the detector response and the reconstruction algorithms are correct.

The shadowing effect of the Moon has been detected at a good significance level ($\sim 5\ \sigma$) in only few months of data taking. This is a record, once compared to the about 2 years of data taking required by other EAS arrays. This result is due to two peculiar features of the ARGO-YBJ detector, that is the very low energy threshold and the excellent angular resolution. A residual shift of the Moon shadow respect to the expected position has been observed. A selection of events with a high number of particles reduces

this shift that can be ascribed to a systematic pointing inaccuracy. Possible reasons have been identified and will be investigated in a future work.

The experimental results of ARGO-42 concerning the angular resolution provide a solid confirmation of the goodness of the reconstruction procedures and make us extremely confident of the performance of the ARGO-YBJ detector. Accordingly we foresee that ARGO-YBJ will work, without any $\gamma-$hadron discrimination at the design sensitivity of 0.3 Crab units.

Bibliography

[1] Schklovsky, Dokl. Akad. Nauk. 90 (1953) 983.

[2] G. Cocconi, ICRC Moscow II (1960) 309.

[3] Aharonian, astro-ph/0511139.

[4] G. W. Clark Phys. Rev. 108 (1957), 450.

[5] A. Gross, astro-ph/0505278, (2005). 40th Rencontres de Moriond on Electroweak Interactions and Unified Theories, La Thuile, Italy, 5-12 Mar 2005.

[6] M. Abbrescia et al., *Astroparticle Physics with ARGO*, Proposal (1996). C. Bacci et al., *The ARGO-YBJ Project*, Addendum to the Proposal (1998).

[7] M. Urban et al. *Astrophysics and Particle Physics*, Proceedings of the 21st International Cosmic Rays Conference, Adelaide, Australia 1990, Vol.11 p.23.

[8] D.E. Alexandreas et al., *Phys. Rev.* **D 43** (1991) 1735.

[9] L3+C collaboration, J.-F. Parriaud, in Proceedings of the XIVth Rencontres de Blois, 2002, Blois, France.

[10] R. Hartman et al., *The Astrophys. J. Suppl.* 123 (1999) 79.

[11] R.A. Ong, Rapporteur paper *Proc. of the 29th ICRC)*(2005) Pne,India.

[12] Aharonian et al., ApJ, Vol. 614 (2004) 897.

[13] Weekes, T.C., et al., *ApJ* **342** (1989) 379.

[14] Aharonian, F. et al., *A&A* **435** (2005) L17.

[15] Aharonian, F. et al., *Science* **307** (2005) 1938.

[16] Aharonian, F. et al., *A&A* **437** (2005) L7.

[17] Muraishi, H. et al. *A&A* **354** (2000) L57.

[18] Puhlhofer, G. et al., *Proc. 27th ICRC (Hamburg)* **6** (2001) 2451.

[19] Aharonian, F. et al., Accepted for publication in *ApJ* (2005) astro-ph/0501397.

[20] Chadwick, P.M. et al. , *ApJ* **503** (1998) 391.

[21] Aharonian, F. et al., *A&A* (in press) (2005); astro-ph/0506280. bibitemgalcen Aharonian, F. et al., *A&A* **425** (2004) L13.

[22] Aharonian, F. et al., *A&A* **393** (2002) L37.

[23] Aharonian, F. et al., *A&A* (in press) (2005); astro-ph/0505219.

[24] R. Atkins et al., Astrophy. J., 680-685 (2004).

[25] Amenomori, M., et al. 2002, *ApJ* 580, 887.

[26] Smith, A. J., et al., 2005, International Symposium on High-Energy Gamma-Ray Astronomy, eds F.A. Aharonian, H.J. Völk, D. Horns, AIP Conference Proceedings, 745, 657.

[27] Fleysher, R. et al. 2004, International Symposium on High-Energy Gamma-Ray Astronomy, ed. F.A. Aharonian, H.J. Völk, D. Horns, AIP Conference Proceedings, 745, 265 (available at http://arxiv.org/abs/astro-ph/0502303).

[28] Aharonian, F., et al. 2002b, A&A, 395, 803.

[29] T. C. Weekes, *Physics Report* 160 (1988) vol. 1,2.

[30] R. Ong, Int. J. Mod. Phys. A15S1 (2000) 740;

[31] F. Longo et al., Nucl. Phys. B Proc. Suppl. 125, 222-229 (2003).

[32] N. Gehrels et al., Astropart. Phys. 11 (1999) 277;

[33] B. Rossi, High Energy Particles, Prentice-Hall, Englewood Cliffs (1052).

[34] P. T. Raynolds et al., *The Astrophysical Journal* 404 (1993) 218.

[35] S. Oser et al., Astroph. J. 547 (2001) 949 ;

[36] S. De Naurois et al., Astroph. J. 566 (2002) 343;

[37] Xu, X. W. et al. J. Phys., 2003, G29, 719.

[38] M. Amenomori et al., Astrophys. J. **633**, 1005 (2005).

[39] R. Atkins et al.,Nucl. Instr. and Meth. **A449** (2000) 478.

[40] R. Atkins et al., Astrophys. J. **595**, 803 (2003).

[41] A. Borione et al., *Phys. Rev.* **D 49** (1994) 1171.

[42] M. Amenomori et al., *Phys. Rev.* **D 47** (1993) 2675.

[43] M. Ambrosio et al., *Phys. Rev.* **D 59** (1999) 012003.

[44] M. Ambrosio et al., *Astrop. Phys.* **20** (2003) 145.

[45] J. H. Cobb et al., *Phys. Rev.* **D 61** (2000) 92002.

[46] M. Urban, P. Fleury and R. Lestienne F. Plouin Nucl. Phys. B Supp. Volume 14, Issue 2 (1990), 223-236.

[47] Amenomori M. et al., *Phys. Rev.* **D47** (1993) 2675.

[48] TibetASγ-collaboration, T. Kido, in HE 3.3.2., Proceedings of the XXVIIIth ICRC, 2003 Tsukuba, Japan.

[49] G. Di Sciascio et al., "Selection of the primary cosmic ray light component with ARGO-YBJ", 19th European Cosmic Ray Symposium, Florence (2004).

[50] M . Iacovacci et al., "The RPC charge read-out in the ARGO-YBJ experiment", Proc. 29th ICRC, Pune (2005).

[51] Zhen Cao et al., "Status of the ARGO-YBJ experiment", Proc. 29th ICRC, Pune (2005).

[52] The ARGO-YBJ coll., "Performance of RPCs used for cosmic ray experiments", preprint submitted to Elsevier Science, (2005).

[53] S. Mastroianni et al., "The ARGO-YBJ inclusive trigger", Proc. 29th ICRC, Pune (2005).

[54] A. Aloisio et al., IEEE Trans. Nucl. Sci. 51, 1835 (2004).

[55] A.M.Hillas et al., *ApJ* 503,744 (1998).

[56] J.R. Horandel et al., Proc. 27th ICRC Hamburg (2001).

[57] S. Vernetto et al. Proc. 26th ICRC, Salt Lake City (1999) astro-ph/9906185.

[58] A. Aloisio et al., Nuovo Cim. 24C, 4-5, 739 (2001).

[59] T. Di Girolamo et al. "Performance of the ARGO-YBJ detector in scaler mode", Proc. 29th ICRC, Pune (2005).

[60] D. Heck, J. Knapp, J.N. Capdevielle, G. Schatz, and T. Thouw. Report **FZKA 6019** (1998), Forschungszentrum Karlsruhe

[61] G. Di Sciascio, B. D'Ettorre Piazzoli, M. Iacovacci, Astrop. Phys. 6 (1997) 313.

[62] D. Campana, B. D'Ettorre Piazzoli and G. Di Sciascio, Nucl. Instr. and Meth. **A344** (1994) 250.
C. Bacci et al., Astrop. Phys. 17 (2002) 151.

[63] E. Rossi, Degree thesis (in italian) "Ricostruzione di sciami atmosferici prodotti da fotoni di alta energia con il rivelatore ARGO-YBJ".
G. Di Sciascio, E. Rossi, ARGO-YBJ Internal Note 04/2003.

[64] G. Di Sciascio et al., "Algorithms for the determination of the primary particle direction with ARGO-YBJ", *Proc. 28th ICRC*, Tsukuba (2003).

[65] G. Di Sciascio and E. Rossi for the ARGO-YBJ coll., "Study of the angular resolution of the ARGO-YBJ detector", Proc. of the "Incontro Nazionale di Astrofisica delle Alte Energie (2003).

[66] G. Di Sciascio et al., "First results on the angular resolution of the ARGO-YBJ detector", *Proc. of the 29th ICRC)* Pune, India (2005).

[67] G. Di Sciascio et al., Proc. 28th ICRC, Tsukuba (2003) p. 3015.

[68] G. Di Sciascio, ARGO-YBJ Internal Note 02/2002.

[69] D.E. Alexandreas et al., Nucl. Instr. and Meth., A328:570 (1993).

[70] P. Bernardini et al., "Time calibration of the ARGO-YBJ experiment", Proc. 29th ICRC, Pune (2005).

[71] M. Aglietta et al., Astrop. Phys. 10 (1999) 1.

[72] G. Cocconi, Handbuch der Physik, Vol. XLVI/1 (1961) 215.

[73] P. Bassi, G. Clark and B. Rossi, Phys. Rev. 92 (1953) 441.

[74] M. Urban et al., *Nucl. Phys. B (Proc. Suppl.)* **14B** (1990) 223.

[75] Lloyd-Evans J., *Proc. of the 19th ICRC)*, La Jolla, California **2** (1985) 173.

[76] Linsley J., *Proc. of the 19th ICRC)*, La Jolla, California **3** (1985) 465.

[77] J. D. Jackson, "Classical Electrodynamics", Wiley & Sons., NY (1975).

[78] C. Caso et al., Eur. Phys. J., 15 (2000).

Aknowledgments

Voglio ringraziare il prof. D'Ettorre, riferimento e guida, per i consigli e le utili discussioni.

Un grazie speciale va al dott. Di Sciascio che ha seguito il mio lavoro passo dopo passo e che mi ha sempre incoraggiato a percorrere la strada che credevo più interessante. Grazie perchè senza di lui questa tesi non sarebbe stata possibile.

Grazie alla dott. Vernetto per il suo supporto e la sua esperienza, grazie per il suo entusiasmo coinvolgente.

Ringrazio tutte le persone dell'esperimento ARGO-YBJ ed in particolare il prof. Bartoli, il prof. Iacovacci, il prof. Catalanotti e il dott. Di Girolamo.

在此同时向在ARGO-YBJ实验中付出努力的中国同事们表示问候和感谢

Un grazie ai miei colleghi di stanza e cari amici Stefano, Luigi e Sheng.

Grazie alla mia famiglia che mi sostiene e ancora mi sopporta. A Biagio, il mio fratellino, dedico questa tesi perchè gli voglio bene.

Un abbraccio a miei nonni, azio Lino e zia Rosaria, Giusina e Cocca. Grazie a Maria, Katia, Alfredo e Anna.

Voglio ringraziare tutte le persone che mi vogliono bene e che mi sono sempre vicine.

C'è chi ci indica la strada e chi ci è vicino qualsiasi strada intraprendiamo...tu fai entrambe le cose...MariaRosaria ti voglio bene.

Dire grazie a Francesco in poche righe è come fare un viaggio attraverso l'oceano chiusi nella stiva di una nave.

Un grande abbraccio a Giorgio, Grazia, Francesca e Mimi.

Grazie a Olghina, Giuseppe e Lello ragazzi brillanti. Un bacio a Maria e Rosaria, dopo tanti anni siamo sempre insieme.

Un saluto ai miei compagni d'avventura: BlackHole Phil, Philip, Chris e Christian, Giorgios, Miltos e la dolce Aba e tutti gli altri che non posso elencare per problemi di spazio!

Altro abbraccio forte ai miei tesori piccoli Bicocco e Bisesti e agli altri miei piccoli di adozione: Cristina, Peppe, Letizia, Carmen, Nicola, Mariantoni-

etta, Nicola, Antonio, Ernesto. Un abbraccio anche a Daniele e ai suoi compagni che mi hanno dovuto sopportare al corso di exp2.

Un abbraccio fortissimo alla mia gemellina e a Peter Parker Roberto.

Freedom as a scent like the top of a new born baby's head
the songs are in your eyes I see them when you smile
I had enough of romantic love I give it up for
a miracle drug